DISSOLUTION AND PRECIPITATION IN SUBSURFACE REACTIVE FLOW WITH COMMON-ION EFFECT

MASOUD GHADERI ZEFREH

Submitted for the degree of Doctor of Philosophy
Institute of Petroleum Engineering
Heriot-Watt University
Monday 28th October, 2019

ABSTRACT

Simulation of multiphysics, multicomponent and multiphase flow for oil reservoirs has become possible thanks to advances in computing technology. However, computational costs for simulating these strongly coupled processes in systems whose parameters are only known statistically remains a limiting factor. The coupling of the processes and the resulting systems of equations at the current computational power, however, only allows for resolutions of the order of tens to hundreds of metres. The course resolution hampers the understanding through numerical diffusion/dispersion that potentially leads to drastic under or overestimation of processes. Even at fine resolutions, numerical solutions may not provide understanding about the nature of the processes unless an ensemble of solutions is obtained on the whole parameter space. In this dissertation, we aim to provide an understanding of a specific class of reactive flow in the subsurface. The ultimate goal is to pave the way for a better intuition of reactive flow relevant to precipitation of minerals around well-bore, known as scaling.

This thesis presents the analytical solution for the reactive flow of two dissolution/precipitation reactions. The two reactions are coupled through a common ion and therefore we have the co-ion effect. We account for the volume of precipitate and hence allow changes of the porosity during dissolution and precipitation. The solution is an extension to the one provided by Helfferich [1]. An important finding here is the induced precipitation of one salt in the course of dissolution of another salt. Accounting for the volume of precipitates allows to analyse clogging of the medium using the ratio of molar densities and equilibrium constants for salts.

Moreover, a streamline approach is discussed to extend the solution to multidimensional settings. In developing the streamline simulator, we account for the heterogeneity of the medium which creates a system of hyperbolic PDEs with discontinuous flux function. It is shown that this specific problem can be solved following the minimum jump entropy condition. Hence, an analytical approach is provided which removes any numerical dispersion in transport of the ions. However, this imposes zero mixing at the well which requires another treatment. Mixing at the well, therefore, needs to be explicitly modelled. A such model is proposed and couplled with the transport similar to conventional streamline simulators.

Finally, the problem is studied in the context of fractured networks. In fracture networks, mixing becomes more important because several locations exist

at which different streams can mix. These locations are the intersection of the fractures which have tiny volumes comparing to the length of fractures. Hence, mixing and transport occur in scales that are different by several orders of magnitude. A novel algorithm is developed and studied for this type of problems. It is concluded that to effectively simulate the single phase transport of ions in networks of fractures, three time steps need to be identified. The first is a time-step at which pressure of the system needs to be updated due to significant changes in the intersections. This is similar to conventional streamline simulators. In addition, a list of times for arrival of fronts at mixers needs to be calculated. This is done via solving an equation of motion for each front. Finally, if a dissolution is happening, the time at which dissolution terminates needs to predicted. No other spatial information is required and hence the difficulty in the difference of scales is circumvented. The benefit of this approach is the understanding it offers about the problem as well as the computational advantage over standard finite volume methods.

To my heroes: my beloved parents.

ACKNOWLEDGEMENTS

First and foremost, I would like to express my sincere gratitude to my advisor, Dr. Florian Doster. This academic and personal journey would not have been possible without his guidance. I was privileged to receive valuable inputs, ever sustained enthusiasm and interest from his side. This encouragement fuelled me to confidently explore into a relatively new field for me. But it also taught me different ways of thinking.

I would also like to thank my collaborators and mentors Prof. Eric Mackay, Dr. Marc Hesse, Prof. Knut Andreas Lie, Dr. Halvor Nilsen, Dr. Xavier Raynaud. It was a great honour for me to know and work with them.

I would like to thank the examiners, Prof. Ken Sorbie and Dr. Jerome Neufeld who patiently and meticulously read my thesis. Their valuable feedbacks and comments improved this thesis. Their scrutiny helped me to modify the thesis such that it spells out the important messeges. I am honoured to have been directed by them.

I am also very grateful to all my friends whose presence was another reason to enjoy research in Heriot-Watt and Edinburgh.

Finally, I am thankful to Energi Simulation (former Foundation CMG) and Energy Technology Partnership of Scotland to provide the funding for this research.

Monday 28th October, 2019

Research Thesis Submission

Name*:*	MASOUD GHADERI ZEFREH		
School:	EGIS		
Version: *(i.e. First, Resubmission, Final)*	Final	Degree Sought:	PhD

Declaration

In accordance with the appropriate regulations I hereby submit my thesis and I declare that:

1. The thesis embodies the results of my own work and has been composed by myself
2. Where appropriate, I have made acknowledgement of the work of others
3. The thesis is the correct version for submission and is the same version as any electronic versions submitted*.
4. My thesis for the award referred to, deposited in the Heriot-Watt University Library, should be made available for loan or photocopying and be available via the Institutional Repository, subject to such conditions as the Librarian may require
5. I understand that as a student of the University I am required to abide by the Regulations of the University and to conform to its discipline.
6. I confirm that the thesis has been verified against plagiarism via an approved plagiarism detection application e.g. Turnitin.

ONLY for submissions including published works

7. Where the thesis contains published outputs under Regulation 6 (9.1.2) or Regulation 43 (9) these are accompanied by a critical review which accurately describes my contribution to the research and, for multi-author outputs, a signed declaration indicating the contribution of each author (complete)
8. Inclusion of published outputs under Regulation 6 (9.1.2) or Regulation 43 (9) shall not constitute plagiarism.

* *Please note that it is the responsibility of the candidate to ensure that the correct version of the thesis is submitted.*

Signature of Candidate*:*		Date:	28 October, 2019

Submission

Submitted By *(name in capitals):*	
Signature of Individual Submitting:	
Date Submitted:	

For Completion in the Student Service Centre (SSC)

Limited Access	Requested	Yes		No		Approved	Yes		No	
E-thesis Submitted ***(mandatory for final theses)***										
Received in the SSC by *(name in capitals):*										

HERIOT WATT UNIVERSITY

Inclusion of Published Works

Please note you are only required to complete the Inclusion of Published Works Form if your thesis contains published works under Regulation 6 (9.1.2)

Declaration

This thesis contains one or more multi-author published works. In accordance with Regulation 6 (9.1.2) I hereby declare that the contributions of each author to these publications is as follows:

Citation details	M. Ghaderi Zefreh, H. Nilsen, K. A. Lie, X. Raynaud, F. Doster *"Streamline simulation for a reactive flow with discontinuous flux function"* Journal of Computational Geosciences(2019) 23:255-271 DOI: 10.1007/s10596-018-9771-3
Author 1	Implemented and coordinated the algorithm, wrote the paper
Author 2	Developed the method
Author 3	Implemented part of the algorithm
Author 4	Developed the model
Author 5	Designed the question and the method, developed the model
Signature:	
Date:	28 October, 2019

Citation details	M. Ghaderi Zefreh, F. Doster, M. A. Hesse *"Theory of precipitation dissolution waves - redux"* AIChE Journal (2019) 65(6); DOI: 10.1002/aic.16573
Author 1	Derived part of the analytical solution, wrote the paper
Author 2	Developed the model, designed the method
Author 3	Designed the question, developed the model
Signature:	
Date:	28 October, 2019

CONTENTS

LIST OF FIGURES

LIST OF TABLES

PUBLICATIONS

This thesis contains excerpts from the following papers:

M. Ghaderi Zefreh, H. Nilsen, K.A. Lie, X. Raynaud, F. Doster (2018). streamline simulation for a reactive flow with discontinuous flux function. Comput Geosci, DOI: 10.1007/s10596-018-9771-3

M. Ghaderi Zefreh, F. Doster, M. Hesse (2019). Theory of precipitation dissolution waves – redux. AIChE journal,
DOI: 10.1002/aic.16573

M. Ghaderi Zefreh, F. Doster. Precipitation and dissolution in self-mixing hydraulic paths. In preparation

1

INTRODUCTION

Injection of seawater for oil recovery, also referred to as water-flooding, is one of the most common recovery methods applied in offshore reservoirs [2]. Water-flooding increases the recovery factor by maintaining the pressure of the reservoir [3, 4]. However, incompatibility of the seawater with formation water may result in the formation of salts. Accumulation of these salts, particularly around well-bores, is a major issue in water-flooding [5]. The formed salts are also referred to as *scales* and the formation process is known as *scaling*.

Scale removal techniques vary from mechanical operations, e. g., pig running and abrasive jetting to chemical treatments like the injection of an acid [6]. However, it is more desirable to avoid scaling than to remove it after it has formed. Hence, *squeeze treatments* are usually performed that involve injection of a chemical agent [7]. These agents act as an inhibitor and are adsorbed or precipitated on the surface of the rock and are designed to gradually dissolve or desorb in the produced water to inhibit any scale formation [8].

Simulation of scaling involves solving a system of nonlinear reactive transport partial differential equations. The non-linearity arises from the corresponding chemical reactions. The transport, however, is linear and is dominated by advection rather than diffusion. Therefore, normally the diffusion part in a simulation of flow in the subsurface is neglected for up-scaled models [9]. It should be noted, however, that in all real systems diffusion exists to some extent. In subsurface flow, the diffusion causes the upstream and downstream flow of a moving front to mix slightly. This small degree of mixing is favourable in reservoir [10, 11] and is referred to as *barium stripping*. The term refers to the fact that barium, which is one of the key components in scaling, is preferred not to be produced. If the degree of the numerical dispersion is larger than actual diffusion in the well, then barium stripping is overestimated. The result would be an underestimation of scales around well-bore. Therefore, it is important to limit the numerical dispersion as it can exceed the actual diffusion by several orders of magnitude.

In a chemical system that involves dissolution and precipitation of minerals, presence of an ion that takes part in more than one reaction causes a phenomenon known as the common-ion (or the co-ion) effect. The effect is referred

to as the influence of the common ion in changes of the reactivity of the dissolution [12]. In the production of scales and in particular sulphates at the wellbore, we have the common-ion effect. I.e., sulphate ions are common in the corresponding chemical reactions for barite, anhydrite and celestite.

The objective of this thesis is to provide a better understanding for the reactive flows with the common-ion effect in the subsurface through analytical solutions in one dimension. Two classes of problems are studied in Chapters 3 and 4 and features of the solutions are analysed. Meanwhile, we aim to construct efficient methods for simulation in higher dimension. The main idea for extension of one-dimensional solution to higher dimension, is the streamline methods. We have made modifications to such methods to make them suitable for the one-dimensional solution that are provided. Extensions to higher dimension are discussed in Chapters 4 and 5 and expanded to include mixing. The benefit of these new methods is their accuracy in terms of reducing the numerical dispersion. However, several simplifying assumptions are made in derivation of the one-dimensional analytical solution which are then migrated to the algorithms for higher dimension. The limitations and features of the proposed of the analytical solutions and algorithm are detailed in each of the chapters.

In this chapter, we review the previous works that are related to Chapters 3 to 5. Ie, we provide a literature review to analytical solutions for one-dimensional reactive flows, streamline methods. In addition, a brief review is given on reactive flows in fracture networks as the last chapter is devoted to application of our methodology in this context.

1.1 Analytical solution to 1D reactive flow with significant porosity change

Precipitation and dissolution during flow in porous media play a major role in many different processes e.g., contaminant transport in aquifers [13, 14], oil recovery processes [15–17], geothermal processes [18, 19] and concrete carbonation [20]. Dissolution and precipitation can be induced by three distinct types of flow-induced reactions [21]: mixing reactions between fluids of different composition [22], gradient reactions due to changes in temperature and pressure along the flow path [23], and frontal reactions driven by the invasion of a fluid with different composition and/or temperature [1, 24–26]. Here, we are interested in the chromatographic patterns that arise during frontal dissolution-precipitation reactions [16]. It should be noted that although the physical processes in chromatography are different than in dissolution and precipitation, the underlying mathematics is similar. It has been shown that the concept of multicomponent chromatography can be used in precipitation and dissolution problems. [1]

Generally, a model for single-phase flow with dissolution and precipitation in porous media involves advective transport, hydrodynamic dispersion and molecular diffusion of components as well as chemical reactions between components [27, 28]. However, in large-scale problems the chromatographic pattern of frontal dissolution-precipitation reactions is independent of reaction kinetics and solute dispersion [29–32]. The analysis presented in this thesis is therefore limited to systems in local chemical equilibrium and with negligible hydrodynamic dispersion. Other premises taken here are incompressibility of the medium and the fluid, immobility of precipitates and isothermal conditions. These assumptions allow for obtaining a model that falls in the class of hyperbolic partial differential equations (PDEs) [1, 33].

The assumption of local equilibrium introduces a discontinuity between two zones with different compositions. It is, therefore, instructive to study the evolution of the discontinuity in the initial condition. An initial-value problem with discontinuous initial states is known as a *Riemann Problem*. A very close concept related to the study of the evolution of discontinuities is "coherence", initially developed for chromatography [34]. Note that relaxing the local equilibrium assumption may impose a new structure for the solution. This has been studied for multiphase problems [35], where new shock structures emerge.

The coherence concept is able to demonstrate that an arbitrary initial variation may be unstable and hence it decomposes into several stable variations as it propagates through the system. These variations may travel at different speeds and new regions with constant state appear as a result [36]. This is following the *method of characteristics* (MOC) from which we obtain self-similar solutions for a Riemann Problem with an initial single discontinuity at the origin [37]. The method of characteristics is discussed in details in Chapter 2.

The method of characteristics has been used in one-dimensional reactive flow in the context of ion-exchange [38–40], multi-component chromatography [34, 41], adsorption and desorption [42, 43] and precipitation and dissolution [1, 15, 44]. The presented model in Chapter 3 is similar to the one presented in [1], as both models consider the co-ion effect. However, we account for the volume of the precipitates here.

1.2 STREAMLINE SIMULATION

The analysis presented in Chapter 3 or in [1] are both limited to one-dimensional settings. For higher dimensions, one can use numerical schemes to tackle these type of problems including additional physical processes [18–20, 45–48]. Alternatively, we can assemble the one-dimensional solutions to develop a streamline simulator. Streamline simulation is a divide-and-conquer strategy that solves

flow (pressure/flux) and fluid transport in separate steps. It uses a Lagrangian grid with a sub-grid resolution for the fluid transport and exploits loose couplings in the equations to enable large time steps. Due to this advantage, streamline simulators have been developed to cope with full 3D compositional reservoir models [49–51] in multiphase flow [52, 53], taking into account miscibility [54, 55] and compressibility of phases [56] as well as fractures in the porous medium [57]. Here, we aim to develop a streamline simulator for the problem discussed in Chapter 2.

In principle, a streamline simulator for porous media has three main components that work together;

1. A pressure solver that calculates the pressure field by solving the elliptic or parabolic pressure equation and evaluates the velocity field using Darcy's law. This solver works on the Eulerian coordinates.

2. A 1D solver that solves the evolutionary 1D transport problem for a given time step on the Lagrangian coordinates.

3. A mapping from Eulerian to Lagrangian coordinates and vice versa. The former uses the flow information (pressure and velocity field) to obtain the Lagrangian coordinates. This transformation decouples the 2D/3D problem into a family of 1D problems along streamlines. Since the 1D problems are independent, we can pick a representative set of streamlines. These streamlines are then passed to a 1D solver that propagates compositions or other quantities. The results of the 1D solver are mapped back to the Eulerian coordinates through averaging the quantities from streamlines.[58]

The choice of the 1D solver depends on the physical processes involved and affects the overall performance. *Front-tracking* algorithms [59] are very well suited for convection dominated flows because they use the exact solution of the corresponding Riemann Problem and can resolve displacement fronts and other discontinuities exactly [60, 61].

As we will discuss in Chapter 4, the one-dimensional problem for the corresponding three-dimensional problem shows spatial discontinuities in the flux function. Hyperbolic partial differential equations with spatially discontinuous flux functions appear frequently in simulation of flow in porous media. The theory for the solution is well established for generic one-dimensional scalar cases [62–65] and multidimensional scalar cases [66]. However, a general approach to solve these type of challenging problems for systems of equations is not available. Existence and uniqueness of solutions for linear systems have been studied and some numerical techniques for nonlinear systems are suggested based on linearisation [67]. Another type of numerical scheme for systems with spatially discontinuous flux functions is suggested in [68]. The solution in the general

case can depend on the small scale assumptions. The main point of our problem is that all the waves travel in the same direction and a global solution can be derived. Our solution for the 2×2 system is based on conservation of mass across the interface and the simple principle of increasing speed of propagation for the sequence of solution waves which for two waves means that the leading wave must propagate faster than the trailing wave.

1.3 DISSOLUTION AND PRECIPITATION IN FRACTURE NETWORKS

Fractured rocks are ubiquitous. Understanding fluid dynamics in them is relevant in many applications including radioactive waste storage [69], geothermal energy production [70], oil and gas recovery [71–73] and geological CO_2 storage [74]. Modelling strategies in fractured networks are divided into two main categories depending on the representation of fractures, i. e., implicit or explicit. For the reactive process we discuss in this thesis, a model with an explicit representation of fractures is more appropriate. If the flow in the rock is negligible, discrete fracture networks (DFN) models are powerful tools to analyse the flow.

In the DFN approach, fractures are represented as two-dimensional planar objects in three dimensions and as one-dimensional objects in two dimensions. Therefore, the network is modelled as a lattice. The fractures in three dimension can be meshed as discussed in [75] to be used in a numerical method. One downside of DFN, however, is the high computation cost for meshing and solving large systems when the number of fractures grows. As an alternative strategy, it has been shown that graph theory and particle tracking can be used to model the flow and transport of a neutral component in both two and three-dimensional settings [76, 77]. This has led to a massive speed-up of simulations up to two orders of magnitude comparing to the other methods that involve meshing of fractures. Further improvements are possible using percolation theory to identify a 'backbone' for the network [78] and thus reducing the corresponding graph and to use machine learning algorithms to extract these backbones [79].

One of the major challenges in the simulation of fractured networks using graph theory is the treatment of the intersection of fractures. Fluid streams coming from different fractures can potentially mix at the intersections. There are two ways the intersections are treated. In the first method, it is assumed that the residence time is long enough that all the incoming streams reach equilibrium [71, 80]. The second approach, streamline routing, is the other extreme where the assumption is no mixing occurs and streamlines exit the intersection as they entered. It is also possible to consider an interpolation between these two extremes [81].

Precipitation and dissolution in the fractured networks is a multi-scale problem. The intersections are scaled by the aperture of the intersecting fractures while the length of a fracture can be several orders of magnitude higher than its aperture. While the chemical components are transported in the fractures, the mixing occurs only at the intersection of fractures. Mixing of different streams at an intersection is accompanied by chemical reactions which can lead to accumulation of precipitates and potentially clogging them. Hence, the flow and transport of ions greatly depend on the changes at the intersections.

1.4 THESIS OVERVIEW

The thesis is structured as follows; In Chapter 2, we provide the background information, i.e., method of characteristics, the chemical and the transport model and provide a discussion on diffusion/dispersion induced waves. Chapter 3 presents the solution to one-dimensional reactive transport for the case that precipitation changes the porosity. We develop the streamline simulator for the case that precipitation does not change the porosity and develop a mixing model for the well in Chapter 4. In Chapter 5, we use these tools in a discrete fracture network to understand parameters affecting clogging and to provide an efficient tool in the simulation of precipitation and dissolution in discrete fracture networks. Conclusion and further suggestions are summarised in Chapter 6.

2

REACTIVE TRANSPORT MODEL AND THE METHOD OF CHARACTERISTICS

In this chapter, we present a local equilibrium theory for the reactive transport of two salts that share an ion. The chemical model and the notations, which are referred to throughout this thesis, are introduced. In addition, a brief introduction to the method of characteristics is provided that is the building block for all the solutions discussed in the following chapters. Finally, we use the method of characteristics in the context of ion-exchange to show how linear transport and nonlinear reactions can lead to numerical artefacts.

For the chemical model, we assume all the stoichiometric coefficients are 1 for the sake of simplicity. However, all the derivations can be extended to any two chemical reactions with a shared ion at a little cost in mathematical complexity.

The discussion on the method of characteristic presented below is solely for the purpose of application for this thesis and is by no means comprehensive. The reader is thus referred to the classical textbooks on this topic [33, 42, 43, 82, 83].

2.1 CHEMICAL SYSTEM

Two equilibrium reactions are considered with ions A, B and X (e. g., Ca^{2+}, Ba^{2+} and SO_4^{2-}) forming immobile salt AX and BX ($CaSO_4$ and $BaSO_4$):

$$\mathrm{A} + \mathrm{X} \longleftrightarrow \mathrm{AX}, \qquad k_A = n_A n_X, \tag{2.1a}$$

$$\mathrm{B} + \mathrm{X} \longleftrightarrow \mathrm{BX}, \qquad k_B = n_B n_X, \tag{2.1b}$$

where n_A, n_B and n_X denote the molar concentration of ions A, B and X in the fluid per unit volume (e. g., mol/litre). We consider an isothermal system with equilibrium constants k_A and k_B. The assumption of equilibrium is valid for high values of Damköhler number, i. e., when the reaction rate in both directions are at least 10 times than that of the convection rate.

Here, we make the simplifying assumption that the amount of ion X is balanced by the two ions A and B, i. e.,

$$n_A + n_B = n_X. \tag{2.2}$$

Hence $N_A + N_B = N_X$ holds true and we will have two independent equations for A and B. In reality, however, inert ions exist in the solution which allow existance of all three ions in the solution independent of each other. Relaxing the above assumption would result in N_X being an independent variable and increasing the degrees of freedom by one. Therefore, the inert ions[1] are lumped together (as N_Ξ) and the charge balance would read

$$n_A + n_B = n_X + n_\Xi. \tag{2.3}$$

The saturation concentration for component A (or B) can be obtained by solving Equation (2.1a) (or Equation (2.1b)) in the absence of the other component to obtain

$$\tilde{n}_A := \sqrt{k_A}, \tag{2.4a}$$
$$\tilde{n}_B := \sqrt{k_B}, \tag{2.4b}$$

The concentrations $\hat{n}_A$, $\hat{n}_B$ when the fluid is saturated with both salts, are evaluated by solving Equations (2.1a) and (2.1b) simultaneously and are given by

$$\hat{n}_A := \frac{\tilde{n}_A^2}{\sqrt{\tilde{n}_A^2 + \tilde{n}_B^2}}, \tag{2.5a}$$
$$\hat{n}_B := \frac{\tilde{n}_B^2}{\sqrt{\tilde{n}_A^2 + \tilde{n}_B^2}}. \tag{2.5b}$$

2.2 STATE VARIABLES

We define the conserved variable or the total amount N_π of ion π per volume of porous medium as

$$N_A = \phi_F n_A + m_A, \tag{2.6a}$$
$$N_B = \phi_F n_B + m_B, \tag{2.6b}$$
$$N_X = \phi_F n_X + m_X, \tag{2.6c}$$

1 By inert ions, we mean the ions that are more much more soluble than AX and BX, for example if the two salts are two sulphates the inert ions are considered as Na^+ and Cl^-

where ϕ_F is the volume fraction that is occupied by the fluid and m_π is the amount of precipitate π per pore volume of the medium. By the amount of precipitate π, we mean the number of moles of all the salts that constitute ion π.

Given that N_π are defined as the primary (or state) variables, we need to express other quantities in terms of N_π. The expressions and thus the solution to the corresponding transport problem depends on whether or not the volume of the precipitates are accounted for. Each choice is the main assumption for Chapters 3 and 4. However, in both cases, the expression for the secondary variables can be categorised into four regions. Each region corresponds to a distinct status of the fluid in terms of saturation with respect to salts. These regions are

$AUBU$: The fluid is unsaturated with respect to both salts A and B.

$ASBU$: The fluid is saturated with salt A but is unsaturated with respect to B ions. Therefore, it may only contain A precipitate.

$AUBS$: This case is the reverse of $ASBU$. All the derivations referred to this case can be constructed by swapping A with B and vice versa. Therefore, unless specified differently, we discuss only $ASBU$. The results and derivations for region $AUBS$ follows accordingly.

$ASBS$: The fluid is saturated with both salts, and the concentration of ions in the fluid is constant ($\hat{n}_A, \hat{n}_B$). Any change in total concentration N_A, N_B changes the amount of precipitates.

The secondary variables, i. e., fluid concentrations ($n_A(N_A, N_B)$, $n_B(N_A, N_B)$) and the amount of precipitates ($m_A(N_A, N_B)$, $m_B(N_A, N_B)$) are expressed in terms of N_A and N_B for each region. Their explicit form is dependent on the assumption whether the precipitates take volume or not and are given in Appendices A.1 and A.4, respectively.

2.3 REACTIVE TRANSPORT MODEL

Mass conservation requires that any variation of total amount of an ion (N_π) within a volume is balanced by the net flux of that ion. We assume that the fluid and rock are incompressible and that precipitates are stationary. Hence, the flux of component π is given by the transport of the components in the fluid $\boldsymbol{v}n_\pi$, where $\boldsymbol{v}$ is the velocity vector. Therefore, the mass balance for each component reads as

$$\frac{\partial}{\partial t^*} N_\pi + \nabla_{\boldsymbol{x}^*} \cdot (\boldsymbol{v} n_\pi) = \nabla_{\boldsymbol{x}^*} \cdot (D \nabla_{\boldsymbol{x}^*} n_\pi), \qquad \boldsymbol{x}^* \in \mathbb{R}^3, t^* > 0, \tag{2.7}$$

where t^* and $\boldsymbol{x}^*$ are time and space, respectively and D is the diffusion coefficient. We assume that the Péclet is higher than 10 which means molecular diffusion

is dominated by convection. Hence, the right hand side of Equation (2.7) can be dropped. Using the charge balance (Equation (2.2)) and the fact that $m_X = m_A + m_B$, we can drop the mass balance equation for component X due to its linear dependency and reduce the system dimensions to 2×2.

Throughout this text, we refer to the vector of overall concentration as $\boldsymbol{N} = \begin{pmatrix} N_A \\ N_B \end{pmatrix}$. Similarly, $\boldsymbol{n}$ and $\boldsymbol{m}$ are used to refer to the vector of fluid concentration and amount of precipitates.

Assuming incompressibility of the medium and the fluid, Equation (2.7) is solved together with the continuity equation for the incompressible fluid

$$\nabla_{\boldsymbol{x}^*} \cdot \boldsymbol{v} = 0, \tag{2.8}$$

and Darcy's law

$$\boldsymbol{v} = -\boldsymbol{T}\nabla P, \tag{2.9}$$

where $\boldsymbol{T}$ is the transmissibility tensor and P is the pressure field, to solve the flow and transport for $t > 0$ and $\boldsymbol{x} \in D \subseteq \mathbb{R}^d$.

2.4 RIEMANN PROBLEMS AND THE METHOD OF CHARACTERISTICS

In this section, we provide a summary for method of characteristics for system of two one-dimensional PDEs. As mentioned in the beginning of this chapter, the discussion presented here is for a generic 2×2 hyperbolic system. The presented theory is relavant to the analyical solutions presented in Section 2.5 and in Chapters 3 and 4.

Consider the one-dimensional system

$$\frac{\partial \boldsymbol{q}}{\partial t} + \frac{\partial}{\partial x}\left[\boldsymbol{f}(\boldsymbol{q})\right] = 0, \qquad x \in \mathbb{R}^1,\ t > 0, \tag{2.10}$$

for vector quantity $\boldsymbol{q} \in \mathbb{R}^2$ and flux function $\boldsymbol{f} : \mathbb{R}^2 \mapsto \mathbb{R}^2, \boldsymbol{f} \in C^1$. This system of PDEs is called hyperbolic if all eigenvalues corresponding to the Jaccobian matrix, $\boldsymbol{\mathcal{J}}$, of function $\boldsymbol{f}$, i. e.,

$$\boldsymbol{\mathcal{J}} = \begin{pmatrix} \frac{\partial f_1}{\partial q_1} & \frac{\partial f_1}{\partial q_2} \\ \frac{\partial f_2}{\partial q_1} & \frac{\partial f_2}{\partial q_2} \end{pmatrix}, \tag{2.11}$$

are real. Moreover, the PDE system is *strictly hyperbolic* if the two eigenvalues are also distinct. The matrix $\boldsymbol{\mathcal{J}}$ depends on the vector quantity $\boldsymbol{q}$ and may not always satisfy the hyperbolicity conditions. Here, we assume that system in Equa-

tion (2.10) is strictly hyperbolic for all values of $\boldsymbol{q}$. If we provide the hyperbolic PDE (2.10) with the initial condition

$$\boldsymbol{q}(x,0) = \begin{cases} \boldsymbol{q}_l & x < 0, \\ \boldsymbol{q}_r & x > 0, \end{cases} \tag{2.12}$$

we have constructed the Riemann Problem for Equation (2.10). Here, $\boldsymbol{q}_l$ and $\boldsymbol{q}_r$ are constant and referred to as left and right data (or states), respectively. This system also is a conservation law with conserved variable $\boldsymbol{q}$.

For the given initial condition Equation (2.12), a strong solution does not exist for Equation (2.10). Yet, *weak solutions* exist in the sense that there are functions $\boldsymbol{q}(x,t)$ that satisfy the integral equation

$$\int_0^\infty \int_{-\infty}^\infty \psi \left\{ \frac{\partial \boldsymbol{q}}{\partial t} + \frac{\partial}{\partial x} \left[\boldsymbol{f}(\boldsymbol{q}) \right] \right\} \mathrm{d}x \, \mathrm{d}t = 0, \tag{2.13}$$

for certain smooth functions ψ. The *method of characteristics* is one way to seek these type of solutions.

The method of characteristic is a technique to solve a Riemann Problem by converting it to a set of ordinary differential equations (ODEs) along *characteristics*. The ODEs are then integrated to obtain the solution for a given final time. The characteristics are families of curves in x-t along which the solution is constant. In order to obtain the solution using the characteristics, a family of characteristics are mapped into a curve in the space of state variables. Hence, we also need to operate in q_1-q_2 plane, also known as phase space or hodograph plane. The hodograph is defined as the 'n-dimensional space of dependent variables' ([43]) which translates to q_1-q_2 plane for our problem. In the case that $\boldsymbol{q}$ is the vector of compositions, the curves in the hodograph plane are referred to as composition paths. The composition paths form a grid in the hodograph plane. Thus, in order to find the solution of the Riemann Problem with initial condition Equation (2.12), one seeks the "physical" path on the grid from $\boldsymbol{q}_l$ to $\boldsymbol{q}_r$.

The two characteristic equations, assuming the eigenvalues of the Jaccobian matrix of $\boldsymbol{f}$ are $\lambda_1(\boldsymbol{q}) < \lambda_2(\boldsymbol{q})$, reads as

$$\frac{\mathrm{d}x}{\mathrm{d}t} = \lambda_1, \tag{2.14a}$$

$$\frac{\mathrm{d}x}{\mathrm{d}t} = \lambda_2, \tag{2.14b}$$

which form the family of the two characteristics. We refer to the characteristics obtained from Equations (2.14a) and (2.14b) as 1-characteristics and 2-characteristics, respectively.

Recall that a constant state can be propagated by a characteristic from any of the two families. A travelling variation, i. e., a union of constant states that are propagated in space and time, are referred to as a *wave* and is denoted by $\mathcal{W}$. If a wave is propagated by 1-characteristics, then it is denoted by $\mathcal{W}_1$ or referred to as a slow wave because $\lambda_1 < \lambda_2$. A fast wave, $\mathcal{W}_2$ is propagated along 2-characteristics.

The solution along a characteristic for an initial state $\boldsymbol{q}$ yields *integral curves* which are denoted by $\mathcal{I}$ and are defined as

$$\mathcal{I}_p(t, \boldsymbol{q}) = \boldsymbol{q} + \int_0^t \boldsymbol{r}_p(\boldsymbol{q})\, \mathrm{d}\tau, \tag{2.15}$$

where $\boldsymbol{r}_p$ is the eigenvector for λ_p. Here, the assumption is that the eigenvalue λ_p does not decrease from the initial point $\boldsymbol{q}$ along the integral curve $\mathcal{I}_p$. If the eigenvalue is strictly increasing the characteristics fan out and the corresponding wave, also known as a *rarefaction wave* is a smooth variation of the quantity $\boldsymbol{q}$. The width of the rarefaction wave increases and the wave become smoother as it travels in the system. If on the other hand, the eigenvalue remains constant, the characteristic is a straight line and the corresponding wave, also known as a *contact discontinuity*, is a travelling discontinuity.

The solution obtained through Equation (2.15) is triple-valued and hence invalid if the eigenvalue is decreasing along the integral curve. Because the characteristic speed on the left side of the discontinuity is larger than that of the right side. Therefore, the solution must be a travelling discontinuity that retains its shape as it propagates. These waves are known as self-sharpening or *shock waves*. In this case, the curve along which we look for a solution is a straight line, similar to the case of a contact discontinuity. The slope of this straight line in x-t plane is the shock speed denoted by $\bar{v}$. Finally, the integral form of Equation (2.14) can be solved to obtain the solution with starting point $\boldsymbol{q}$

$$\mathcal{H}(\boldsymbol{q}) := \left\{ \boldsymbol{q}^* \middle| \boldsymbol{f}(\boldsymbol{q}^*) - \boldsymbol{f}(\boldsymbol{q}) = \bar{v}(\boldsymbol{q}^* - \boldsymbol{q}) \right\}. \tag{2.16}$$

Equation (2.16) is also known as the Rankine-Hugoniot condition and basically is a mass balance around the discontinuity from $\boldsymbol{q}$ to $\boldsymbol{q}^*$. The notation $\mathcal{H}$ stands for Hugoniot locus, i. e., the location of all $\boldsymbol{q}^*$ that satisfy Rankine Hugoniot condition.

The solution to the system of algebraic nonlinear equations, given by Equation (2.16), is not necessarily unique and can have several branches, i. e., for a given $\boldsymbol{q}$, there may be more than one $\boldsymbol{q}^*$ that honours Equation (2.16). However, only one solution is physical. One approach to obtain the correct and unique solution is to use the *vanishing viscosity method* [84]. Accordingly, the unique solution to the original parabolic equation with diffusion approaches to that of

its hyperbolic limit when the diffusion coefficient approaches zero [33]. Under certain circumstances (strictly convex flux function), this can be translated to the condition for eigenvalues around a shock [85]. Throughout this thesis, we use the *Lax Entropy Condition* to obtain the unique solution to Equation (2.16).

Lax Entropy Condition. *A discontinuity that separates states $\boldsymbol{q}_l$ and $\boldsymbol{q}_r$ and propagates with velocity $\bar{v}$ satisfies the Lax entropy condition if either of the inequalities below holds:*

$$\lambda_1(\boldsymbol{q}_l) > \bar{v} > \lambda_1(\boldsymbol{q}_r),$$
$$\lambda_2(\boldsymbol{q}_l) > \bar{v} > \lambda_2(\boldsymbol{q}_r).$$

For the sake of brevity, we use the notation $\mathcal{I}_1$ and $\mathcal{H}_1$ for the integral curves and Hugoniot loci for 1-characteristics, respectively. Waves corresponding to 1-characteristics are also denoted by $\mathcal{W}_1$, $\mathcal{C}_1$, $\mathcal{R}_1$ and $\mathcal{S}_1$ for a general wave, a contact discontinuity, a rarefaction or a shock, respectively. There will be no rarefaction waves in the dissolution and precipiation systems that we consider in the following chapters. Similar notations are used for 2-characteristic waves and curves.

In summary, we see that a family of characteristics maps to an integral curve or a Hugoniot locus for a given state $\boldsymbol{q}$ depending on the changes of the corresponding eigenvalue. The integral curves and Hugoniot loci form the composition grid in the hodograph plane. Hence, for the solution to the Riemann Problem Equation (2.10) with initial condition Equation (2.12), we seek to intersect $\mathcal{H}_1$ or $\mathcal{I}_1$ with $\mathcal{H}_2$ or $\mathcal{I}_2$ to obtain the physical path. The intersection point denoted by $\boldsymbol{q}_i$ (or $\boldsymbol{N}_i$ in following chapters) is the constant state that appears between $\mathcal{W}_1$ and $\mathcal{W}_2$. The solution is represented as

$$\boldsymbol{q}_l \xrightarrow{\mathcal{W}_1} \boldsymbol{q}_i \xrightarrow{\mathcal{W}_2} \boldsymbol{q}_r. \tag{2.17}$$

For flux functions that are not strictly convex, it may happen that a wave is compound, i. e., it comprises two or more waves of different type. Compound waves appear in the form of shock-rarefaction in multiphase flow. Compound waves that appear in the systems studied here have a shock-contact or contact-shock structure. Therefore, an additional intermediate point appears and we adopt the notation

$$\boldsymbol{q}_l \xrightarrow{\mathcal{C}_1} \boldsymbol{q}_{i1} \xrightarrow{\mathcal{S}_1} \boldsymbol{q}_{i2} \xrightarrow{\mathcal{W}_2} \boldsymbol{q}_r, \tag{2.18}$$

if $\mathcal{W}_1$ is compound or

$$\boldsymbol{q}_l \xrightarrow{\mathcal{W}_1} \boldsymbol{q}_{i1} \xrightarrow{\mathcal{S}_2} \boldsymbol{q}_{i2} \xrightarrow{\mathcal{C}_2} \boldsymbol{q}_r, \tag{2.19}$$

if $\mathcal{W}_2$ is compound.

2.5 DIFFUSION INDUCED WAVES IN NONLINEAR PROCESSES

In this section, we will show through an example how non-linearities can create additional waves. These waves may not actually exist in real systems with negligible diffusion, though they appear and dominate the pattern due to the numerical artefact caused by low order numerical methods. The example we consider here is an ion-exchange problem. We solve the problem using the method of characteristics presented in the previous section and compare the results with the one obtained from CMG-GEM Simulator on a coarse and fine space resolution, respectively. The coarse resolution on CMG-GEM is exaggerated to magnify this effect.

Consider the ion-exchange chemical reaction

$$\mathrm{Na}^+ + \tfrac{1}{2}\mathrm{CaX}_2 \leftrightarrow \tfrac{1}{2}\mathrm{Ca}^{2+} + \mathrm{NaX} \tag{2.20}$$

in equilibrium. We assume the solid phase has no vacant site on its surface therefore at all times

$$\tilde{q}_1 + 2\tilde{q}_2 \equiv Z_e, \tag{2.21}$$

where $\tilde{q}_i$'s are the concentration of the species (1 for NaX and 2 for CaX_2) on solid surfaces in moles per volume of solid and Z_e is the total capacity (exchanger sites) of the surface. In addition, summation of the cations should be equal to that of anions and therefore,

$$\tilde{c}_1 + 2\tilde{c}_2 = c_{\text{anion}}, \tag{2.22}$$

where $\tilde{c}_1$ and $\tilde{c}_2$ are the concentration of Na^+ and Ca^{2+}, respectively. We can use equivalent concentrations $q_i = e_i\tilde{q}_i$, $c_i = e_i\tilde{c}_i$ to write Equation (2.21) in the normalised form

$$q_1 + q_2 = 1. \tag{2.23}$$

From Equation (2.20) according to [86] we obtain the equilibrium constant to be

$$k = \sqrt{\frac{q_2}{c_2}}\left(\frac{c_1}{q_1}\right). \tag{2.24}$$

Combining Equations (2.23) and (2.24) yields

$$q_1 = \frac{c_1}{2k^2c_2}\left(\sqrt{c_1^2 + 4k^2c_2} - c_1\right), \tag{2.25a}$$

$$q_2 = 1 - \frac{c_1}{2k^2c_2}\left(\sqrt{c_1^2 + 4k^2c_2} - c_1\right). \tag{2.25b}$$

The total concentration of components are defined as

$$a_i = c_i + q_i. \tag{2.26}$$

We consider the one-dimensional transport of components for which the mass balance in a porous medium with porosity ϕ reads

$$\frac{\partial(\phi \boldsymbol{a})}{\partial \tilde{t}} + \frac{\partial(v\boldsymbol{c})}{\partial \tilde{x}} = 0, \quad 0 \leq \tilde{x} \leq L,\ \tilde{t} > 0, \tag{2.27}$$

where $\boldsymbol{a} = [a_1\, a_2]^T$ and $\boldsymbol{c} = [c_1\, c_2]^T$. Assuming incompressibility for fluid and rock in a homogeneous medium, Equation (2.27) can be recast in the form of quasi-linear hyperbolic equation ([87, 88]) using the dimensionless variables $x = \tilde{x}/L$ and $t = v\tilde{t}/(\phi L)$

$$\boldsymbol{A}\frac{\partial \boldsymbol{c}}{\partial t} + \frac{\partial \boldsymbol{c}}{\partial x} = 0, \quad 0 \leq x \leq 1,\ \tilde{t} > 0, \tag{2.28}$$

where $\boldsymbol{A}$ is the Jacobian matrix of the vector $\boldsymbol{a}$ with respect to $\boldsymbol{c}$ and therefore

$$\boldsymbol{A} = \begin{pmatrix} 1 + \frac{\partial q_1}{\partial c_1} & \frac{\partial q_1}{\partial c_2} \\ \frac{\partial q_2}{\partial c_1} & 1 + \frac{\partial q_2}{\partial c_2} \end{pmatrix}. \tag{2.29}$$

The setup for the problem is as follows: we consider a medium with dimensions $1025 \times 1000 \times 30$ meters in x,y and z direction, as depicted in Figure 2.1. The fluid with uniform concentration $\boldsymbol{c}_r = \begin{bmatrix} c_1^r & c_2^r \end{bmatrix}^T$ (referred to as initial condition, initial fluid or right data) is at rest and a new fluid with concentration $\boldsymbol{c}_l = \begin{bmatrix} c_1^l & c_2^l \end{bmatrix}^T$ (referred to as boundary condition, injection fluid or left data) is injected at $x = 0$. The concentration of ions on the surface and hence the total concentration in a unit volume of fluid can be calculated from Equation (2.25) and eq. (2.26) for both fluids. Here, we state the initial conditions but do not give the calculations of other secondary components are as they are trivial.

The eigenvalues of $\boldsymbol{A}$ (shown by σ_i) represent the retardation of the system and are the inverse of the velocity (λ_i) of the system. The eigenvalues are $\sigma_1 = \frac{\partial a_1}{\partial c_1} + \frac{\partial a_2}{\partial c_2} - 1$ and $\sigma_2 = 1$. The first eigenvalue due the definition of a_i in Equation (2.26) is $\sigma_1 = \frac{\partial q_1}{\partial c_1} + \frac{\partial q_2}{\partial c_2} + 1$, therefore $\sigma_1 > \sigma_2$ which implies $\lambda_1 < \lambda_2$. Figure 2.2 illustrates the integral curves in c_1-c_2 plane. It can be shown that the fast and slow integral

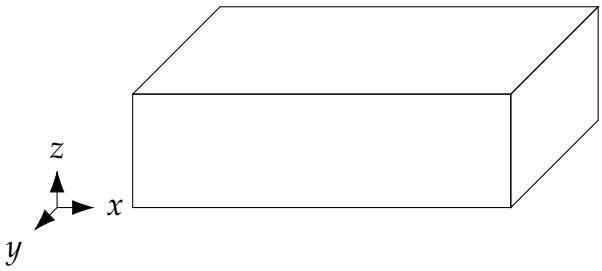

Figure 2.1: Sketch of the domain for the ion-exchange problem. The lenght in x, y and z directions are 1025, 1000 and 30, respectively. Injected fluid enters from the left at $x = 0$.

curves, which correspond to σ_1 and σ_2, are parabolas and lines, respectively in this plane. The Hugoniot loci curves coincide with the integral curves for 1-characteristics, because the $\mathcal{I}_1$ are straight lines [89]. Same holds true for 2-characteristics because σ_2 is constant, (i. e., linearly degenerate).

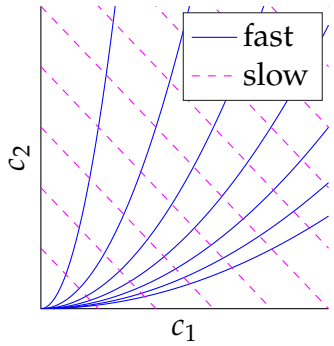

Figure 2.2: Fast (solid blue) and slow (dashed magenta) integral curves on the hodograph plane. The Hugoniot loci for each fields coincide with the corresponding family of integral curves of that field.

The solution to the Riemann Problem is a rarefaction (or a shock) followed by a contact discontinuity. The rarefaction or the shock is the retarded wave along which ion-exchange occurs. This wave is sometimes referred to as the *cation wave*. The fast wave travels with the velocity of the flow ($\lambda_2 = 1$) and is referred to as the *anion wave*. Along the fast wave, which reaches the production well first, no ion exchange occurs. Hence, in the absence of dispersion, profile (or history) of the equivalent fractions, q_1 and q_2, have at most one discontinuity.

The numerical setup for the problem is as follows: the reservoir is discretised only in x direction, hence length of $dy = 1000$ and $dz = 30$. We consider two discretisations: for the coarse resolution, we take $dx = 25$ and hence we have $41 \times 1 \times 1$ blocks. The other discretisation is five times finer and $dx = 5$ and there are $205 \times 1 \times 1$ blocks. For all problems we assume the injected fluid has molal concentration $\boldsymbol{c}_I = \binom{81.81977}{1.11749} \cdot 10^{-4} \frac{\text{mol}}{\text{kg}}$. To compare the analyical solution with the one obtained from CMG-GEM, we focus on the history or profile of $\boldsymbol{q}$ rather than $\boldsymbol{c}$. From the eigenvalue analysis, we expect to observe maximum

one discontinuity in the history of q which accounts for the retarded shock (or rarefaction) anion wave, in case they exist in the solution.

For the first example, we assume the initial molal concentration (mol/kg) of Ca^{2+} and Na^{+} are $6.304443 \cdot 10^{-3}$ and 1.015920087, resepectively which are balanced by Cl^{-} in an uncharged solution. The results from the CMG-GEM Simulator with coarse resolution suggests that a travelling bump in the profile of q_2 appears. The additional waves in Figure 2.3a are not consistent with mesh refinement as illustrated in Figure 2.3b.

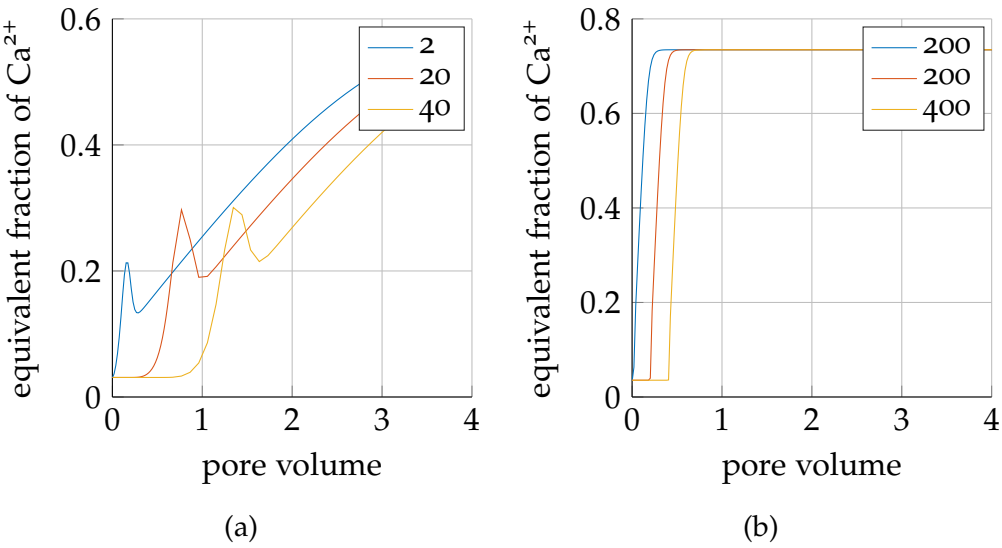

Figure 2.3: History of equivalent fraction at different grid blocks using GEM for the ion-exchange problem discussed in [90] $c_l = \binom{81.81977}{1.11749} \cdot 10^{-4} \frac{\text{mol}}{\text{kg}}$, $c_l = \binom{1.0159}{6.30 \cdot 10^{-3}} \frac{\text{mol}}{\text{kg}}$ with mesh size (a): $41 \times 1 \times 1$ blocks and (b): $1025 \times 1 \times 1$ blocks. The numbers in the legend show the number of the block in x direction.

It can be proved that if the initial condition and the boundary condition have the same Gapon ratio, i. e.,

$$\left(\frac{\sqrt{c_2}}{c_1}\right)_l = \left(\frac{\sqrt{c_2}}{c_1}\right)_r \Rightarrow \begin{pmatrix} q_1 \\ q_2 \end{pmatrix}_l = \begin{pmatrix} q_1 \\ q_2 \end{pmatrix}_r, \tag{2.30}$$

the history of equivalent fractions is a straight horizontal line. This holds true, because no ion exchange happens in this system. Therefore, if there is no diffusion, we have transport of two neutral components. However, in reality diffusion can change the balance of ions on the either side of the front which induces ion exchange and hence an additional wave. To illustrate this case, we have changed the initial condition to $c_r = \binom{1.015920087}{1.722845098} \frac{\text{mol}}{\text{kg}}$, i. e., we have only increased the concentration of Ca^{2+} so that Equation (2.30) holds true. The result on the coarse and fine mesh can be seen in Figures 2.4a and 2.4b. As before, we can see that refining the mesh tends to merge the additional waves.

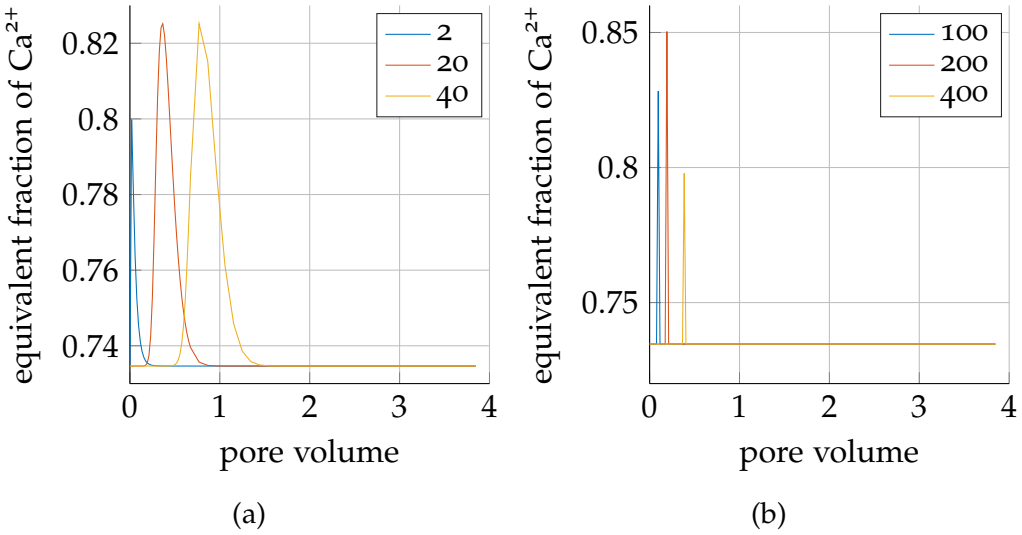

Figure 2.4: History of equivalent fraction at different grid blocks using GEM for an ion-exchange problem with same Gapon ratio (only concentration of Ca^{2+} of the initial fluid from Figure 2.3 is changed to 1.016) with mesh size (a): $41 \times 1 \times 1$ blocks and (b): $1025 \times 1 \times 1$ blocks. The numbers in the legend show the number of the block in x direction.

The diffusion-induced ion-exchange phenomena was initially introduced by [39]. Accordingly, when the ratio of rate of advection over that of diffusion (i. e., the corresponding Péclet number) is within a certain range, diffusion induces an extra wave. However, for very low values P'eclet numbers diffusion completely dominates the advective flow. For advection dominated reactive flow, low-order numerical methods (or simulation on a coarse grid) may result in purely numerical artefacts.

3

PRECIPITATION AND DISSOLUTION

In this chapter, we provide the Riemann Solution corresponding to Equation (2.7) on page 9 in one dimension. Here, we account for the volume of precipitates in the medium. Therefore, the porosity is allowed to change. We assume a one-dimensional domain of length L is initially filled with a fluid with an overall concentration of $\boldsymbol{N}_r$. The amount of precipitates and the concentration of an ion in the fluid at $t = 0$ can be back-calculated from the value of $\boldsymbol{N}_r$. The boundary condition for this problem is the injection of a new fluid with constant overall concentration $\boldsymbol{N}_l$ at $x = 0$ at a constant flow rate. While it is important to mention again, that all the precipitates are assumed stationary and in principle, only the mobile components are injected and not the precipitates associated with the boundary condition, it still makes sense to take $\boldsymbol{N}_l$ as the boundary condition. This is because such a boundary condition appears in initial conditions that are more than a step function, as shown in Section 3.2.1. Hence, Riemann Problems are the building block for the solution with general initial conditions and it is necessary to analyse all the cases.

3.1 PHYSICAL AND CHEMICAL MODEL

The main assumption in this chapter is that the porosity of the medium is allowed to change when precipitation or dissolution occurs. However, the liquid-solid solution is assumed to be an ideal solution, i. e., a given mass of salt takes the same volume both as a solid phase and as a solute in the solution. Hence, the Darcy velocity is constant throughout the medium.

Since we account for the volume of the precipitates, their amount (m_A, m_B) can be expressed by their molar densities (ω_A, ω_B) and volume fractions (ϕ_A, ϕ_B). Therefore, the definition of the conservative variables can be recast to

$$N_A = n_A \phi_F + \omega_A \phi_A, \tag{3.1}$$

$$N_B = n_B \phi_F + \omega_B \phi_B. \tag{3.2}$$

Since we assume ideality of the solution (i. e., the total volume remains constant after chemical reaction) and incompressibility of the medium and the fluid, volume conservation holds true. It reads

$$\phi_F = \phi_P - \phi_A - \phi_B, \tag{3.3}$$

where ϕ_P is the initial porosity of the rock without any precipitates.

The mass balance or the transport model Equation (2.7) on page 9 in one dimension reads,

$$\frac{\partial}{\partial t^*} N_\pi + \frac{\partial}{\partial x^*} (v_x n_\pi) = 0, \qquad 0 \leq x^* \leq L, t^* > 0. \tag{3.4}$$

where v_x is the component of the velocity field that is parallel to the direction of the flow. Since the Darcy velocity is constant we can obtain the dimension-less from of Equation (3.4) by defining $x = x^*/L$ for space and $t = q^* t^*/L$ for time, where L is the length of the medium,

$$\frac{\partial N_\pi}{\partial t} + \frac{\partial n_\pi}{\partial x} = 0, \qquad 0 \leq x \leq 1, t > 0. \tag{3.5}$$

Next, we want to identify the four regions for the status of the fluid (c.f. Section 2.2 on page 8) on the hodograph plane. In order to obtain expressions for the curves that separate the four regions, we need to eliminate n_A and n_B. Therefore, with $\phi_A = 0$ and solving Equation (2.6a) for n_A (and $\phi_B = 0$ and solving Equation (2.6b) for n_B) we obtain

$$n_A = \frac{N_A}{\phi_P - \phi_B}, \tag{3.6a}$$

$$n_B = \frac{N_B}{\phi_P - \phi_A}. \tag{3.6b}$$

Using $\phi_B = 0$ and $\phi_A = 0$ in Equations (3.6a) and (3.6b) and replacing them in Equation (2.4a), we obtain a relation $N_B(N_A)$ for the branch of the curve where B is unsaturated, A^{BU}. Using $\phi_A = 0$ and $n_A = \hat{n}_A$ in Equation (2.6a), we obtain an expression for $\phi_B(N_A)$ which we insert in Equation (2.6b) with $n_B = \hat{n}_B$ to obtain a relation $N_B(N_A)$ for the branch of the curve where B is saturated, A^{BS}:

$$N_B(N_A) = \begin{cases} \frac{\phi_P^2 \tilde{n}_A^2}{N_A} - N_A, & \text{for B unsaturated } (A^{BU}), \\ \frac{\hat{n}_B - \omega_B}{\hat{n}_A} N_A + \phi_P \omega_B, & \text{for B saturated } (A^{BS}). \end{cases} \tag{3.7}$$

Analogue to above, we can get the two other separating curves and obtain:

$$N_A(N_B) = \begin{cases} \frac{\phi_P^2 \tilde{n}_B^2}{N_B} - N_B, & \text{for A unsaturated } (B^{AU}), \\ \frac{\hat{n}_A - \omega_A}{\hat{n}_B} N_B + \phi_P \omega_A, & \text{for A saturated } (B^{AS}). \end{cases} \tag{3.8}$$

With the separating curves defined, we can identify the four regions as

$$AUBU = \left\{ (N_A, N_B) \,|\, N_A \leq B^{AU}(N_B),\, N_B \leq A^{BU}(N_A) \right\}, \tag{3.9a}$$

$$ASBU = \left\{ (N_A, N_B) \,|\, N_A \leq B^{AS}(N_B),\, N_B \geq A^{BU}(N_A) \right\}, \tag{3.9b}$$

$$AUBS = \left\{ (N_A, N_B) \,|\, N_A \geq B^{AU}(N_B),\, N_B \leq A^{BS}(N_A) \right\}, \tag{3.9c}$$

$$ASBS = \left\{ (N_A, N_B) \,|\, N_A \geq B^{AS}(N_B),\, N_B \geq A^{BS}(N_A) \right\}. \tag{3.9d}$$

All regions lie within the triangular domain

$$\left\{ N_A \geq 0,\, N_B \geq 0,\, N_A + \frac{\omega_A}{\omega_B} N_B < \omega_A \phi_P \right\}. \tag{3.10}$$

Figure 3.1 shows the hodograph plane with the separating curves Equations (3.7) and (3.8). For illustrative purposes, throughout this chapter, we choose $k_A = 1\frac{\text{mol}^2}{\text{lit}^2}$, $k_B = 0.67\frac{\text{mol}^2}{\text{lit}^2}$, $\omega_A = 3\frac{\text{mol}}{\text{lit}}$, $\omega_B = 2\frac{\text{mol}}{\text{lit}}$, $\phi_P = 0.4$, unless stated otherwise. We denote the intersection of the curves from Equations (3.7) and (3.8) as $\boldsymbol{N}_t = \begin{pmatrix} \phi_P \hat{n}_A \\ \phi_P \hat{n}_B \end{pmatrix}$ (Equation (2.5)); at this value, the fluid is saturated with both salts but there is no precipitate of either. The two points in the hodograph plane $\begin{pmatrix} \phi_P \omega_A \\ 0 \end{pmatrix}$ and $\begin{pmatrix} 0 \\ \phi_P \omega_B \end{pmatrix}$ and the line connecting them are the union of limit points where $\phi_P = \phi_A + \phi_B$, i. e., the porous medium is completely filled with precipitates. Therefore, the fractions in Equation (3.6) are definite since the denominator is always nonzero. Clearly, points above the line connecting the two corner points are unphysical because the corresponding volume of precipitates is larger than the pore space.

Here, we seek the Riemann solution to Equation (3.5) with initial condition

$$\boldsymbol{N}(x, 0) = \begin{cases} \boldsymbol{N}_l & x < 0, \\ \boldsymbol{N}_r & x > 0, \end{cases} \tag{3.11}$$

where $\boldsymbol{N}$ is the composition vector $\begin{pmatrix} N_A \\ N_B \end{pmatrix}$ and the subscripts r and l refer to right fluid (downstream) and left fluid (upstream or the injected fluid), respectively. Throughout this thesis, we refer to a given fluid overall composition $\boldsymbol{N}$ as state $\boldsymbol{N}$. If a state is associated with a point in the hodograph plane, say $\boldsymbol{N}_p$, the co-

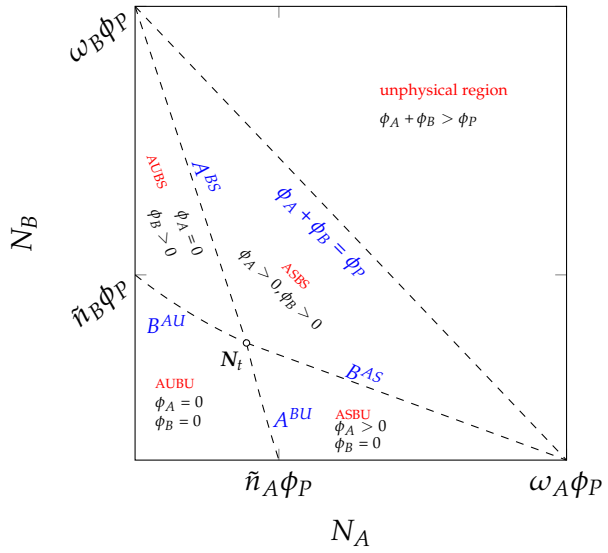

Figure 3.1: Phase plane (hodograph plane) and the separating curves defined in Equation (3.7) and Equation (3.8) for parameter values $k_A = 1\frac{\text{mol}^2}{\text{lit}^2}$, $k_B = 0.67\frac{\text{mol}^2}{\text{lit}^2}$, $\omega_A = 3\frac{\text{mol}}{\text{lit}}$, $\omega_B = 2\frac{\text{mol}}{\text{lit}}$ and $\phi_P = 0.4$. The diagonal line ($\phi_A + \phi_B = \phi_P$) is the limit line at which porosity vanishes. Each of the regions $AUBU$, $ASBU$, $AUBS$ and $ASBS$ are bounded by the separating curves and the main axes.

ordinates are labelled as N_A^p and N_B^p. A similar notation is used for concentration of ions in the fluid and the amount of precipitates, i. e., $\begin{pmatrix} n_A^p \\ n_B^p \end{pmatrix}$ and $\begin{pmatrix} \phi_A^p \\ \phi_B^p \end{pmatrix}$.

This section presents the analysis of the possible waves for the system of Equations (3.5). For simplicity and illustration, we first treat the single reaction case where $N_B = n_B = \phi_B = 0$.

3.2.1 *Single reaction*

When ion B is not present, the fluid is either unsaturated with salt A ($\phi_A = 0$ and $N_A = \phi_F n_A = \phi_P n_A$) or it is saturated and there is precipitate $\phi_A \geq 0$. The saturated fluid composition is $n_A = 1/\sqrt{k_A} = \tilde{n}_A$ (c.f. Equation (2.1a)). Therefore, $N_A = \phi_F \tilde{n}_A + \phi_A \omega_A = (\phi_P - \phi_A)\tilde{n}_A + \phi_A \omega_A$ and

$$\phi_A(N_A) = \frac{N_A - \phi_P \tilde{n}_A}{\omega_A - \tilde{n}_A}, \tag{3.12}$$

where due to our assumption, $\omega_A > \tilde{n}_A$, the above fraction is always well defined.

The resulting conservation equation for a single component is

$$\frac{\partial N_A}{\partial t} + \frac{\partial}{\partial x} n_A(N_A) = 0. \tag{3.13}$$

Its quasi-linear form reads

$$\frac{\partial N_A}{\partial t} + \frac{dn_A}{dN_A}\frac{\partial N_A}{\partial x} = 0, \tag{3.13a}$$

where

$$\frac{\mathrm{d}n_A}{\mathrm{d}N_A} = \begin{cases} 0 & N_A > \phi_P \tilde{n}_A, \\ \frac{1}{\phi_P} & N_A < \phi_P \tilde{n}_A. \end{cases} \tag{3.13b}$$

The flux function, n_A is not differentiable at $N_A = \phi_P \tilde{n}_A$, and we need to use the integral form of mass conservation to seek the weak solution [82]. In addition, since the flux function n_A is piece-wise linear and has a monotonic derivative (c.f. Figure 3.2), the solution to the Riemann Problem is either a shock or a series of contact discontinuities [83, 91].

The single reaction case has 3 classes of solutions to the Riemann Problem.

1) The solution is a contact discontinuity when $\left.\frac{\mathrm{d}n_A}{\mathrm{d}N_A}\right|_{\boldsymbol{N}_l} = \left.\frac{\mathrm{d}n_A}{\mathrm{d}N_A}\right|_{\boldsymbol{N}_r}$ that travels with constant velocity $\left.\frac{\mathrm{d}n_A}{\mathrm{d}N_A}\right|_{\boldsymbol{N}_l}$, i. e., $\boldsymbol{N}_l \xrightarrow{\mathcal{C}} \boldsymbol{N}_r$. This case corresponds to transport of inerts in a single phase flow.

2) Two contact discontinuities when $\left.\frac{\mathrm{d}n_A}{\mathrm{d}N_A}\right|_{\boldsymbol{N}_l} < \left.\frac{\mathrm{d}n_A}{\mathrm{d}N_A}\right|_{\boldsymbol{N}_r}$: the first is stationary and the second one travels with velocity $\frac{1}{\phi_P}$. In this case, a constant intermediate state appears between the two fronts, i. e., $\boldsymbol{N}_l \xrightarrow{\mathcal{C}} \boldsymbol{N}_i \xrightarrow{\mathcal{C}} \boldsymbol{N}_r$. The intermediate state $\boldsymbol{N}_i$ is the saturation concentration.

3) A shock wave when $\left.\frac{\mathrm{d}n_A}{\mathrm{d}N_A}\right|_{\boldsymbol{N}_l} > \left.\frac{\mathrm{d}n_A}{\mathrm{d}N_A}\right|_{\boldsymbol{N}_r}$ that travels according to Rankine-Hugoniot condition, $\boldsymbol{N}_l \xrightarrow{\mathcal{S}} \boldsymbol{N}_r$. This case corresponds to dissolution of a salt by unsaturated fluid. This shock corresponds to a wave that completely dissolves the salt upon propagation.

Figure 3.2 provides an illustrative example for two Riemann Problems; a region of precipitate with total concentration N_A^q is surrounded by an unsaturated fluid with a total concentration N_A^p. Figure 3.2a shows the initial and a later profile of the total concentration. The first jump from N_A^p to N_A^q initially at x_1 belongs to the third category and is a shock. This shock travels to x_2 with a velocity equal to $\bar{v}$ and therefore $x_2 - x_1 = \bar{v}(t_2 - t_1)$. The second jump from N_A^q to N_A^p on x_3 belongs to the second category. In this case, the discontinuity propagates according to the derivative of the flux function. Since there is a discontinuity in the derivative, the solution wave is composed of two parts: the first part (from N_A^q to $\phi_P \tilde{n}_A$) is stationary while the other part (from $\phi_P \tilde{n}_A$ to N_A^p) travels with fluid velocity $(1/\phi_P)$. The discontinuity of the velocity at $N_A = \phi_P \tilde{n}_A$ is shown in Figure 3.2b. This point is the total concentration of the saturated fluid. Therefore, the front separating the saturated and the unsaturated fluid moves away to x_4 whereas the right bank stays at x_3 until the shock wave reaches it.

3.2.2 *Two Reactions (2×2 system)*

The Riemann Problem for Equation (3.5) for the continuous case in quasi-linear form reads

$$\frac{\partial \boldsymbol{N}}{\partial t} + \boldsymbol{\mathcal{J}}(\boldsymbol{N})\frac{\partial \boldsymbol{N}}{\partial x} = 0, \qquad t > 0,\, 1 > x > 0 \tag{3.14a}$$

$$\boldsymbol{N}(x,0) = \begin{cases} \boldsymbol{N}_l & x < 0, \\ \boldsymbol{N}_r & x > 0, \end{cases} \tag{3.14b}$$

$$\boldsymbol{N}(0,t) = \boldsymbol{N}_l, \qquad t > 0 \tag{3.14c}$$

The functions n_A and n_B do not always have strong derivatives across the boundary curves (Equations (3.7) and (3.8)) [82], because these functions take different forms in different regions that are continuous but not continuously differenti-

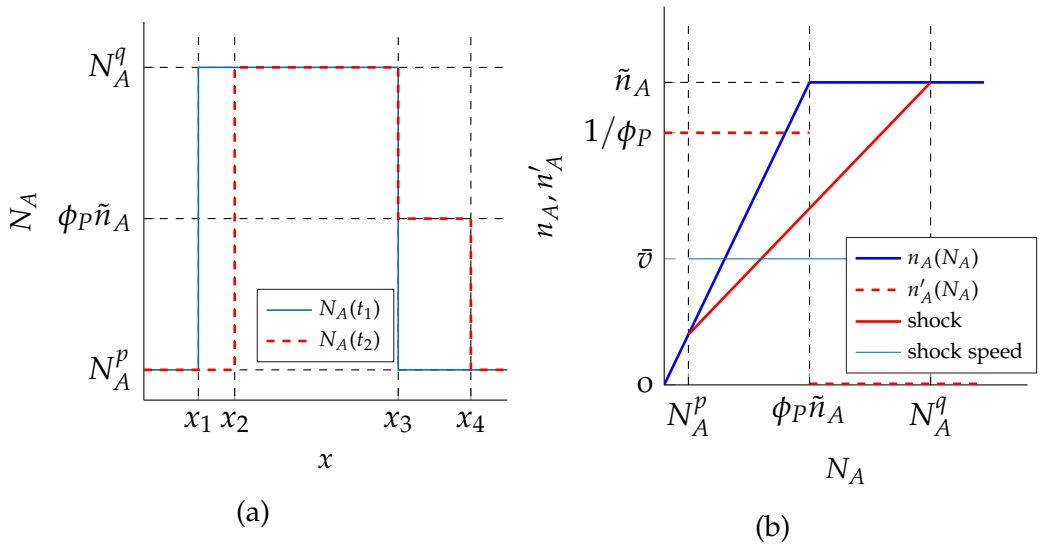

Figure 3.2: (a) Distribution of total concentration at initial time t_1 (solid blue) and at t_2 (dashed red) for a batch of precipitate A (concentration N_A^q) bounded from both sides by unsaturated fluid (N_A^p). The total concentration for the saturated fluid is shown by a horizontal black dashed line. (b) Flux function vs. total concentration (thick solid blue) and its derivative (dashed red), shock composition path (solid red) and its slope (thin solid blue) for the same problem.

able (c.f. Appendix A.1). Therefore, special care needs to be taken when the end points of a wave lie in different regions.

3.2.2.1 *Eigenvalue analysis and composition paths*

The details of the calculation including the entries of the Jacobian matrix, eigenvalues, integral curves and Hugoniot loci are given in the appendix (Appendices A.1 to A.3). In this subsection, we provide a summary of the mathematical character of the two classes of waves in the four different regions.

In the region $AUBU$, the eigenvalues are identical, $\lambda_1 = \lambda_2 \equiv 1/\phi_P$, and the system is diagonalisable. Therefore, every point is an umbilical point [92]. In this case, the two linear transport equations can be decoupled. The solution to the system is also a contact discontinuity because the solution for each transport equation is a contact discontinuity. Also, every direction is an integral curve.

In the region $ASBU$, $\lambda_1 = 0$ and $\lambda_2 = \frac{1}{\phi_P - \phi_A}$ and so the system is strictly hyperbolic. Figure 3.3 illustrates the integral curves in regions $ASBU$ and $AUBS$. The slow integral curves $\mathcal{I}_1$ are straight lines emerging from $\begin{pmatrix} \omega_A\phi_P \\ 0 \end{pmatrix}$ and are depicted by dashed red lines in Figure 3.3. Along these lines, and therefore along the slow waves, the concentration of chemicals in the fluid is constant while the amount of precipitate changes. The fast integral curves $\mathcal{I}_2$, on the other hand, are iso-porosity curves along which the concentration in the fluid changes according to Equation (2.1). The curves for $\mathcal{I}_2$ are represented by solid blue lines.

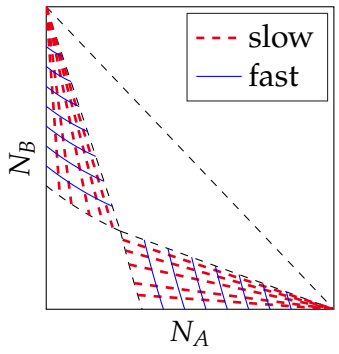

Figure 3.3: Slow (dashed red) and fast (solid blue) integral curves in the hodograph plane for points in the regions $ASBU$ and $AUBS$

The Jacobian matrix in region $ASBS$ is zero because the concentrations of the two ions in the fluid are constant as long as the fluid is saturated with both solid phases. Therefore, the flux function is constant and Equation (3.14) turns into a local ODE for time. However, we shall look at it as a *non-strictly* hyperbolic system with both eigenvalues equal to zero. Hence, all precipitate variations (discontinuities in initial condition) remain stationary.

Figure 3.4a shows the slow Hugoniot locus $\mathcal{H}_1$ for a point in $AUBU$. Any variation inside $AUBU$ is a contact discontinuity. This is equivalent to the transport of two tracers without any chemical reactions. However, if the right state belongs to another region, a shock develops, because $1/\phi_P = \lambda_1(\boldsymbol{N}_l) > \lambda_1(\boldsymbol{N}_r) = 0$. A shock develops as a result of the dissolution of a salt. In general, for a point in $AUBU$, there are three branches of $\mathcal{H}_1$ curves in the other three regions: two lines emerging from the corner points in regions $ASBU$ and $AUBS$ and the line in $ASBS$ that passes through the point itself and $\boldsymbol{N}_t$. A 2-shock with the left state in $AUBU$ and the right state in $ASBU/AUBS$ is not admissible because it violates the Lax condition. Slow shocks are shown by dashed red straight lines.

For points in the region $ASBU$, $\mathcal{H}_1$ coincides with $\mathcal{I}_1$ because the latter are straight lines [89]. A slow shock with the left state in $ASBU$ and right state in any other region violates the Lax condition. A fast shock with the left state in $ASBU$ is admissible if the right state lies in $ASBS$. Figure 3.4b illustrates fast shocks for four points in $AUBS$ and $ASBU$. The Hugoniot loci $\mathcal{H}_2$ with the left state in $ASBU$ coincide with $\mathcal{I}_2$ in the region $ASBU$ and are straight lines in the region $ASBS$. The slope of this line depends on the left state, (see Equation (3.16) in the Section 3.2.3). The Hugoniot loci $\mathcal{H}_2$ in hodograph plane are depicted as blue lines.

Two regions α and β in Figure 3.4 are highlighted in blue and green colour, respectively. These two regions are particularly interesting to us. A discontinuity with one of its end-points in any of these regions develops a non-coherent wave. The non-coherent wave then breaks into a *compound wave*. Presence of a compound wave in this system creates an additional constant state. The ex-

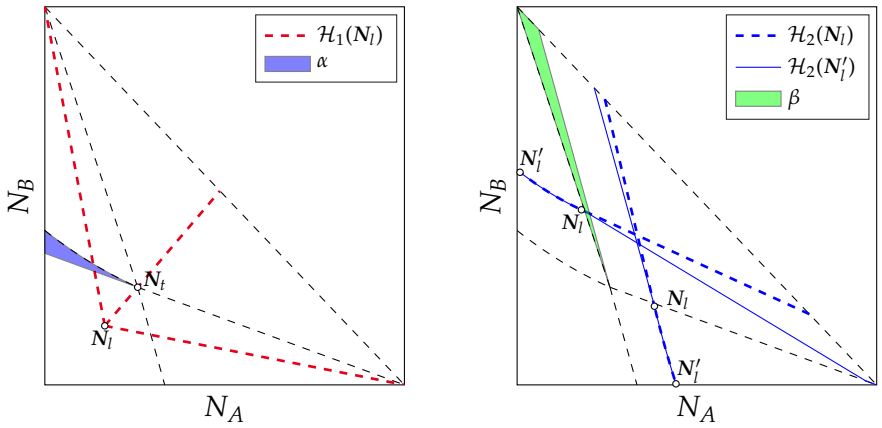

Figure 3.4: (a) Slow shock curves for the left state in $AUBU$ and the right state in the other three regions. If $\boldsymbol{N}_l$ lies in region α, then the branch of $\mathcal{H}_1$ in $ASBU$ is not possible. (b) Fast shock curves (solid and dashed blue) for two left states in $ASBU$ and two in $AUBS$ and right states in $ASBS$.

istence of regions α and β depends on the curvature of the boundary curves (Equations (3.7) and (3.8)). These regions and their corresponding solution are discussed in the section Solution to Riemann Problem (Cases 11 to 16).

Figure 3.5 shows examples of solutions to the algebraic equation for $\mathcal{H}$ that are not physically admissible. In general, a shock with the left state in a region with more precipitate violates the entropy condition and is not admissible. In addition, for any point in $ASBU$, there is a detached branch of $\mathcal{H}$ in the region $AUBS$ (and for any point in $AUBS$ a detached branch in $ASBU$). Solutions on the detached $\mathcal{H}$ branch are not admissible either, because they violate the entropy condition.

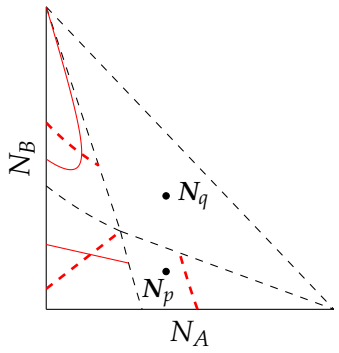

Figure 3.5: Detached Hugoniot locus $\mathcal{H}$ in $AUBS$ for a state $\boldsymbol{N}_p$ and inadmissible Hugoniot locus $\mathcal{H}$ in $AUBU$ (solid red) and inadmissible $\mathcal{H}$s for state $\boldsymbol{N}_q$ in other three regions (dashed red).

In summary, we can divide all waves into three classes depending on the location of the left state;

- No precipitate ($\boldsymbol{N}_l \in AUBU$): Every direction is an integral curve in this region. For any point in this region, admissible shocks are $\mathcal{S}_1$ with the right state in any other region. This class of shocks is represented by straight dashed red lines in

Figure 3.4a.

- One precipitate ($\boldsymbol{N}_l \in AUBS \cup ASBU$): There are two classes of integral curves in this region (Figure 3.3). In addition, admissible shocks have their right state in the region $ASBS$. Examples of fast shock curves are shown in Figure 3.4b.

- Two precipitates ($\boldsymbol{N}_l \in ASBS$): Any variation in this region is stationary, and it corresponds to a change in the amount of precipitates. Therefore, no shock develops in this region.

The above 3 classes of composition paths are the only possible routes in the hodograph plane. Therefore, the solution of the Riemann Problem is a combination of waves that are defined by these composition paths. The analytical solution to the problem is constructed using these waves.

3.2.3 *Clogging waves*

In this section, we study the dissolution shock waves that reduce the porosity upon propagation. The mobile ions in the unsaturated upstream flow react with the dissolved ions from the salt and can re-precipitate in the form of another salt. This phenomenon occurs due to the presence of the co-ion effect, i. e., the shared ion between the two salts. If the re-precipitating salt has less molar density, it reduces the porosity. The reduction may be up to 100% depending on the model parameters, i. e., ratio of molar densities and equilibrium constants and the initial conditions. We refer to these type of shock waves as clogging waves and find their explicit relationship with model parameters in this section. Recall from the Section 3.2.2.1 and Figure 3.4, that $\mathcal{H}_2$ for a point $\boldsymbol{N}_l = \begin{pmatrix} N_A^l \\ N_B^l \end{pmatrix} \in ASBU$ is two parts. The first part coincides with $\mathcal{I}_2(\boldsymbol{N}_l)$ inside $ASBU$ and the second part in $ASBS$ is the straight line

$$N_B = \frac{\hat{n}_B - n^l_A}{\hat{n}_A - n^l_B}(N_A - N^l_A) + N^l_B. \tag{3.15}$$

Therefore, the Hugoniot locus $\mathcal{H}$ for another point $\boldsymbol{N}_l'$, that is in $ASBU$ and on $\mathcal{I}_2(\boldsymbol{N}_l)$, is different only on the second part. The second part of $\mathcal{H}(\boldsymbol{N}_l')$, i. e., the staright line has a different slope. In fact, it can be shown that

$$\left(\frac{\partial}{\partial N_B}\right)_{\phi_A} \left(\frac{\hat{n}_B - n_B}{\hat{n}_A - n_A}\right) < 0 \tag{3.16}$$

in $ASBU$. Therefore, $\mathcal{H}_2$ for a point with $N_B = n_B = 0$ has the maximum slope $\dfrac{\hat{n}_B}{\hat{n}_A - \tilde{n}_A}$ in $ASBS$. Analogous to this argument, the minimum slope converges to $\left(-1 - \dfrac{\tilde{n}_A^2}{\hat{n}_A^2}\right)$ for a point that approaches the boundary curve B^{AS} along $\mathcal{I}_2(\boldsymbol{N}_l)$

(in $ASBU$). To calculate the minimum slope, l'Hospital's rule for multivariate functions is used with $(n_A, n_B) \to (\hat{n}_A, \hat{n}_B)$ [93].

Next, we look at the contours of porosity in the region $ASBS$. The iso-contours for porosity in this region are straight lines parallel to the hypotenuse of the domain with slope $-\omega_B/\omega_A$. Hence, if the second part of the Hugoniot locus $\mathcal{H}$ has a slope more than the slope of iso-porosity lines, there is a decrease of porosity from the left state of a fast shock to the right state. Therefore, the necessary condition to avoid clogging is that the minimum slope of $\mathcal{H}_2$ should be less than that of iso-porous lines, i. e.

$$-1 - \frac{\tilde{n}_A^2}{\hat{n}_A^2} < -\frac{\omega_B}{\omega_A} \qquad \Rightarrow \qquad \frac{\omega_A}{\omega_B}\left(2 + \frac{1}{k_A/k_B}\right) > 1. \tag{3.17}$$

In other words, when a salt (B) with a much higher molar density is more soluble, the other salt (A) starts to precipitate due to the co-ion effect. However, since the precipitating salt has a lower molar density than the dissolving one, it will take more space and may eventually take the whole available pore space and clog the system.

Comparing the maximum slope of $\mathcal{H}_2$ with iso-porosity lines, we obtain the sufficient condition to avoid clogging,

$$\frac{\hat{n}_B}{\hat{n}_A - \tilde{n}_A} < -\frac{\omega_B}{\omega_A} \qquad \Rightarrow \qquad \frac{\omega_A/\omega_B}{\sqrt{k_A/k_B}\sqrt{k_A/k_B + 1} - k_A/k_B} > 1 \tag{3.18}$$

To illustrate this condition, we consider the system with $k_A = 0.5$, $k_B = 0.71$, $\omega_A = 1$, $\omega_B = 5$, $\phi_P = 0.4$, $\boldsymbol{N}_l = \binom{0.20}{0.15}$. Figure 3.6 shows the corresponding hodograph plane. Here, we have $-\omega_B/\omega_A = -5$, whereas the maximum and minimum slopes are -2.56 and -3.43, respectively. We follow $\mathcal{H}_2$ of a point as it approaches the boundary of the domain $\binom{N_A^{max}}{0}$ along two different trajectories $N_B = 0$ and B^{AS}. The resulting $\mathcal{H}$-curves are shown as dashed (for trajectory $N_B = 0$) and solid (for trajectory B^{AS}) red lines in Figure 3.6, which divide $ASBS$ into three sections. Points in the upper part (e. g., $\boldsymbol{N}_r = \binom{0.20}{0.80}$) cannot be the right state for any fast shock with the left state in $ASBU$. In the next section, we construct the solution to the Riemann Problem and explain why Equation (3.13) has no solution for this system with $\boldsymbol{N}_l = \binom{0.20}{0.15}$. Extensions of the two red lines as $\mathcal{I}_2$ in $AUBS$ divides the region $AUBS$ in three segments (Figure 3.6) and a similar argument applies here.

The presented wave analysis of Equation (3.14a) in this section allows us to provide an exact solution for the Riemann Problem Equation (3.14). We provide this exact solution in the next section.

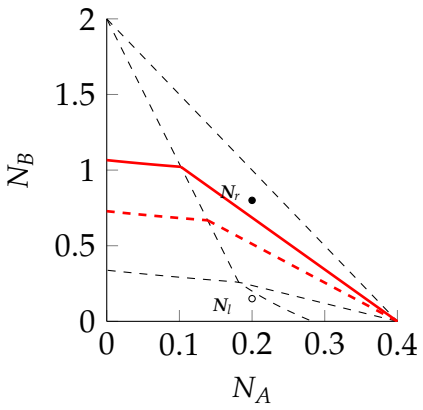

Figure 3.6: Clogging boundaries for $\mathcal{H}_2$ in $ASBS$ and $AUBS$. The system parameters are $k_A = 0.5\frac{\text{mol}^2}{\text{lit}^2}$, $k_B = 0.71\frac{\text{mol}^2}{\text{lit}^2}$, $\omega_A = 1\frac{\text{mol}}{\text{lit}}$, $\omega_B = 5\frac{\text{mol}}{\text{lit}}$ and $\phi_P = 0.4$.

3.3 SOLUTIONS OF THE RIEMANN PROBLEM

In this section, we study the evolution of the discontinuity of the Riemann Problem (Equation (3.14)). There are 2^4 possible cases combining left and right states of the discontinuity from any of the four regions I to IV. Table 3.1 shows all of these cases and the corresponding locations of the left and right states. In this section, the 16 cases are considered, and the unique solution is provided for each case. The solution to cases 1-10 is straightforward, and we only briefly discuss them. Cases 10 to 16 are more involved and require a more extensive discussion. The value of the parameters, unless stated otherwise, are $k_A = 1\frac{\text{mol}^2}{\text{lit}^2}$, $k_B = 0.67\frac{\text{mol}^2}{\text{lit}^2}$, $\omega_A = 3\frac{\text{mol}}{\text{lit}}$, $\omega_B = 2\frac{\text{mol}}{\text{lit}}$, $\phi_P = 0.4$. All solutions have been confirmed using finite-volumes methods. The comparison is not shown here for the sake of brevity.

Case:	1	2	3	4	5	6	7	8
$AUBU$		N_l, N_r	N_r	N_r				
$ASBU$			N_l		N_r		N_l, N_r	
$AUBS$				N_l		N_r		N_l, N_r
$ASBS$	N_l, N_r				N_l	N_l		

Case:	9	10	11	12	13	14	15	16
$AUBU$	N_r	N_l	N_l	N_l				
$ASBU$			N_r		N_l		N_l	N_r
$AUBS$				N_r		N_l	N_r	N_l
$ASBS$	N_l	N_r			N_r	N_r		

Table 3.1: Possible cases for the initial states of Riemann Problem (Equation (3.14))

3.3.1 *Case 1 ($ASBS \rightarrow ASBS$)*

When the left and right states are located in $ASBS$, then a saturated fluid is displaced by another saturated fluid. Hence, both eigenvalues are zero and the solution is a stationary wave.

3.3.2 *Case 2 ($AUBU \rightarrow AUBU$)*

When both left and right states are located in $AUBU$, an unsaturated fluid is displaced by another unsaturated one. Both eigenvalues are identical ($1/\phi_P$), and the case corresponds to two tracer transport problems with the same velocity ($1/\phi_P$).

3.3.3 *Cases 3 and 4 ($ASBU \rightarrow AUBU$ and $AUBS \rightarrow AUBU$)*

Case 3 describes the displacement of an unsaturated fluid by a saturated fluid emanating from a region containing precipitate of A. Figure 3.7 illustrates an example. Figure 3.7a shows that the intermediate point $\boldsymbol{N}_i$ is found at the intersection of $\mathcal{I}_1(\boldsymbol{N}_l)$ with the boundary A^{BU}. $\boldsymbol{N}_i$ lies on the boundary A^{BU} because along the integral curve and across A^{BU} the eigenvalue has a discontinuity. The second wave $\boldsymbol{N}_i \xrightarrow{\mathcal{C}_2} \boldsymbol{N}_r$ is analogous to case 2 and propagates with velocity $1/\phi_P$. Figure 3.7b illustrates these waves in the N-v plane (the profile of $\boldsymbol{N}$ after dimensionless time $t = 1$). Figure 3.7c illustrates the porosity profile for the solution. It shows the amount of precipitate ϕ_A (blue), the sum $\phi_A + \phi_B$ (dashed red) and ϕ_P (yellow), such that the area between ϕ_P and $\phi_A + \phi_B$ represents the void space.

3.3.4 *Case 5 and 6 ($ASBS \rightarrow ASBU$ and $ASBS \rightarrow AUBS$)*

Case 5 models a situation where fluid flows from a region containing precipitates of both A and B into a region containing only precipitates of A. The solution is $\boldsymbol{N}_l \xrightarrow{\mathcal{C}_1} \boldsymbol{N}_i \xrightarrow{\mathcal{C}_2} \boldsymbol{N}_r$ with $\boldsymbol{N}_i$ being on the intersection of the boundary line A^{BS} and $\mathcal{I}_2(\boldsymbol{N}_r)$. The fast eigenvalue is $\lambda_2 = 0$ in $ASBS$. In addition, it has a discontinuity that jumps to a nonzero value across the boundary line A^{BS}. Hence, $\boldsymbol{N}_i$ lies on the boundary line A^{BS}. The first wave is stationary in $ASBS$ and does not follow any path.

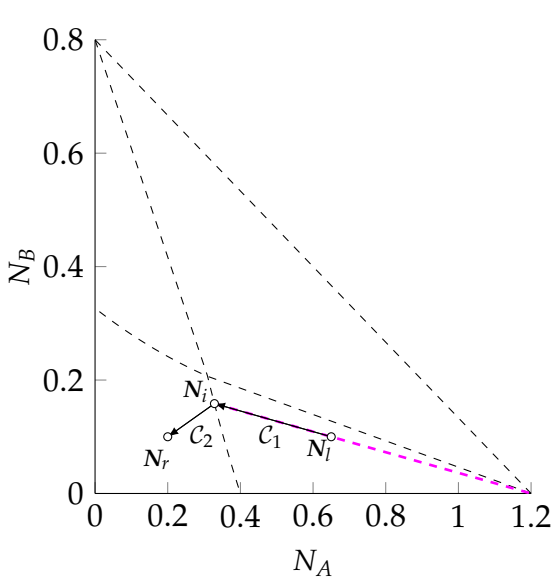

(a) solution on hodograph plane

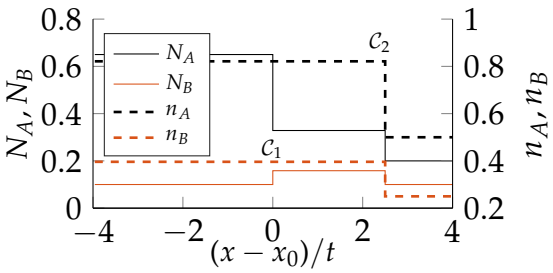

(b) concentrations profile

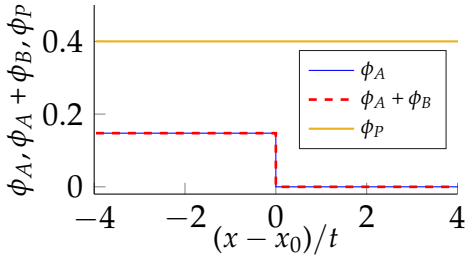

(c) precipitates profile

Figure 3.7: Example solution for case 3 with $\boldsymbol{N}_l = \binom{0.65}{0.10}\frac{\text{mol}}{\text{lit}}$ and $\boldsymbol{N}_r = \binom{0.2}{0.1}\frac{\text{mol}}{\text{lit}}$; (a) on the hodograph plane, (b) profile of concentration of ions, (c) profile of volume fractions of the precipitates. In Figure (a) $\boldsymbol{N}_i$ is on the boundary of $ASBU$ and $AUBU$. The waves are shown by arrows and the slow integral curve by a dashed magenta line. In Fig. (b) the labels are for the profiles of N_A and N_B.

3.3.5 *Cases 7 ($ASBU \to ASBU$) and 8 ($AUBS \to AUBS$)*

Case 7 models fluid flow from a region containing precipitate A into a region containing precipitate A. Figure 3.8 illustrates an example for this case. The intermediate point $\boldsymbol{N}_i$ in Figure 3.8a is the intersection of $\mathcal{I}_1(\boldsymbol{N}_l)$ with $\mathcal{I}_2(\boldsymbol{N}_r)$. The solution is a stationary wave $\boldsymbol{N}_l \xrightarrow{\mathcal{C}_1} \boldsymbol{N}_i$ followed by a fast wave $\boldsymbol{N}_i \xrightarrow{\mathcal{C}_2} \boldsymbol{N}_r$. Figures 3.8b and 3.8c show the concentration and precipitate profiles, respectively. The amount of precipitates varies along the stationary wave $\mathcal{C}_1$ whereas the ion concentrations in the fluid (n_A and n_B) vary along wave $\mathcal{C}_2$.

3.3.6 *Case 9 ($ASBS \to AUBU$)*

Case 9 represents fluid flow from a region containing precipitates of both salts into a region without any precipitate. The wave through $\boldsymbol{N}_l$ is stationary because $\lambda_1(\boldsymbol{N}_l) = \lambda_2(\boldsymbol{N}_l) = 0$. The transport wave through $\boldsymbol{N}_r$ has velocity $1/\phi_P$. The two waves connect through point $\boldsymbol{N}_t$. A path in either of the regions $ASBU$ and $AUBS$ is not possible.

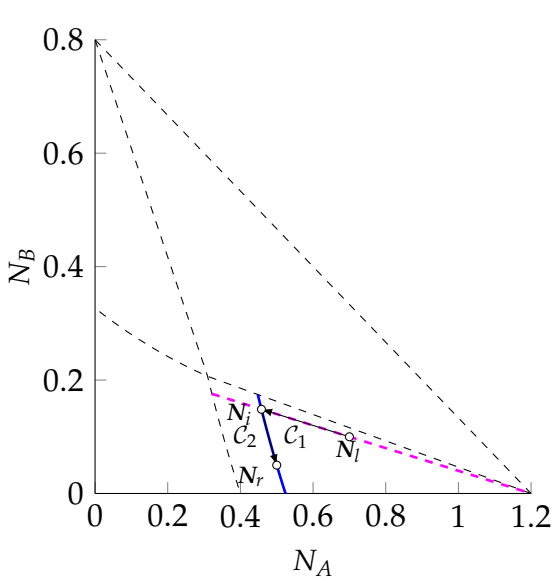

(a) solution on hodograph plane

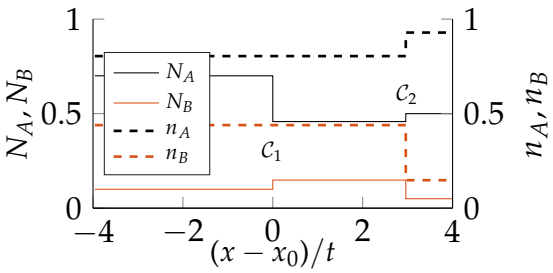

(b) concentrations profile

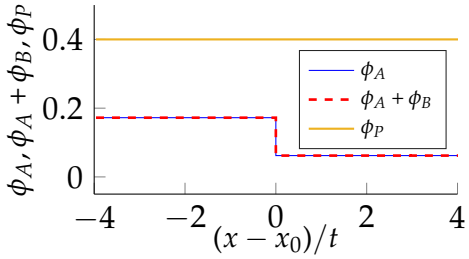

(c) precipitates profile

Figure 3.8: (a) Example solution for case 7 with on the hodograph plane with $\boldsymbol{N}_l = \binom{0.70}{0.10} \frac{\text{mol}}{\text{lit}}$ and $\boldsymbol{N}_r = \binom{0.5}{0.05} \frac{\text{mol}}{\text{lit}}$. $\boldsymbol{N}_i$ is on the intersection of $\mathcal{I}_1(\boldsymbol{N}_l)$ (magenta) and $\mathcal{I}_2(\boldsymbol{N}_r)$ (blue). (b) Profile of the solution on $\boldsymbol{N}$-v plane and (c) on ϕ-v plane.

3.3.7 *Case 10 ($AUBU \to ASBS$)*

Case 10 is the inverse of case 9, i. e., an unsaturated fluid from a region without any precipitate enters a region where precipitates of both A and B are present. An example for this case is presented in Figure 3.10. For this example, we assume the one dimensional domain is initially saturated with respect to both salts and it has 0.122 moles of precipitate A and 0.106 moles of precipitate B per a litre of the porous medium which is uniformly distributed in the medium. The imposed boundary condition is the injection of the unsaturated fluid at $x = 0$ with a concentration of $n_A = 0.625 \frac{\text{mol}}{\text{lit}}$ and $0.250 \frac{\text{mol}}{\text{lit}}$ for the fluid. In terms of the conserved variables, the boundary and the initial condition read as $\boldsymbol{N}_l = \binom{0.25}{0.10}$ and $\boldsymbol{N}_r = \binom{0.50}{0.3} \frac{\text{mol}}{\text{lit}}$. As discussed in the Section 3.2.2, the slow wave $\boldsymbol{N}_l \xrightarrow{\mathcal{W}_1} \boldsymbol{N}_i$ has to be a shock because a wave with the left state in $AUBU$ and the right state in any other region is a shock wave. The fast wave $\boldsymbol{N}_i \xrightarrow{\mathcal{W}_2} \boldsymbol{N}_r$ has to be a shock as well because a wave with the right state in $ASBS$ and the left state in any other region is a shock wave. The intermediate point in solution $\boldsymbol{N}_l \xrightarrow{\mathcal{S}_1} \boldsymbol{N}_i \xrightarrow{\mathcal{S}_2} \boldsymbol{N}_r$ can be either in $ASBU$ or $AUBS$ ($\boldsymbol{N}_{iA}$ and $\boldsymbol{N}_{iB}$ in Figure 3.10), i. e., either of the salts could dissolve faster.

The sequence of dissolution depends on the solubility constants and the relative amount of precipitates and concentration of ions in the fluid for both left and right states. These criteria can be boiled down to a simple condition: If $\boldsymbol{N}_l$ lies be-

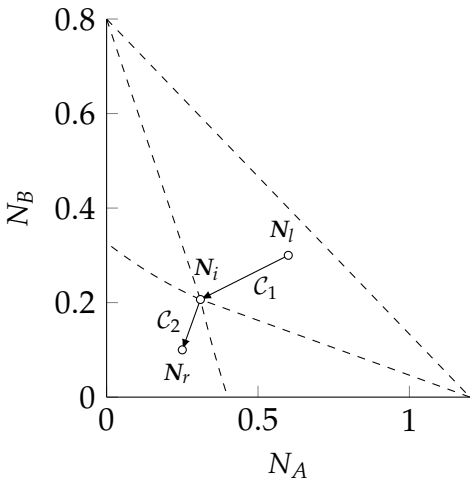

Figure 3.9: Solution for case 9 on the hodograph plane with the upstream fluid saturated with both fluids ($\boldsymbol{N}_l = \binom{0.60}{0.30} \frac{\text{mol}}{\text{lit}}$) and the downstream fluid unsaturated ($\boldsymbol{N}_r = \binom{0.25}{0.1} \frac{\text{mol}}{\text{lit}}$). Note that directions of the integral curves are abitrary in both regions $AUBU$ and $ASBS$.

low the extension of the line defined by $\boldsymbol{N}_r$ and $\boldsymbol{N}_t$, $\boldsymbol{N}_i$ is in $ASBU$. Otherwise, it is in $AUBS$. The line which connects $\boldsymbol{N}_r$ and $\boldsymbol{N}_t$ is in fact $\mathcal{H}(\boldsymbol{N}_r)$. Therefore, if $\boldsymbol{N}_l$ lies exactly on this line, the solution is a single shock that can be classified both 1-shock or 2-shock. In other words, the two shocks merge. The proofs are given in Lemmas 1 and 2 and Theorem 3 in the appendix. In summary, the solution is not stable if a slower shock is in front of a faster shock. The structure of the solution, i. e., the location of $\boldsymbol{N}_i$ changes so that this stability condition is satisfied because the speed of shocks depends on the location of all three points $\boldsymbol{N}_l$, $\boldsymbol{N}_i$ and $\boldsymbol{N}_r$. We refer to the line connecting $\boldsymbol{N}_r$ and $\boldsymbol{N}_t$ as the bifurcation line because the solution on the hodograph plane is discontinuous with respect to the location of the initial states relative to this line. However, the profile of the solution remains continuous with respect to the initial condition, because the velocities of the fronts are continuous functions of the composition (c.f. Appendix A.1). In order to find $\boldsymbol{N}_{iA}$ (or $\boldsymbol{N}_{iB}$) in the hodograph plane, the intersection of $\mathcal{H}(\boldsymbol{N}_l)$ with $\mathcal{H}(\boldsymbol{N}_r)$, is evaluated although the latter is not physically admissible. Generally, for any two points $\boldsymbol{N}_p$ and $\boldsymbol{N}_q$ if $\boldsymbol{N}_p \in \mathcal{H}(\boldsymbol{N}_q)$ then $\boldsymbol{N}_q \in \mathcal{H}(\boldsymbol{N}_p)$ [33]. Therefore, $\boldsymbol{N}_{iA}$ is the intersection $\mathcal{H}(\boldsymbol{N}_l)$ with $\mathcal{H}(\boldsymbol{N}_r)$ since $\boldsymbol{N}_{iA}$ belongs to $\mathcal{H}(\boldsymbol{N}_l)$ and $\boldsymbol{N}_r$ belongs to $\mathcal{H}(\boldsymbol{N}_{iA})$.

Figure 3.11a shows the concentration profiles of five Riemann Problemswith identical $\boldsymbol{N}_r$ and a $\boldsymbol{N}_l$ with slightly differing N_A. The solution for each case in the hodograph (Figure 3.11b) has a completely different structure. Thus, the intermediate states are different. The velocity of the two fronts is slightly altered as a result of small changes of $\boldsymbol{N}_l$.

Next, we consider a problem with the parameters and the initial condition as stated in the Section 3.2.3. The values for the parameters are set to k_A =

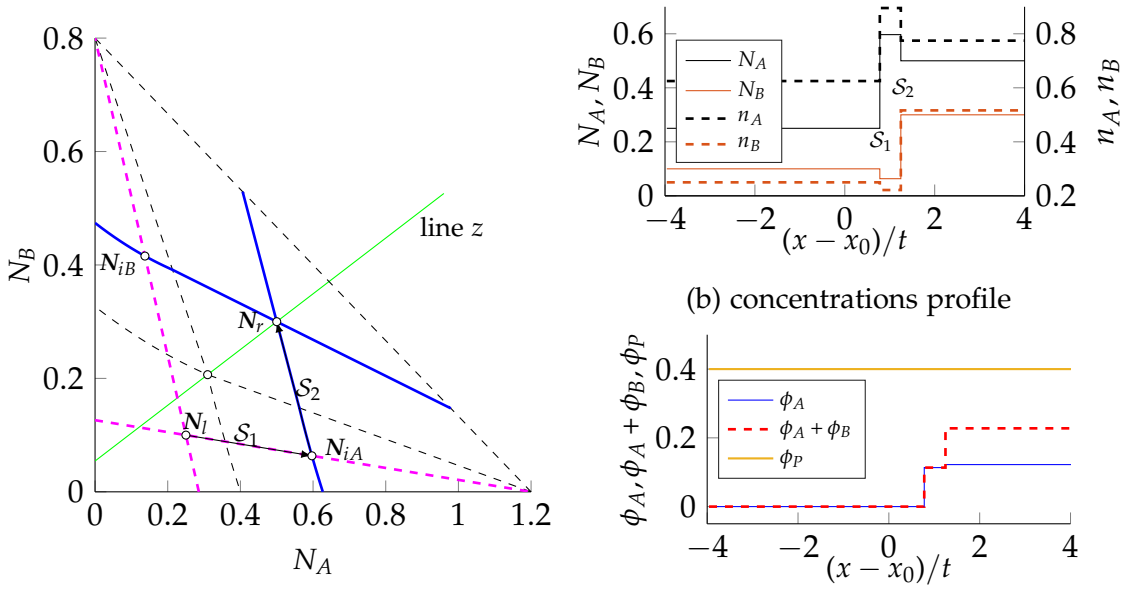

(a) solution on hodograph plane

(b) concentrations profile

(c) precipitates profile

Figure 3.10: (a) Construction of the solution for case 10 on the hodograph plane. Magenta lines show $\mathcal{H}_1(\boldsymbol{N}_l)$ and blue curves show $\mathcal{H}_2(\boldsymbol{N}_{iA})$ and $\mathcal{H}_2(\boldsymbol{N}_{iB})$ passing through $\boldsymbol{N}_r$. The state $\boldsymbol{N}_l$ is below the bifurcation line z and $\boldsymbol{N}_{iA}$ is the intermediate state. (b) Profile of the solution on the $\boldsymbol{N}$-v plane and (c) on the ϕ-v plane. The initial overall concentration for the domain is $\boldsymbol{N}_r = \binom{0.50}{0.3} \frac{\text{mol}}{\text{lit}}$ and the injected fluid overall concentration is $\boldsymbol{N}_l = \binom{0.25}{0.10} \frac{\text{mol}}{\text{lit}}$

$0.5\frac{\text{mol}^2}{\text{lit}^2}$, $k_B = 0.71\frac{\text{mol}^2}{\text{lit}^2}$, $\omega_A = 1\frac{\text{mol}}{\text{lit}}$, $\omega_B = 5\frac{\text{mol}}{\text{lit}}$. We consider the domain is initially filled with a fluid that is saturated with respect to both salts. The medium also contains 0.156 moles of precipitate A and 0.147 moles of precipitate B per a litre of the porous medium that is uniformly distributed across the domain. The boundary condition is the injection of the unsaturated fluid has concentration $n_A = 0.5\frac{\text{mol}}{\text{lit}}$ and $n_B = 0.375\frac{\text{mol}}{\text{lit}}$. In terms of the initial condition for the corresponding Riemann Problem, this would read as $\boldsymbol{N}_l = \binom{0.20}{0.15} \frac{\text{mol}}{\text{lit}}$ and $\boldsymbol{N}_r = \binom{0.2}{0.8} \frac{\text{mol}}{\text{lit}}$. Here, point $\boldsymbol{N}_i$ should be in $ASBU$ because $\boldsymbol{N}_l$ lies on the right side of the bifurcation line z. However, we discussed in the Section 3.2.3 that $\boldsymbol{N}_r$ cannot be the right state for a shock with the left state in $BSCU$. Therefore, this Riemann Problem has no solution. If, on the other hand, the right state $\boldsymbol{N}'_r = \binom{0.26}{0.40}$ as in Figure 3.12a, is in the middle section, the existence of a solution is determined by the location of $\boldsymbol{N}_l$. Figure 3.12 illustrates the solution for this example with $\boldsymbol{N}_l = \binom{0.20}{0.15}$. As depicted in Figure 3.12c, the void space in the transient region is lower than the initial void space in any other location. In fact, one can identify a prohibited region in $AUBU$ for which the solution has an unphysical intermediate state. This area is highlighted with yellow colour in Figure 3.10a and is bounded by two lines: The bifurcation line z (cf. Figure 3.10) and the extension of $\mathcal{I}_1$ of a set of limit points in $ASBU$. Physically speaking, completely freshwater cannot be used to dissolve both salts for such a system,

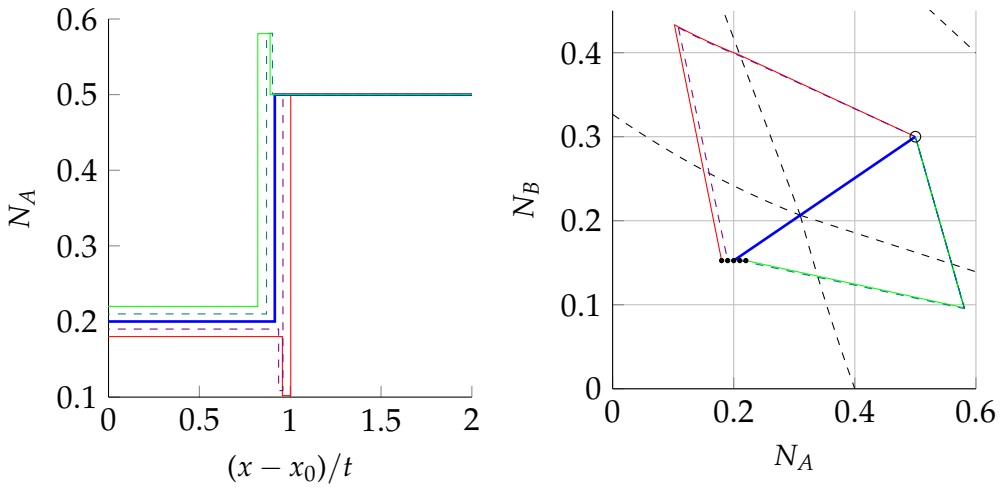

Figure 3.11: (a) Profile of the solution of five Riemann Problemswith $\boldsymbol{N}_r = (0.5, 0.3)^T$ and $\boldsymbol{N}_l = \left(N_A^l, 0.15\right)^T$ with slightly different values for N_A^l. (b) Structure of the solution on the hodograph plane. Note that the the structure of the solution is discontinuous with respect to the initial condition on hodograph plane. However, this is the case if we only look at the hodograph plane, because the velocities are continuous as shown in Figure (a).

because it leads to clogging, i. e., the porosity of the medium goes to zero (c.f. the Section 3.2.3). Instead, an unsaturated fluid that contains a small amount of B should be used.

3.3.8 *Cases 11 and 12 ($AUBU \rightarrow ASBU$ and $AUBU \rightarrow AUBS$)*

An example for case 11, when an unsaturated fluid dissolves precipitate A, is depicted in Figure 3.13. The direct solution is $\boldsymbol{N}_l \xrightarrow{\mathcal{S}_1} \boldsymbol{N}_i \xrightarrow{\mathcal{C}_2} \boldsymbol{N}_r$, where $\boldsymbol{N}_i$ is the intersection of $\mathcal{H}_1(\boldsymbol{N}_l)$ and $\mathcal{I}_2(\boldsymbol{N}_r)$ in $ASBU$. This wave structure is not possible if $\boldsymbol{N}_l$ belongs to region α in $AUBU$, because $\mathcal{H}_1(\boldsymbol{N}_l)$ and $\mathcal{I}_2(\boldsymbol{N}_r)$ cannot intersect in $ASBU$. In other words, the fast wave is not coherent. Figure 3.14 illustrates this case, with $\boldsymbol{N}_l \xrightarrow{\mathcal{S}_1} \boldsymbol{N}_{i1} \xrightarrow{\mathcal{S}_2} \boldsymbol{N}_{i2} \xrightarrow{\mathcal{C}_2} \boldsymbol{N}_r$. Here, the second wave is compound wave of $\mathcal{S}_2$ followed by $\mathcal{C}_2$. $\boldsymbol{N}_{i2}$ lies on the boundary B^{AS}, because of the discontinuity of the second eigenvalue across this line.

There are two points to be highlighted:

1. In the second case, the first intermediate point is in $AUBS$, with B precipitates. Even though on neither side of the Riemann Problem C precipitates are present, a transient region forms with B precipitates. The region of precipitate B is forming after the dissolution of A because the concentration of B in the upstream fluid is relatively high and the added common ion X from the dissolution of salt A leads to precipitation of salt B.

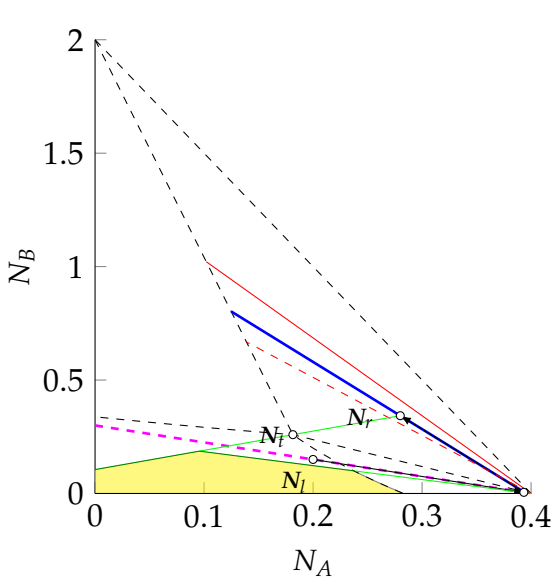

(a) solution on hodograph plane

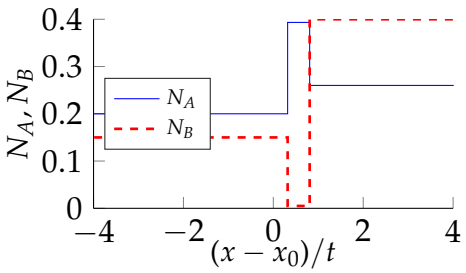

(b) concentrations profile

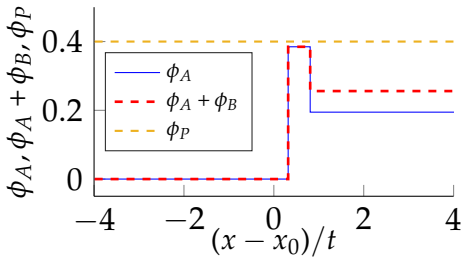

(c) precipitates profile

Figure 3.12: (a) Solution for case 10 when the shock wave $\mathcal{C}_2$ causes the more reactive and less dense salt B to precipitate. The structure is analogous to Figure 3.10. However, here the intermediate point is very close to the boundary of the domain. For the given $\boldsymbol{N}_r$ the problem has no solution if $\boldsymbol{N}_l$ lies in the yellow shaded region. (b) Profile of the concentrations. (c) Profile of the precipitates in the ϕ-v plane. The increase in A precipitate almost fills the available void space. The parameters are $k_A = 0.5\frac{\text{mol}^2}{\text{lit}^2}$, $k_B = 0.71\frac{\text{mol}^2}{\text{lit}^2}$, $\omega_A = 1\frac{\text{mol}}{\text{lit}}$, $\omega_B = 5\frac{\text{mol}}{\text{lit}}$, $\phi_P = 0.4$. The initial condition for the Riemann Problem are $\boldsymbol{N}_l = \binom{0.20}{0.15}$ and $\boldsymbol{N}_r = \binom{0.28}{0.34}\frac{\text{mol}}{\text{lit}}$

2. The solution shows the compound wave structure only if $\boldsymbol{N}_l$ lies in the region above the extension line. We prove in Theorem 4 that the compound wave structure is unstable if $\boldsymbol{N}_l$ does not belong to α and the first structure is possible.

3.3.9 *Case 13 (ASBU → ASBS) and 14 (AUBS → ASBS)*

Cases 13 and 14 model flow from a region with one precipitate into a region where both precipitates are present. Case 13 with $\boldsymbol{N}_l$ in *ASBU* and $\boldsymbol{N}_r$ in *ASBS* is illustrated in Figures 3.15 and 3.16. In these figures, the solubility constants are altered from $k_A = 1\frac{\text{mol}^2}{\text{lit}^2}$, $k_B = 0.67\frac{\text{mol}^2}{\text{lit}^2}$ to $k_A = 1.5\frac{\text{mol}^2}{\text{lit}^2}$, $k_B = 2\frac{\text{mol}^2}{\text{lit}^2}$ for illustrative purposes. The structure of the solution depends on whether or not $\boldsymbol{N}_r$ belongs to region β (the green shaded region). When $\boldsymbol{N}_r$ does not belong to region β, cf. Figure 3.15, $\boldsymbol{N}_i$ is the intersection of $\mathcal{I}_1(\boldsymbol{N}_l)$ with $\mathcal{H}(\boldsymbol{N}_r)$ in *ASBU* and therefore the solution is $\boldsymbol{N}_l \xrightarrow{\mathcal{C}_1} \boldsymbol{N}_i \xrightarrow{\mathcal{S}_2} \boldsymbol{N}_r$. However, if $\boldsymbol{N}_r$ lies in β, this structure is not possible, because no point on $\mathcal{I}_1(\boldsymbol{N}_l)$ can be connected to $\boldsymbol{N}_r$ via $\mathcal{H}_2(\boldsymbol{N}_r)$ and the solution has a different structure. In this case, the slow wave

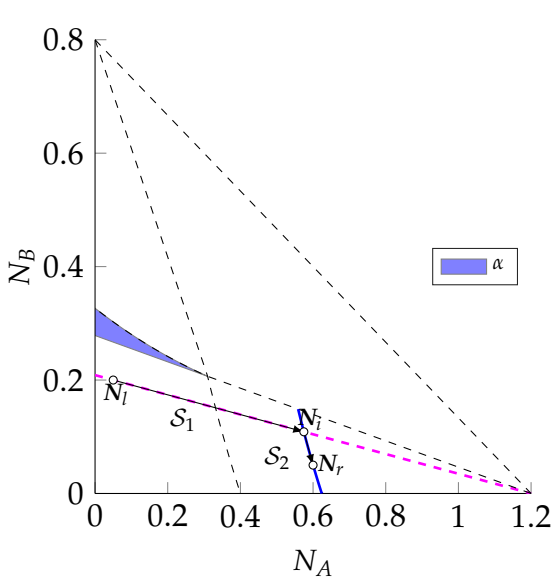

(a) solution on hodograph plane

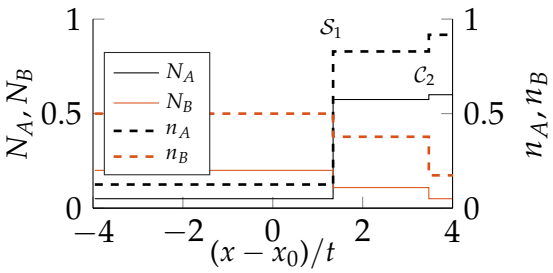

(b) concentrations profile

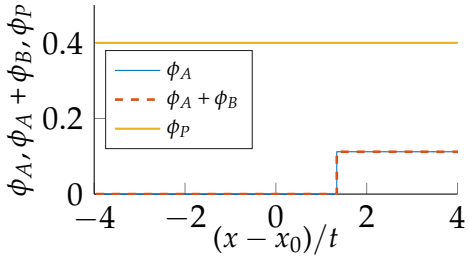

(c) precipitates profile

Figure 3.13: (a) Construction of the solution for case 11 on the hodograph plane when there is a direct path from $\boldsymbol{N}_l$ to $ASBU$. The magenta line shows $\mathcal{H}_1(\boldsymbol{N}_l)$ and the blue curve shows $\mathcal{H}(\boldsymbol{N}_r)$. (b) Solution of the same problem on the $\boldsymbol{N}$-v plane and (c) on the ϕ-v plane. The initial condition for the Riemann Problem is $\boldsymbol{N}_l = \left(\begin{smallmatrix} 0.05 \\ 0.20 \end{smallmatrix}\right)$ and $\boldsymbol{N}_r = \left(\begin{smallmatrix} 0.60 \\ 0.05 \end{smallmatrix}\right) \frac{\text{mol}}{\text{lit}}$

is not coherent. Figure 3.16 shows an example for this case. The first wave is compound $\boldsymbol{N}_l \xrightarrow{\mathcal{C}_1} \boldsymbol{N}_{i1} \xrightarrow{\mathcal{S}_1} \boldsymbol{N}_{i2}$. Its intermediate point $\boldsymbol{N}_{i1}$ lies on the boundary A^{BU}, where λ_1 is discontinuous. Its right state $\boldsymbol{N}_{i2}$ lies in $AUBS$, where the second wave $\mathcal{S}_2$ can follow to $\boldsymbol{N}_r$.

In the second case, a dissolution front initiates at $x = 0$. All the salts will eventually be dissolved by this wave because it is the slowest non-stationary wave. Using an argument similar to Theorem 4 of the appendix, it can be proved that this structure for the solution is only stable when $\boldsymbol{N}_r$ lies in β.

3.3.10 *Cases 15 ($ASBU \to AUBS$) and 16 ($AUBS \to ASBU$)*

Case 15 describes the flow of a fluid from a region containing only A precipitate into a region containing only B precipitate. The first wave is stationary $\mathcal{C}_1$, because $\lambda_1(\boldsymbol{N}_l) = 0$ and the last wave is $\mathcal{C}_2$. The solution has two possible structures depending on the curvature of A^{BU}, i. e., whether the two non-coherent regions α and β exist.

Figure 3.17 shows an example for the first case. Note that for illustrative purposes, we use the same parameter values as for Figure 3.16. The point $\boldsymbol{N}_{i1}$ is the intersection of A^{BU} with the integral curve $\mathcal{I}_1(\boldsymbol{N}_l)$ and $\boldsymbol{N}_{i2}$ is the intersection of $\mathcal{H}_1(\boldsymbol{N}_{i1})$ with $\mathcal{I}_2(\boldsymbol{N}_r)$. The solution for this case is $\boldsymbol{N}_l \xrightarrow{\mathcal{C}_1} \boldsymbol{N}_{i1} \xrightarrow{\mathcal{S}_1} \boldsymbol{N}_{i2} \xrightarrow{\mathcal{C}_2} \boldsymbol{N}_r$, i. e.,

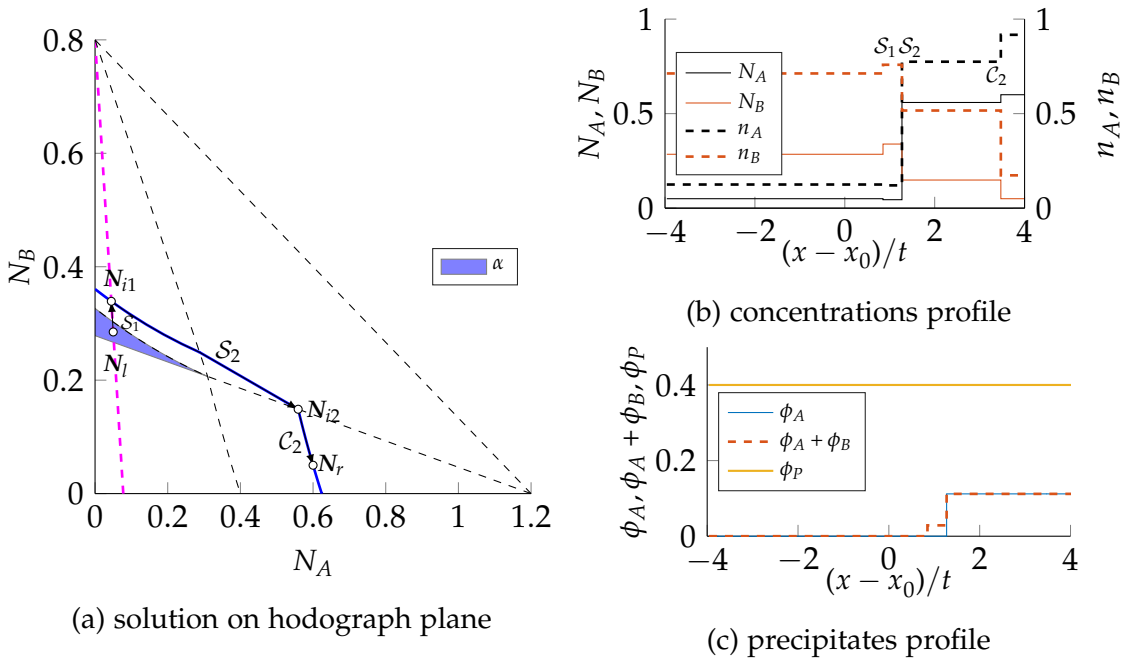

(a) solution on hodograph plane

(b) concentrations profile

(c) precipitates profile

Figure 3.14: (a) Construction of the solution for case 11 on the hodograph plane when there is not a direct path from $\boldsymbol{N}_l$ to $ASBU$, i. e., when $\boldsymbol{N}_l$ is in region α (shaded blue region). The magenta line shows $\mathcal{H}_1(\boldsymbol{N}_l)$ and the blue curves represent $\mathcal{H}_2(\boldsymbol{N}_{i1})$ and $\mathcal{I}_2(\boldsymbol{N}_r)$. $\boldsymbol{N}_{i2}$ is on the boundary and therefore belongs to both $\mathcal{H}_1(\boldsymbol{N}_{i1})$ and $\mathcal{I}_2(\boldsymbol{N}_r)$. (b) Solution of the same problem on $\boldsymbol{N}$-v plane and (c) on ϕ-v plane. The initial condition for the Riemann Problem is $\boldsymbol{N}_l = \begin{pmatrix} 0.050 \\ 0.285 \end{pmatrix}$ and $\boldsymbol{N}_r = \begin{pmatrix} 0.60 \\ 0.05 \end{pmatrix} \frac{\text{mol}}{\text{lit}}$

the first wave is a compound wave starting from a stationary wave and followed by a $\mathcal{S}_1$.

The above structure is unstable if the Hugoniot locus $\mathcal{H}$, of the intersection of the integral curve $\mathcal{I}_1(\boldsymbol{N}_l)$ with the separating curve A^{BU} does not have a branch in $AUBS$. Then, the fast wave is a compound wave composed of a shock $\mathcal{S}_2$ and a contact discontinuity $\mathcal{C}_2$. Figure 3.18 illustrates an example for this case. Point $\boldsymbol{N}_{i2}$ is the intersection of A^{BS} with $\mathcal{I}_2(\boldsymbol{N}_r)$ and hence $\boldsymbol{N}_{i1}$ is inside $ASBU$ and is the intersection of $\mathcal{H}_1(\boldsymbol{N}_l)$ with $\mathcal{H}(\boldsymbol{N}_{i2})$. The solution follows $\boldsymbol{N}_l \xrightarrow{\mathcal{C}_1} \boldsymbol{N}_{i1} \xrightarrow{\mathcal{S}_2} \boldsymbol{N}_{i2} \xrightarrow{\mathcal{C}_2} \boldsymbol{N}_r$. The parameter values for Figure 3.18 are $k_A = 0.33 \frac{\text{mol}^2}{\text{lit}^2}$, $k_B = 1 \frac{\text{mol}^2}{\text{lit}^2}$, $\omega_A = 2 \frac{\text{mol}}{\text{lit}}$, $\omega_B = 3 \frac{\text{mol}}{\text{lit}}$. The two cases differ with respect to the existence of precipitates in the intermediate states.

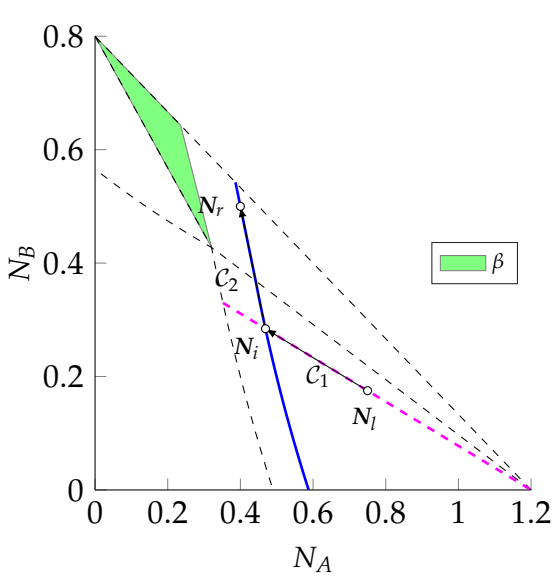

(a) solution on hodograph plane

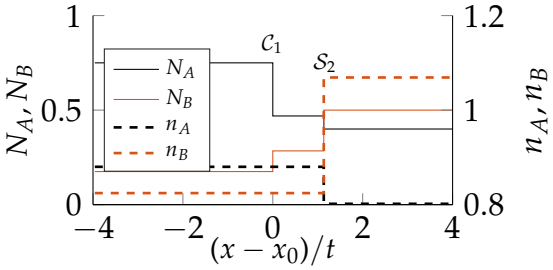

(b) concentrations profile

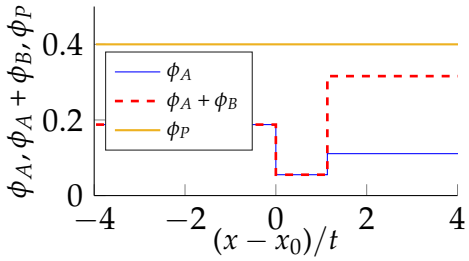

(c) precipitates profile

Figure 3.15: (a) Construction of the solution for case 13 on the hodograph plane when $\boldsymbol{N}_r$ can be the right state of a shock with the left state in $ASBU$. The magenta line depicts $\mathcal{I}_1(\boldsymbol{N}_l)$ and the blue curve show $\mathcal{H}(\boldsymbol{N}_r)$ and $\boldsymbol{N}_i$ marks the intersection of them. (b) Solution of the same problem on the $\boldsymbol{N}$-v plane and (c) on the ϕ-v plane. The system parameters are $k_A = 1.5\frac{\text{mol}^2}{\text{lit}^2}, k_B = 2\frac{\text{mol}^2}{\text{lit}^2}, \omega_A = 1\frac{\text{mol}}{\text{lit}}, \omega_B = 0.4\frac{\text{mol}}{\text{lit}}$ and $\phi_P = 0.4$. The initial condition for the Riemann Problem is $\boldsymbol{N}_l = \binom{0.75}{0.18}$ and $\boldsymbol{N}_r = \binom{0.4}{0.5}\frac{\text{mol}}{\text{lit}}$

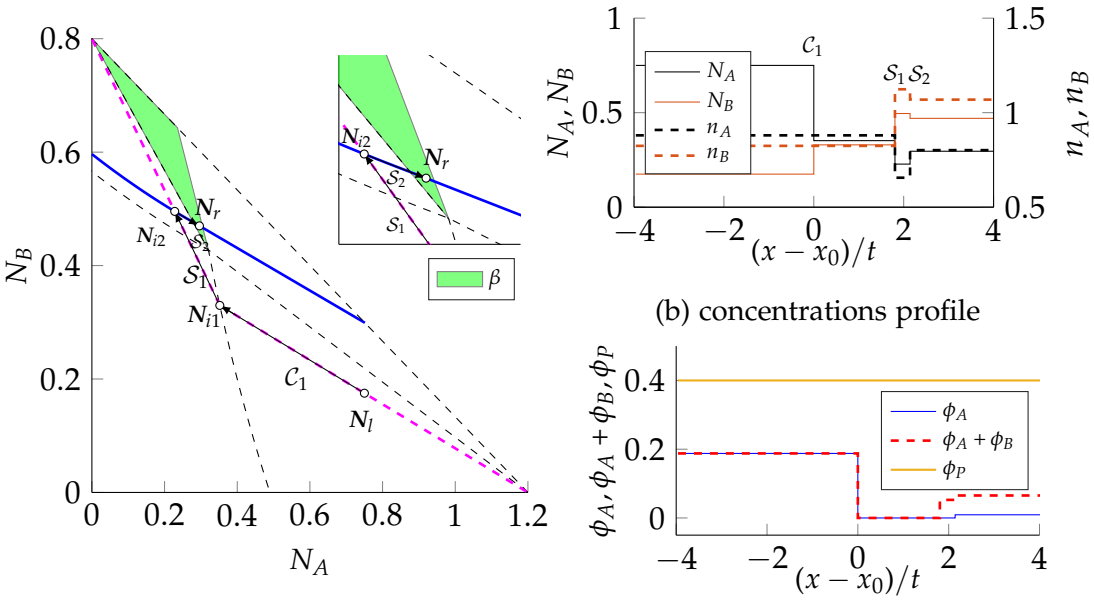

(a) solution on hodograph plane

(b) concentrations profile

(c) precipitates profile

Figure 3.16: (a) Construction of the solution for case 13 on the hodograph plane when $\boldsymbol{N}_r$ can not be the right state of a shock with the left state in $ASAU$, i. e., when $\boldsymbol{N}_r$ belongs to the green shaded region β. The magenta lines show $\mathcal{I}_1(\boldsymbol{N}_l)$ and $\mathcal{H}_1(\boldsymbol{N}_{i1})$. The state $\boldsymbol{N}_{i2}$ is the intersection of $\mathcal{H}_2(\boldsymbol{N}_r)$ (blue curve) with $\mathcal{H}_1(\boldsymbol{N}_{i1})$. The two first waves $\mathcal{C}_1$, $\mathcal{S}_1$ are the two parts of the slow compound wave. (b) Solution of the same problem on the $\boldsymbol{N}$-v plane and (c) on the ϕ-v plane. The parameter values are $k_A = 1.5\frac{\text{mol}^2}{\text{lit}^2}, k_B = 2\frac{\text{mol}^2}{\text{lit}^2}, \omega_A = 1\frac{\text{mol}}{\text{lit}}, \omega_B = 0.4\frac{\text{mol}}{\text{lit}}$ and $\phi_P = 0.4$. The initial condition for the Riemann Problem is $\boldsymbol{N}_l = \binom{0.75}{0.18}$ and $\boldsymbol{N}_r = \binom{0.296}{0.470}\frac{\text{mol}}{\text{lit}}$

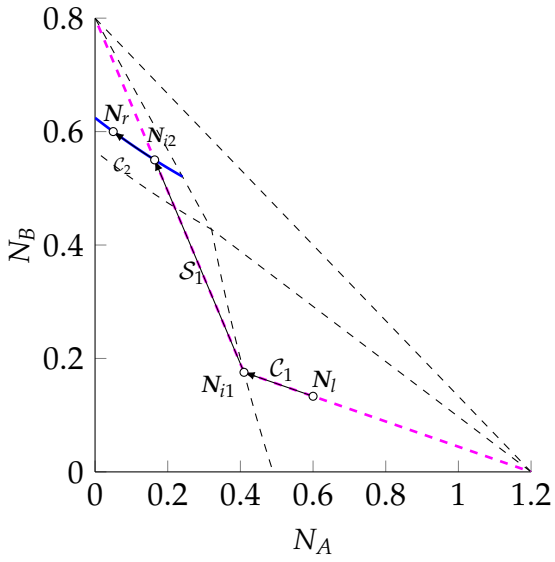

(a) solution on hodograph plane

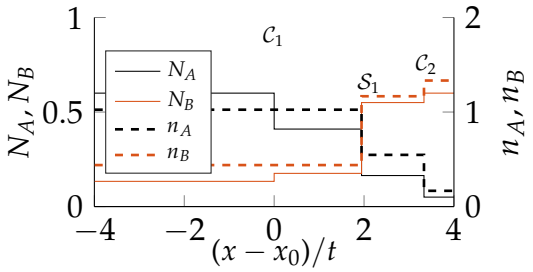

(b) concentrations profile

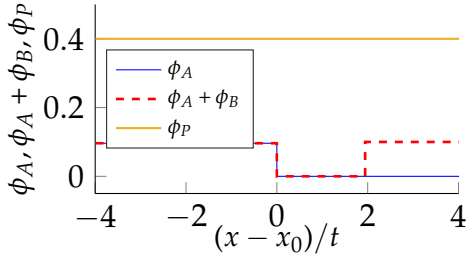

(c) precipitates profile

Figure 3.17: (a) Construction of the solution for case 15 on the hodograph plane when the intermediate points are connected by a slow shock. The magenta lines shows $\mathcal{H}_1(\boldsymbol{N}_l)$ and $\mathcal{H}_1(\boldsymbol{N}_{i1})$. The state $\boldsymbol{N}_{i2}$ is the intersection of $\mathcal{I}_2(\boldsymbol{N}_r)$ (blue) with $\mathcal{H}_1(\boldsymbol{N}_{i1})$. The waves $\mathcal{C}_1$ and $\mathcal{S}_1$ are the two parts of the slow compound wave. (b) Solution of the same problem on the $\boldsymbol{N}$-v plane and (c) on the ϕ-v plane. The parameter values are $k_A = 1.5\frac{\text{mol}^2}{\text{lit}^2}, k_B = 2\frac{\text{mol}^2}{\text{lit}^2}, \omega_A = 1\frac{\text{mol}}{\text{lit}}, \omega_B = 0.4\frac{\text{mol}}{\text{lit}}$ and $\phi_P = 0.4$. The initial condition for the Riemann Problem is $\boldsymbol{N}_l = \binom{0.60}{0.13}$ and $\boldsymbol{N}_r = \binom{0.05}{0.60}\frac{\text{mol}}{\text{lit}}$

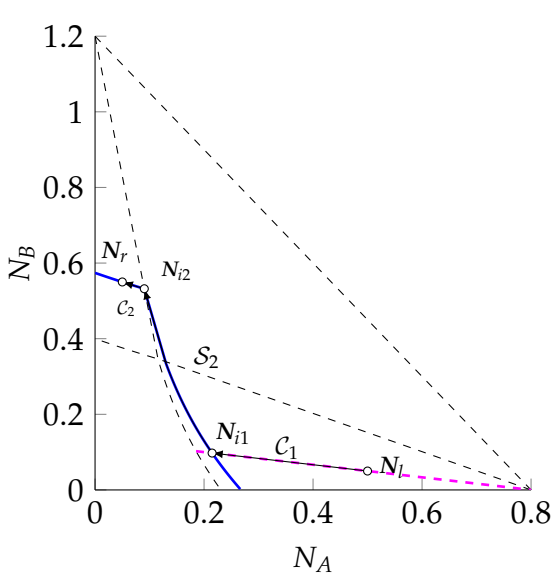

(a) solution on hodograph plane

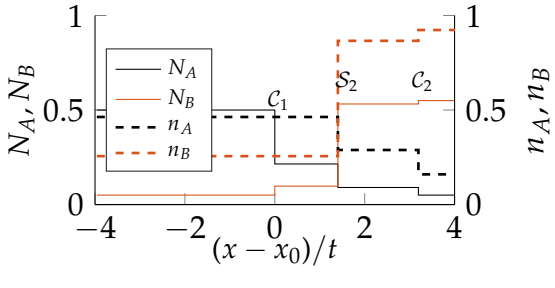

(b) concentrations profile

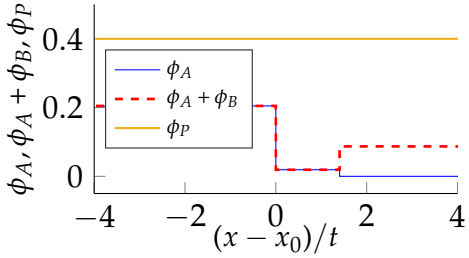

(c) precipitates profile

Figure 3.18: (a) Construction of the solution for case 15 on the hodograph plane when the intermediate points are connected by a fast shock. Blue curves show $\mathcal{I}_2(\boldsymbol{N}_r)$ and $\mathcal{H}_2(\boldsymbol{N}_{i2})$. The state $\boldsymbol{N}_{i1}$ is the intersection of $\mathcal{I}_1(\boldsymbol{N}_l)$ (magenta) with $\mathcal{H}_2(\boldsymbol{N}_{i2})$. The waves $\mathcal{S}_2$ and $\mathcal{C}_2$ are the two parts of the fast compound wave. (b) Solution of the same problem on the $\boldsymbol{N}$-v plane and (c) on the ϕ-v plane. The parameter values are $k_A = 0.33\frac{\text{mol}^2}{\text{lit}^2}, k_B = 1\frac{\text{mol}^2}{\text{lit}^2}, \omega_A = 2\frac{\text{mol}}{\text{lit}}, \omega_B = 3\frac{\text{mol}}{\text{lit}}$ and $\phi_P = 0.4$. The initial condition for the Riemann Problem is $\boldsymbol{N}_l = \begin{pmatrix} 0.50 \\ 0.05 \end{pmatrix}$ and $\boldsymbol{N}_r = \begin{pmatrix} 0.05 \\ 0.55 \end{pmatrix} \frac{\text{mol}}{\text{lit}}$

In this section, we summarise and discuss the key findings of the Section 3.3 from a chemical and physical perspective without the technical aspects of the construction of the solution.

In case 10 of the Section 3.3, we discussed two different solutions that occur when an unsaturated fluid enters a region with both precipitates (c.f. Figure 3.10a). The structure of the solution and therefore, the sequence of the dissolution of salts depends on the location of $\boldsymbol{N}_l$ in the hodograph plane relative to the bifurcation line z. If an application prioritises the dissolution of one specific salt where both salts are present, the injection fluid composition can be designed with the help of bifurcation line z.

The priority is more important when the molar density difference between the two salts becomes more significant. Dissolution of a denser salt (for example BX) releases both ions in the fluid. The common ion X is now available to re-precipitate with the other mobile ion (A) and produce a less dense salt AX. Hence, the porosity of the medium reduces. If the relevant conditions hold (c.f. Equations (3.17) and (3.18)) the reduction is 100%, i. e., the system clogs itself. Figure 3.19 shows these two conditions in the space of ω_A/ω_B vs k_A/k_B as well as values for four pairs of minerals ($BaSO_4$, $CaSO_4$), (NaCl, KCl), ($CaCO_3$, $CaSO_4$), (LiF, LiCl). The pair (LiF, LiCl), does not satisfy either of conditions and therefore clogging is possible. Another example why the sequence of dissolution may be important is to avoid such clogging by dissolving the less dense salt first.

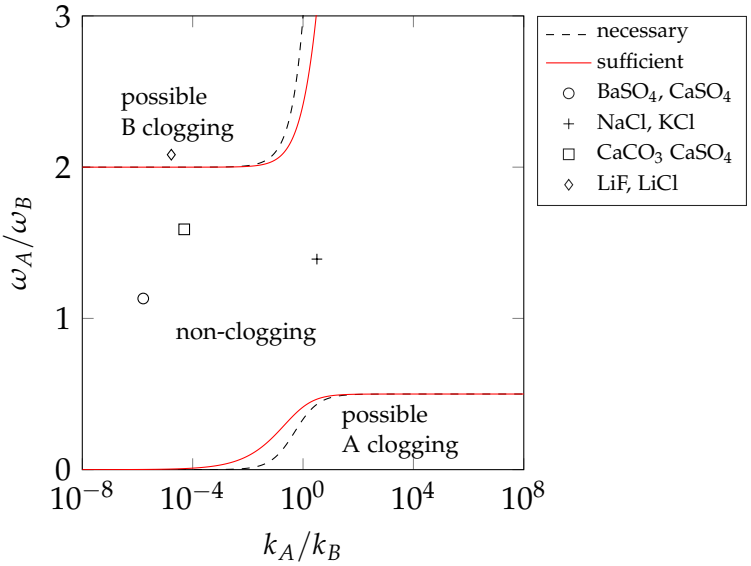

Figure 3.19: Necessary and sufficient condition curves to avoid clogging in the space of molar density ratio vs equilibrium constant ratio. Four different pairs of two minerals are shown as examples. B, C and S for the systems in the legend are in the form B-S, C-S respectively with S being the common ion.

Case 11 also shows a bifurcation in the behaviour on whether region α is present or not. The solution structure can have an intermediate precipitate of B depending on the composition of $\boldsymbol{N}_l$ (c.f. Figures 3.13a and 3.14a). If the unsaturated injection fluid is relatively rich in B such that its corresponding point in hodograph plane lies in the non-coherent region α, an intermediate state with salt B appears. The formation of salt B effectively reduces the required pore volume of injection fluid if the main objective is only to dissolve salt A but does not harm to precipitate salt B. That is, in dissolving salt A we allow salt B to precipitate and hence the slowest wave required to reach the producer is a fast shock.

When the region β exists in the hodograph plane and contains the point corresponding to the initial fluid $\boldsymbol{N}_r$, an intermediate point in the unsaturated zone appears. In other words, regardless of the amount of A in the injection fluid, all the salts are dissolved (c.f. Figure 3.16a). However, if point $\boldsymbol{N}_r$ is outside of region β, the injection of a fluid with a high concentration of A does not completely dissolve salt A. Therefore, the transient region has precipitate of A.

Finally, it is worth comparing the solution to the one obtained by Helfferich. In doing so, we observe not only the appearance of new intermediate states, but also change of speed of the shocks. The intermediate states appear mainly because of the changes in the structure of first Hugoniot Loci (from horizontal/vertical lines to inclined lines). In Figure 3.20, we have illustrated both solution for case 10 with initial condition $\boldsymbol{N}_r = \binom{1.00}{1.25}$ and boundary condition $\boldsymbol{N}_l = \binom{0.5}{0.5}$. Needless to say, other features of the solution, i. e., self-clogging characteristics and some of the bifurcations, would not appear if it is assumed that the porosity contribution to changes in the volume is negligible.

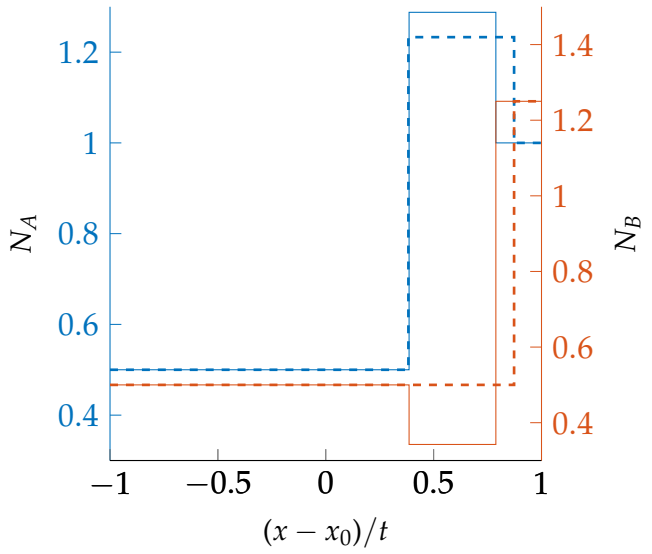

Figure 3.20: Comparison of analytical solution from [1] (thick dashed) and the one presented in this chapter (solid) for $\boldsymbol{N}_l = (0.5, 0.5)^T$ and $\boldsymbol{N}_r = (1.00, 1.25)^T$ (case 10). The overall concentration of N_A and N_B are shown by blue and red color, respectively.

3.5 CONCLUSIONS

This chapter presented analytical solutions for reactive flow containing two precipitation and dissolution reactions with a shared ion in an ideal chemical solution. The presentation extends the theory of precipitation/dissolution waves developed by Helfferich [1] to systems where changes of porosity are significant. The analysis of the structure of the solution provides a tool for identifying clogging and non-clogging situations. The mathematical solution is constructed using the method of characteristics from the theory of hyperbolic partial differential equations. The behaviour of the system is different depending on the presence of the two precipitates.

1. In the absence of precipitates, or when both precipitates exist, the system is non-strictly hyperbolic with identical eigenvalues.

2. When only one of the precipitates is present, eigenvalues are constant along integral curves, and the system is linearly degenerate.

3. Rarefaction waves do not form, and the solution is only composed of shocks and contact discontinuities.

4. Every shock wave completely dissolves at least one salt. A simple criterion is provided for the sequence of the dissolution of the salts.

5. Precipitation and partial dissolution of salts occur along stationary waves. Transport waves are not retarded and therefore travel with the fluid velocity.

6. In the solution to the general Riemann Problem, compound waves may form (shock + contact or contact + shock). The compound waves form because the Jacobian matrix is not globally differentiable. The formation of compound waves depends on the parameters of the system and the initial composition. There are a total of 7 bifurcations with respect to the initial condition and system parameters for the general Riemann Problem.

7. Compound waves introduce new intermediate states. They can have a different amount of precipitates compared to the initial condition. An intermediate state with no precipitate appears when a region rich in two salts is flushed with a fluid that is saturated with only one salt (c.f. Figure 3.16). Conversely, intermediate states can form which have nearly no space for the fluid to flow (c.f. Figure 3.12).

4

STREAMLINE SIMULATION FOR FLOW WITH PRECIPITATION AND DISSOLUTION

In this chapter, we present a multi-dimensional simulation method for reactive flow in porous media of two salts that share an ion, i. e., Equation (3.4) on page 20. The method consists of a front-tracking solver that uses the Riemann solutions of the underlying set of hyperbolic PDEs. In addition to the discontinuities stemming from the nonlinearities of the flux function, as discussed in Chapter 3, the flux function for the corresponding advection reaction equation also admits discontinuities for a heterogeneous medium. Here, we present the analytical solution for the governing nonlinear hyperbolic system with a discontinuous flux function. We use mass balance across the interface and the non-decreasing sequence of the velocity of waves to seek the unique solution for this problem. Furthermore, a model is provided for mixing of streamlines at the well to estimate the amount of precipitate. The simulation method is applied to model dissolution through injection of an unsaturated fluid. It is shown that the first dissolution shock, which causes induced precipitation due to the co-ion effect, results in the accumulation of precipitate at the well.

4.1 PHYSICAL AND CHEMICAL MODEL

The problem we address here is the injection of brine into a reservoir that already contains another brine with a different composition. The difference in compositions causes the two brines to react as the injected brine pushes the initial one. The flow field is obtained independent of the chemical reactions and transport of the materials. We assume there is no difference in the density and the viscosity of the injected and the produced brine. Hence, Darcy's law in the absence of gravity reads

$$v = -\frac{\boldsymbol{K}}{\mu}\nabla P, \tag{4.1}$$

where $\boldsymbol{K}$ is the permeability tensor and μ is the viscosity of the solution. Mass conservation for an incompressible fluid in an incompressible rock requires

$$\nabla \cdot \boldsymbol{v} = 0. \tag{4.2}$$

Equations (4.1) and (4.2) with relevant prescribed boundary conditions are solved to obtain the velocity field.

For the reactive part, we consider the two equilibrium reactions in Chapter 2. However, we neglect the contribution of the precipitates in changing the porosity of the medium here. Hence, the total concentration are defined similar to Equation (2.6) on page 8 and using the same notation:

$$N_A = n_A \phi + m_A, \tag{2.6a}$$
$$N_B = n_B \phi + m_B, \tag{2.6b}$$

In the above definitions, we have dropped the index p for porosity, ϕ_P, for simplicity.

The mass balance for this system in multi-dimension reads,

$$\frac{\partial N_\pi}{\partial t} + \nabla \cdot (\boldsymbol{v} n_\pi) = 0, \quad \pi = \{\mathrm{A}, \mathrm{B}\},\ \boldsymbol{x} \in \Omega \subset \mathbb{R}^3,\ t > 0, \tag{4.4a}$$

with the initial compositions

$$N_\pi(x, t = 0) = N_\pi(x), \tag{4.4b}$$

and appropriate boundary condition on $\partial\Omega$.

4.2 STREAMLINE SIMULATION

We choose a combination of streamline and front-tracking methods to solve Equation (4.4) numerically for several reasons. First, the inherent numerical diffusion in finite-volume methods will often overestimate or underestimate the amount of precipitate. As we will see in Section 4.3, the analytical solution for the one-dimensional case involves contact discontinuities in many cases. For contact discontinuities, the characteristic wave speeds are equal on both sides of the propagating discontinuity. Unlike multiphase displacement fronts, these discontinuities do not have any inherent self-sharpening mechanism and are therefore more susceptible to numerical smearing when solved with a low-order finite-volume scheme. Second, general numerical methods are not computationally efficient for Equation (4.4a). The flux functions n_π are not differentiable across the boundary curves on the hodograph plane (see Section 4.3.1) for constant

values of ϕ. This non-differentiability imposes restrictions on time steps for implicit finite-volume methods because standard Newton solvers fail to converge for large time steps. Non-smooth variations of ϕ in space render the flux function discontinuous which in turn introduces more difficulty in implementing finite-volume methods. Third, the analytical solution for the simplified case is already developed [1] and we can develop a more general case based on that. Availability of the analytical solution for the one-dimensional Riemann Problem makes the problem well suited for front-tracking. Finally, streamline methods can often be more computationally efficient than finite-volume methods in large domains and highly heterogeneous media [58].

4.2.1 *Flow in the reservoir*

In this section, we provide a streamline method to simulate the reactive flow in a porous medium. In a streamline simulator, we convert the multidimensional transport equations into a set of simpler one-dimensional equations. Each one-dimensional problem explains the propagation of quantities along one *streamline*. A streamline at an instance of time is a curve that is everywhere tangential to the velocity field. Therefore, two streamlines can never cross and the transport along a streamline is a one-dimensional problem [58].

Herein, we will only solve the flow equations, Equations (4.1) and (4.2), on rectilinear grids. This means that we can use a variant of Pollock's method [94] to trace streamlines. In streamline methods for typical problems, e.g., tracer transport or 2-phase flow saturation calculation, the streamlines are traced using Pollock's method by calculating the *time-of-flight* for an arbitrary particle at initial position $\boldsymbol{x}_i$. The time-of-flight τ^* is defined as the time that is required for a particle at $\boldsymbol{x}_i$ to reach a certain position $\boldsymbol{x}$,

$$\tau^* = \int_{\boldsymbol{x}_i}^{\boldsymbol{x}} \frac{\phi}{|\boldsymbol{v}|} \, \mathrm{d}\xi. \tag{4.5}$$

The integral in the above definition is along the particle path. Here, we use a modified definition of time-of-flight that does not include ϕ, i. e.,

$$\tau = \int_{\boldsymbol{x}_i}^{\boldsymbol{x}} \frac{1}{|\boldsymbol{v}|} \, \mathrm{d}\xi. \tag{4.6}$$

The reason we use this definition is two-folds. First, we can reconstruct the one-dimensional form of Equation (4.4a) along a streamline with no explicit depend-

ence on ϕ. The result is similar to a truly one-dimensional problem. To reconstruct the one-dimensional form (as in Chapter 3),

$$\frac{\partial N_\pi}{\partial t} + \frac{\partial n_\pi}{\partial x} = 0, \tag{3.5}$$

we expand the divergence operator in Equation (4.4a) and use Equation (4.2) and the differential form of Equation (4.6), i. e.,

$$\boldsymbol{v} \cdot \nabla \tau = 1.$$

The result is the one-dimensional problem in time-of-flight coordinates

$$\frac{\partial N_\pi}{\partial t} + \frac{\partial n_\pi}{\partial \tau} = 0. \tag{4.7}$$

Second, for streamline methods, the porosity only occurs explicitly in the temporal derivative. Here, in contrast, in Equation (4.4a) both terms n_π and N_π are functions of ϕ. This means that the one-dimensional wave speeds in Equation (4.7) will involve ϕ, whereas in other streamline methods, the effect of ϕ on the wave speed is accounted for in τ and not seen in the one-dimensional equations.

Note that the reconstruction of the homogeneous one-dimensional problem is possible even in the case that the contribution of the precipitates in changes of the porosity are taken into account. In this case, the derivation of transport along streamlines remains identical because of the ideality assumption for the solid-liquid solution (volume conservation) whichs retain a free flow-field, i. e., Equation (4.2) holds true. However, for several pairs of the salts (sulphates for example), the contribution of precipitates in changing of porosity is negligible. Thus, for the sake of simplicity we assume porosity is not altered in the course of transport. It should be also noted that while relaxing this assumption, the effect of changes of porosity on the permeability needs to be accounted for using Kozney-Carman or some other equations ([95]). Nevertheless, the Riemann Problem associated with a heterogeneous medium becomes more complicated than the one discussed in Section 4.3.2.

After the propagation along the streamlines, the solutions are mapped back on to the spatial grid. The overall value of quantities for each cell is calculated using the contribution of each streamline that passes through that cell. The result of the

one-dimensional solver for each streamline is averaged to yield the concentration on each cell in the multidimensional domain using the following equation

$$N_{\pi,j} = \frac{\sum_{i=1}^{nsl} V_i \tau_{i,j} N_{\pi,i,j}}{\sum_{i=1}^{nsl} V_i \tau_{i,j}}, \tag{4.8}$$

where nsl represents the number of streamlines and $\tau_{i,j}$ is the incremental time-of-flight of streamline i at cell j and V_i is the amount of fluid that streamline i carries [96].

To evaluate the amount of fluid V_i that each streamline carries, we use the method suggested in [97]. We distribute the injected fluid on the outflow faces of the inlet cells in the Eulerian grid. An inlet cell is defined as a cell through which fluid is injected into the domain. In this regard, each streamline is associated with a conceptual stream-tube. The boundaries of these stream-tubes are constructed by bisecting the location of streamlines on the outflow faces of the inlet cell. The width of each stream-tube is proportional to the amount of flow of its corresponding streamline. Hence, the fluid is distributed to the streamlines according to the weights that are determined by the width of each stream-tube. We assume that at for each rectilinear grid, there exist at least one streamline that passes that grid. Therefore, all regions are sampled by at least one streamline.

If the flow field changes for any reason, it has to be reflected on the streamlines. Hence, after a simulation from time $t_0 = 0$ to t_1, the quantities are mapped to the Eulerian grid (using e.g., Equation (4.8)), the flow field is recalculated and the fronts are propagated from t_1 to t_2. This introduces a special type of numerical diffusion that may smear the fronts. For this problem, however, we will not consider any scenarios that change the flow field and hence it remains constant. Herein, we run the simulation always from $t_0 = 0$ to any time t and therefore, the results are free from any error caused by numerical dispersion. This does not hold true if the velocity field does not remain constant due to, for example, considerable changes of precipitate in one region of the medium.

4.2.2 *Mixing at well*

In many circumstances, such as during the water-flooding, the flow is dominated by advection, and thus mixing through diffusion is limited in the reservoir. However, at the well all streamlines converge and mixing takes place. If this mixing results in an excessive production of precipitates (scales), the well will clog and the flow stops. Scaling requires very expensive remediation strategies. In this section, we provide a model for mixing of streamlines at the well to estim-

ate the concentration and the amount of produced precipitates. We assume that all streamlines converge at the well and only at the well. We assume that the streamlines mix and reach equilibrium in a certain volume V_w. In this volume, precipitates form if the molar content of a species exceeds its saturation value. The fluid mixture without the precipitate then leaves the well towards the surface. The subsequent dynamics are not addressed here. The mass balance for the components at the well reads as

$$\boldsymbol{N}(t_k + \delta t) = \boldsymbol{N}(t_k) + \frac{\boldsymbol{f}_{\text{in}} - \boldsymbol{f}_{\text{out}}}{V_w}\delta t, \tag{4.9}$$

where $\boldsymbol{f}_{\text{in}}$ and $\boldsymbol{f}_{\text{out}}$ are the molar inflow and outflow of ions to the well, respectively. According to our mixing assumption, we set δt such that at the next time step, the well contents are completely swept out and replaced by the new mixture of streamlines. More discussion on mixing is provided in the next chapter and a method is suggested for coupling flow and transport. We approximate $\boldsymbol{f}_{\text{in}}$ and $\boldsymbol{f}_{\text{out}}$ as constant values from t_k to $t_k + \delta t$. Given the total flow rate q we obtain the time step δt from the following relation

$$\delta t = \frac{V_w}{q}. \tag{4.10}$$

For the molar inflow we have

$$\boldsymbol{f}_{\text{in}} = \delta t \sum_{i=1}^{nsl} q_i \boldsymbol{n}_i(t_k), \tag{4.11}$$

where q_i denotes the flux of streamline i and $\boldsymbol{n}_i(t_k)$ is the vector of concentrations at time t_k associated with streamline i. Note that we have used $\boldsymbol{n}$ and not $\boldsymbol{N}$ in Equation (4.11) because the precipitates do not move and it is only the fluids that mix at the well. The molar outflow is expressed via the following equation

$$\boldsymbol{f}_{\text{out}} = \delta t \bar{\boldsymbol{n}}(t_k) \sum_{i=1}^{nsl} q_i, \tag{4.12}$$

where $\bar{\boldsymbol{n}}(t_k)$ is the concentration of the equilibrated outflow from the well at time t_k. The summation in the Equation (4.12) yields the total out-flux from the well q. Using the definition of $\boldsymbol{N}$ and Equations (4.11) and (4.12) in Equation (4.9) with $\phi = 1$ yields

$$\boldsymbol{N}(t_k + \delta t) = \bar{\boldsymbol{n}}(t_k) + \boldsymbol{N}(t_k) + \frac{\delta t}{V_w}\left(\sum_{i=1}^{nsl} q_i \boldsymbol{n}_i(t_k) - q\bar{\boldsymbol{n}}(t_k)\right), \tag{4.13}$$

with $\boldsymbol{m} = (m_A, m_B)^T$. Inserting the value of δt (Equation (4.10)) in Equation (4.13) yields the total amount of components at the next time step

$$\boldsymbol{N}(t_k + \delta t) = \frac{1}{q} \sum_{i=1}^{nsl} q_i \boldsymbol{n}_i(t_k) + \boldsymbol{m}(t_k) \tag{4.14}$$

The average value of concentrations in the fluid at the next time step $\bar{\boldsymbol{n}}(t_k + \delta t)$ and the amount of precipitates $\boldsymbol{m}(t_k + \delta t)$ is calculated using the corresponding functions (from Appendix A.4) for $\boldsymbol{n}$ and $\boldsymbol{m}$ with $\phi = 1$ and $\boldsymbol{N}(t_k + \delta t)$ obtained from Equation (4.14).

Note that we have not used any spatial resolution for the well in deriving Equation (4.14). In fact, we only post-process the results from the streamline simulator. Note further that V_w is a model parameter that represents the mixing volume in the well. To obtain the history of concentration $\bar{\boldsymbol{n}}(t_k)$ and the amount of precipitate at the well $\boldsymbol{m}(t_k)$, we need to iterate through Equation (4.14) with the estimated value for δt. An interpolation might be required since δt and the time step for the streamline simulator are not essentially equal.

4.3 FRONT TRACKING AND RIEMANN SOLVER

The initial conditions for Equation (4.7) are piece-wise constant because a streamline passes through several cells that potentially have different concentration of components. We first discuss the solution for the case with a single discontinuity in the initial compositions. In Section 4.3.3, we combine Riemann solutions to construct the global solution for several discontinuities using front-tracking.

The solution to the Riemann Problem follows from Helfferich [1]. It can also be constructed as a special case to the solution provided in Chapter 3 when $(\omega_A, \omega_B) \to (\infty, \infty)$. In the next subsection, we give a summary of the Riemann solution. The solution and the analysis apply to the case where the porosity of the medium is constant. This solution is extended to involve heterogeneities of the system in the second subsection.

4.3.1 *Solution for constant porosity*

Figure 4.1 shows the hodograph plane for this problem which is very similar to the one obtained in Chapter 3 (Figure 3.1 on page 22). The difference here is that there is no unphysical region in this case as the volume of precipitates are ignored. The separating curves for the four regions discussed in section 2.2

are constructed by solving the chemical equations (2.1) similar to the procedure explained in Section 3.1:

$$A^{BU} := \left\{ N_B = \frac{(\phi\tilde{n}_A)^2}{N_A} - N_A \right\}, \tag{4.15a}$$

$$B^{AU} := \left\{ N_A = \frac{(\phi\tilde{n}_A)^2}{N_B} - N_B \right\}, \tag{4.15b}$$

$$A^{BS} := \{ N_A = \phi\tilde{n}_A \}, \tag{4.15c}$$

$$B^{AS} := \{ N_B = \phi\tilde{n}_B \}. \tag{4.15d}$$

The four regions in the hodograph plane can be defined as in Equation (3.9) on page 21 with separating curves defined in Equation (4.15).

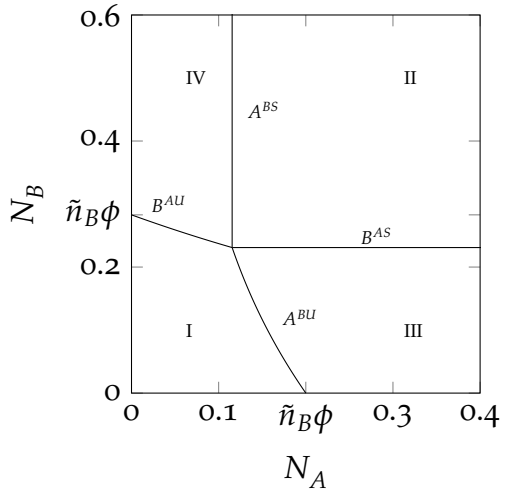

Figure 4.1: Hodograph plane and the separating curves for $k_A = 1, k_B = 2, \phi = 0.2$. A fluid in region $AUBU$ is unsaturated, whereas in region $ASBS$, it is saturated with both components and therefore both precipitates exist. In region $ASBU$, we have precipitates of A, but the fluid is unsaturated with respect to B. Region $AUBS$ is the reverse of region $ASBU$. The boundary curve between region $AUBU$ and $ASBU$, where A becomes saturated but B remains unsaturated, is labelled as A^{BU}. The boundary curve B^{AU} is similarly defined. The horizontal and vertical lines are the other two boundaries denoted by B^{AS} and A^{BS}, respectively. The triple point with coordinates $\boldsymbol{N}_t = (\hat{n}_A\phi, \hat{n}_B\phi)^T$ is defined as the intersection of all the boundary curves.

The $\mathcal{I}_1$ curves in regions $ASBU$ are straight lines that start from boundary curve A^{BU} and are parallel to x-axis. The $\mathcal{I}_1$ curves coincide with $\mathcal{H}_1$ curves for points in $AUBU$. The $\mathcal{I}_2$ curves are again iso-porous curves.

The analytical solution is obtained case by case depending on the location of the endpoints $\boldsymbol{N}_l$ and $\boldsymbol{N}_r$ of the initial discontinuity:

- **Case 1, 2:** Case 1 refers to $\boldsymbol{N}_l$ and $\boldsymbol{N}_r$ being in region $AUBU$. The solution for this case is only a simple wave $\boldsymbol{N}_l \xrightarrow{\mathcal{C}_2} \boldsymbol{N}_r$, and the two PDEs decouple. Case 2 refers to the case where both states lie in region $ASBS$. The solution

for this case is similar in that it is only one wave, but now this single wave is stationary because both eigenvalues of the Jacobian matrix are zero.

- **Case 3, 4:** In Case 3, both left and right states belong to region $ASBU$ and in Case 4 they both lie in region $AUBS$. The solution for Case 3 is illustrated in Figure 4.2a. The solution in notation of waves and an intermediate state is $\boldsymbol{N}_l \xrightarrow{\mathcal{C}_1} \boldsymbol{N}_i \xrightarrow{\mathcal{C}_2} \boldsymbol{N}_r$, where $\boldsymbol{N}_i$ is the intersection of the horizontal line from $\boldsymbol{N}_l$ and the $\mathcal{I}_2$ curve from $\boldsymbol{N}_r$ in region $ASBU$ ($\mathcal{I}_1(\boldsymbol{N}_l)$ and $\mathcal{I}_2(\boldsymbol{N}_r)$). Case 4 has an equivalent structure.

Cases 5 to 9 refer to the situations where the upstream composition has more precipitate than the downstream composition. They all have a similar structure: a stationary wave followed by a fast transport wave because precipitates do not move with the fluid. The notation for the solution reads $\boldsymbol{N}_l \xrightarrow{\mathcal{C}_1} \boldsymbol{N}_i \xrightarrow{\mathcal{C}_2} \boldsymbol{N}_r$.

- **Case 5, 6:** The initial condition for Case 5 is $\boldsymbol{N}_l \in ASBS$, $\boldsymbol{N}_r \in ASBU$ (and $\boldsymbol{N}_r \in AUBS$ for Case 6). The solution for Case 5 in the hodograph plane is illustrated in Figure 4.2b. The intermediate state for Case 5 is the intersection of $\mathcal{I}_2(\boldsymbol{N}_r)$ and the boundary line B^{AS}. The solution for Case 6 follows the same structure.

- **Case 7, 8:** Case 7 refers to state $\boldsymbol{N}_l$ being in $ASBU$ ($AUBS$ for Case 8) and $\boldsymbol{N}_r$ in $AUBU$. For Case 7, the intermediate state is the intersection of $\mathcal{I}_1(\boldsymbol{N}_l)$ and the boundary curve A^{BU}. The concentration of A for $\boldsymbol{N}_i$ is equal to that of $\boldsymbol{N}_l$. Case 8 has a similar structure with difference that the stationary wave keeps the concentration of B fixed, i. e., $N_B^l = N_B^i$.

- **Case 9:** Case 9 is $\boldsymbol{N}_l \in ASBS$ and $\boldsymbol{N}_r \in AUBU$. The intermediate state in this case is the intersection of all the boundary curves in the hodograph plane denoted by the $\boldsymbol{N}_t$.

Cases 10 to 14 describe the solution for cases where the upstream is relatively fresher than the downstream, i. e., the left composition belongs to a region with less precipitate in the solution. The solution for these cases involves at least one shock $\mathcal{S}_1$ or $\mathcal{S}_2$.

- **Case 10, 11:** Case 10 refers to the situation where $\boldsymbol{N}_l \in ASBU$ and $\boldsymbol{N}_r \in$ II. The solution for this case is a stationary wave followed by a fast shock $\boldsymbol{N}_l \xrightarrow{\mathcal{C}_1} \boldsymbol{N}_i \xrightarrow{\mathcal{S}_2} \boldsymbol{N}_r$. Point $\boldsymbol{N}_i$ is the intersection of $\mathcal{I}_1(\boldsymbol{N}_l)$ and $\mathcal{H}_2(\boldsymbol{N}_r)$ and lies in region $ASBU$. Case 11 has a similar structure with $\boldsymbol{N}_i$ in region $AUBS$.

- **Case 12, 13:** In Case 12, $\boldsymbol{N}_l$ lies in region $AUBU$ and $\boldsymbol{N}_r$ in $ASBU$. The slow wave for the solution to this case is $\mathcal{S}_1$ and the fast wave is $\mathcal{C}_2$. Hence, we expect to obtain $\boldsymbol{N}_i$ in region $ASBU$ by intersecting $\mathcal{H}_1(\boldsymbol{N}_l)$ with $\mathcal{I}_2(\boldsymbol{N}_r)$.

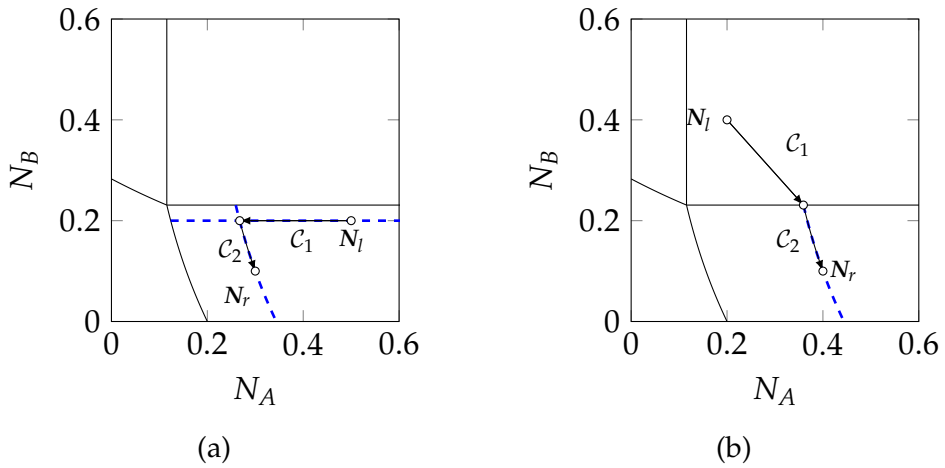

Figure 4.2: Structure of the solution for (a) Case 3 and (b) Case 5. Each arrow represents a wave that is labelled with its family 1 or 2. The dashed blue lines are integral curves. The point between $\mathcal{C}_1$ and $\mathcal{C}_2$ is $\boldsymbol{N}_i$.

However, it is not always possible to find the intersection $\boldsymbol{N}_i$ inside region $ASBU$ due to the structure of the flux function n_π. In fact, if $N_B^l > \phi \hat{n}_B$ for $\boldsymbol{N}_l = \left(N_A^l, N_B^l\right)^T$, then the second wave becomes compound. However, we do not have rarefactions in this system and the compound wave appears in the form of a shock-contact wave. This compound wave arises a new intermediate state $\boldsymbol{N}_{i2}$. The second intermediate states $\boldsymbol{N}_{i2}$ in the complete solution $\boldsymbol{N}_l \xrightarrow{\mathcal{S}_1} \boldsymbol{N}_{i1} \xrightarrow{\mathcal{S}_2} \boldsymbol{N}_{i2} \xrightarrow{\mathcal{C}_2} \boldsymbol{N}_r$ lies on the intersection of $\mathcal{I}_2\left(\boldsymbol{N}_r\right)$ and the boundary line B^{AS} between regions $ASBU$ and $ASBS$. Point $\boldsymbol{N}_{i1}$ lies on the intersection of $\mathcal{H}_2\left(\boldsymbol{N}_i\right)$ and $\mathcal{H}_1\left(\boldsymbol{N}_l\right)$ in region $AUBS$. The solution for Case 13 is similar in structure.

- **Case 14:** Here, we consider dissolution of both salts with an unsaturated fluid, hence $\boldsymbol{N}_l \in AUBU$, $\boldsymbol{N}_r \in ASBS$. The solution for this case involves two shocks, $\boldsymbol{N}_l \xrightarrow{\mathcal{S}_1} \boldsymbol{N}_i \xrightarrow{\mathcal{S}_2} \boldsymbol{N}_r$, thus a combination of Cases 10 to 14. Point $\boldsymbol{N}_i$ can be either in region $ASBU$ or $AUBS$ or it can disappear. Helfferich concluded that if $\boldsymbol{N}_l$ is below the line passing through $\boldsymbol{N}_r$ and the triple point, then $\boldsymbol{N}_i$ will be in region $ASBU$ to satisfy $\bar{v}\left(\mathcal{S}_2\right) > \bar{v}\left(\mathcal{S}_1\right)$. Figure 4.3a shows the solution for this case. On the other hand, if $\boldsymbol{N}_l$ lies above the line, the admissible value for $\boldsymbol{N}_i$ is in region $AUBS$. For the case that $\boldsymbol{N}_l$ is exactly on this line the two shocks have the same velocity, merge and state $\boldsymbol{N}_i$ disappears.

Two more special cases are considered as Cases 15 and 16.

- **Case 15, 16:** In Case 15 we analyse the solution for $\boldsymbol{N}_l \in ASBU$ and $\boldsymbol{N}_r \in AUBS$, which is a combination of Cases 7 and 13. This case is illustrated in Figure 4.3b. The solution involves a compound shock-contact wave and hence there are two intermediate states $\boldsymbol{N}_{i1}$ and $\boldsymbol{N}_{i2}$. The full solution is

$\boldsymbol{N}_l \xrightarrow{\mathcal{C}_1} \boldsymbol{N}_{i1} \xrightarrow{\mathcal{S}_2} \boldsymbol{N}_{i2} \xrightarrow{\mathcal{C}_2} \boldsymbol{N}_r$ where $\boldsymbol{N}_{i2}$ is the intersection of $\mathcal{I}_2(\boldsymbol{N}_r)$ and the boundary curve A^{BS} between regions $ASBS$ and $AUBS$. Since $\boldsymbol{N}_{i2}$ is on the boundary, it belongs to both regions $ASBS$ and $AUBS$. Therefore, the rest of the solution follows as Case 10, i. e., $\boldsymbol{N}_{i1} = \mathcal{I}_1(\boldsymbol{N}_l) \cap \mathcal{H}_2(\boldsymbol{N}_{i2})$. The solution for Case 16 follows a similar structure to that of Case 15.

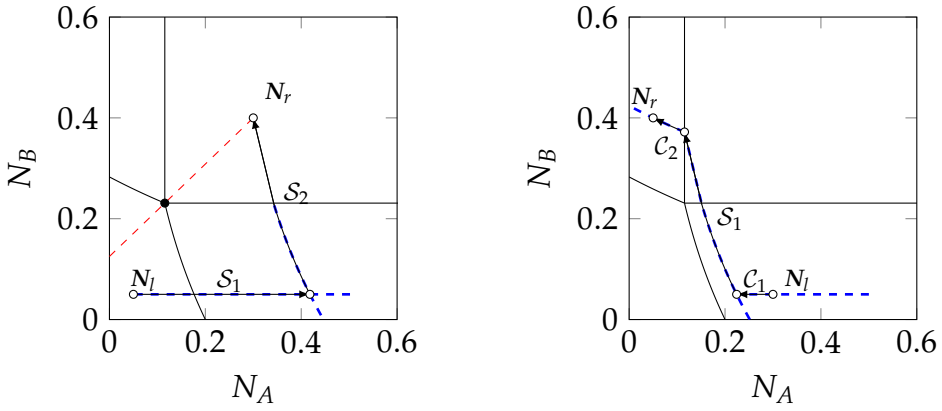

Figure 4.3: Structure of the solution for (a) Case 14 and (b) Case 15. Integral curves and Hugoniot loci are shown by thick dashed blue curves. The red dashed line in figure (a) passes through $\boldsymbol{N}_r$ and the triple point (shown by a solid point) and determines the location of $\boldsymbol{N}_i$.

4.3.2 *Solution for variable porosity*

In this section, we present the solution for the Riemann Problem when the porosity is spatially discontinuous in addition to discontinuities in the concentrations. Hence, the problem is given by

$$\frac{\partial \boldsymbol{N}}{\partial t} + \frac{\partial \boldsymbol{n}}{\partial x} = 0, \tag{4.16a}$$

$$\frac{\partial \phi}{\partial t} = 0, \tag{4.16b}$$

$$\boldsymbol{N}(x,0) = \begin{cases} \boldsymbol{N}_l, & x < 0, \\ \boldsymbol{N}_r, & x > 0, \end{cases} \tag{4.16c}$$

$$\phi(x,0) = \begin{cases} \phi_l, & x < 0, \\ \phi_r, & x > 0. \end{cases} \tag{4.16d}$$

Generally speaking, the flux functions n_π depend on the primary variables N_π with porosity acting as a parameter, i. e., $n_\pi = n_\pi(N_A, N_B; \phi)$. Hence, Equation (4.16) can be decoupled into two separate problems.

We aim to obtain the analytical solution by transforming Equation (4.16) into two systems and analysing the behaviour on the interface in between where we have discontinuity of the quantities. This is similar to the scalar case in which one finds the global solution using the minimum jump entropy condition across the interface [62, 63, 98]. Equation (4.16) is decoupled into two problems

$$\frac{\partial \boldsymbol{N}}{\partial t} + \frac{\partial}{\partial x}\boldsymbol{n}_l(N_A, N_B) = 0, \tag{4.17a}$$

$$\boldsymbol{N}(x,0) = \begin{cases} \boldsymbol{N}_l & x < 0, \\ \boldsymbol{N}_l' & x = 0, \end{cases} \tag{4.17b}$$

and

$$\frac{\partial \boldsymbol{N}}{\partial t} + \frac{\partial}{\partial x}\boldsymbol{n}_r(N_A, N_B) = 0, \tag{4.18a}$$

$$\boldsymbol{N}(x,0) = \begin{cases} \boldsymbol{N}_r' & x = 0, \\ \boldsymbol{N}_r & x > 0, \end{cases} \tag{4.18b}$$

with $\boldsymbol{n}_l(\cdot,\cdot) := \boldsymbol{n}(\cdot,\cdot;\phi_l)$ and $\boldsymbol{n}_r(\cdot,\cdot) := \boldsymbol{n}(\cdot,\cdot;\phi_r)$. Given that $\boldsymbol{N}(x,0^-)$ from Equation (4.17) and $\boldsymbol{N}(x,0^+)$ from Equation (4.18) satisfy additional condition [61, 67], each of the problems Equations (4.17) and (4.18) has a unique solution according to the previous section. It remains to find the states $\boldsymbol{N}_l'$ and $\boldsymbol{N}_r'$ to concatenate these solutions together. In addition, $\frac{\partial \phi}{\partial t}$ in Equation (4.16) suggests that there is a stationary wave accounting for the discontinuity of porosity[1]. Thus, we seek the endpoints of the aforementioned stationary wave, $\tilde{\mathcal{W}}_0$, $\boldsymbol{N}_l'$ and $\boldsymbol{N}_r'$ that account for the porosity change. This wave glues the weak solution of Equation (4.17) to that of Equation (4.18).

We first find admissible values for $\boldsymbol{N}_l'$. The solution to Equation (4.17) should not have any waves with positive speed because the wave to the right of this solution, i. e., $\tilde{\mathcal{W}}_0$, is stationary. It is not possible to have any waves with negative velocity either, because the eigenvalues of the Jacobian matrix are always non-negative. Hence, the solution to Equation (4.17) can contain only stationary waves. This means that the solution to Equation (4.17) is a stationary wave and is to the left of another stationary wave $\tilde{\mathcal{W}}_0$ between $\boldsymbol{N}_l'$ and $\boldsymbol{N}_r'$. They both start at the same position $x = 0$ and as a result, the two waves merge and the state in between, $\boldsymbol{N}_l'$, disappears. The conclusion is $\boldsymbol{N}_l = \boldsymbol{N}_l'$.

1 Obviously, this wave is stationary due to the construction of the problem i. e., heterogeneity of medium.

To evaluate the state $\boldsymbol{N}_r'$, we use the conservation of flux across the interface, i. e.,

$$n_A^l\left(\boldsymbol{N}_l\right) = n_A^r\left(\boldsymbol{N}_r'\right), \quad n_B^l\left(\boldsymbol{N}_l\right) = n_B^r\left(\boldsymbol{N}_r'\right). \tag{4.19}$$

In Equation (4.19), we are stating that only the dissolved ions in the fluid travel. This is in accordance with our assumption that precipitates are stationary. Unfortunately, this condition is not enough to ensure a unique value for $\boldsymbol{N}_r'$ since neither of the four mappings $N_A \mapsto n_A(N_A, \cdot)$, $N_B \mapsto n_A(\cdot, N_B)$, $N_A \mapsto n_B(N_A, \cdot)$ nor $N_B \mapsto n_B(\cdot, N_B)$ is surjective. We look at this problem case by case depending on the values of n_A and n_B for $\boldsymbol{N}_l$, i. e., location of $\boldsymbol{N}_l$ in the hodograph plane. We identify four cases depending on the location of $\boldsymbol{N}_r$.

1. If $\boldsymbol{N}_l$ is not saturated with any of the salts, $\boldsymbol{N}_r'$ is uniquely determined using Equations (4.19) and (A.6), i. e., $N_A^r = N_A^l \frac{\phi_r}{\phi_l}$ and $N_B^r = N_B^l \frac{\phi_r}{\phi_l}$.

2. If $\boldsymbol{N}_l$ is saturated with A and unsaturated with B (i. e., $\boldsymbol{N}_l$ belongs to region III in Figure 4.1), then $\boldsymbol{N}_r'$ should also belong to region $ASBU$ so that the flux is conserved. To show this, we pick $\boldsymbol{N}_l = \left(N_A^l, N_B^l\right)^T \in ASBU$, then solving Equation (4.19) for $\boldsymbol{N}_r'$ yields

$$\boldsymbol{N}_r' \in \mathcal{D} = \left\{ \boldsymbol{N} = (N_A, N_B)^T \,\middle|\, N_B = \frac{\phi_r}{\phi_l} N_B^l, \; N_A \geq \frac{1}{2}\left(\sqrt{N_B^2 + 4\phi_r^2 \tilde{n}_A^2} - N_B\right) \right\}, \tag{4.20}$$

   using Equations (A.6) to (A.9). The set $\mathcal{D}$ is a horizontal line that lies under the line $N_B = \phi_r \hat{n}_B$ because $N_B^l < \phi_l \hat{n}_B$. On the other hand, the point with the minimum value of N_A lies on the boundary curve A^{BU} (c.f. Equation (4.15a)). Hence, the set $\mathcal{D}$ completely lies in region $ASBU$ and we have infinite possible candidates for $\boldsymbol{N}_r'$. In the following, we first show that the global solution to Equation (4.16) is independent of $\boldsymbol{N}_r'$. We select an arbitrary value for $\boldsymbol{N}_r'$ in the set $\mathcal{D}$ so that we can construct a solution for Equation (4.18).

   The solution to Equation (4.18) with $\boldsymbol{N}_r'$ saturated in A involves a stationary wave (possibly) followed by non-stationary waves. To show this, we consider four cases for location of $\boldsymbol{N}_r$ and we refer to the corresponding case number in the previous section for details.

   a) $\boldsymbol{N}_r \in$ I: $\boldsymbol{N}_r' \xrightarrow{\mathcal{C}_1} \boldsymbol{N}_i \xrightarrow{\mathcal{C}_2} \boldsymbol{N}_r$ (Case 7)

   b) $\boldsymbol{N}_r \in$ II: $\boldsymbol{N}_r' \xrightarrow{\mathcal{C}_1} \boldsymbol{N}_i \xrightarrow{\mathcal{S}_2} \boldsymbol{N}_r$ (Case 10)

   c) $\boldsymbol{N}_r \in$ III: $\boldsymbol{N}_r' \xrightarrow{\mathcal{C}_1} \boldsymbol{N}_i \xrightarrow{\mathcal{C}_2} \boldsymbol{N}_r$ (Case 3)

d) $N_r \in$ IV: $N_r' \xrightarrow{\mathcal{C}_1} N_{i1} \xrightarrow{\mathcal{S}_1} N_{i2} \xrightarrow{\mathcal{C}_2} N_r$ (Case 15)

In summary, if N_r' belongs to region $ASBU$, the solution to Equation (4.18) always involves the stationary wave $\mathcal{C}_1$. Thus, the two stationary waves in sequence, ($\tilde{\mathcal{W}}_0$) and the first wave in the solution of Equation (4.18) ($\mathcal{C}_1$), merge and the state in between (N_r') disappears. In other words, the solution for this case is independent of N_r'. However, to be able to construct the solution for Equation (4.18), we choose N_r' to be the intersection of the boundary curve A^{BU} and the set $\mathcal{D}$. Figure 4.4 illustrate solutions to the above four cases (a) to (d) with $\phi_l = 0.1$ and $\phi_r = 0.3$.

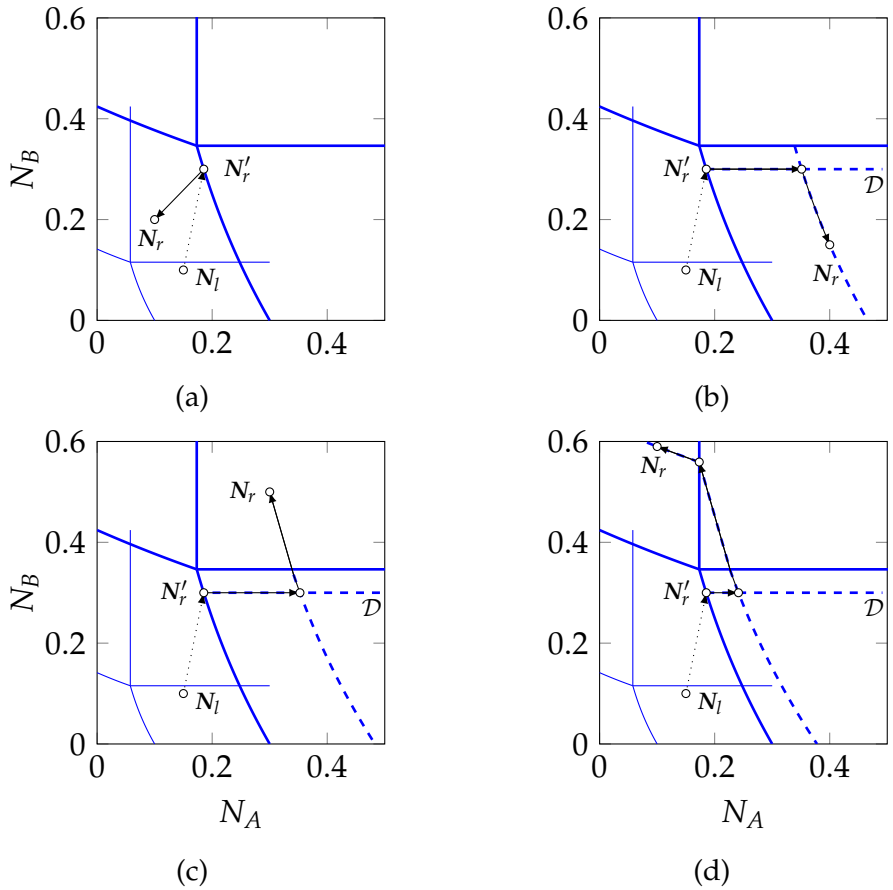

Figure 4.4: Solution on the hodograph plane for the case when $N_l \in ASBU$. The hodograph with thin solid curves correspond to $\phi_l = 0.1$ and the thick ones are for $\phi_r = 0.3$. The dotted arrow represents the stationary wave $\tilde{\mathcal{W}}_0$. Set $\mathcal{D}$ is shown in Figures b, c and d which coincides with $\mathcal{I}_1(N_r')$. The integral curves and Hugoniot loci are shown by dashed blue curves for hodograph plane with $\phi_r = 0.3$.

3. If N_l is saturated with B and unsaturated with respect to A, the solution follows the same structure as in the previous case. State N_r' is chosen to lie on the intersection of B^{AU} and the corresponding vertical line.

4. Finally, when the left composition is completely saturated (i. e., N_l belongs to region $ASBS$) the situation is analogous to the previous two cases. There

are infinitely many possibilities for $\boldsymbol{N}_r'$ such that $\boldsymbol{n}_l(\boldsymbol{N}_l) = \boldsymbol{n}_r(\boldsymbol{N}_r)$ (basically any point in region $ASBS$). However, the Riemann solution with left composition in this region always contains a stationary wave, c.f. Cases 2, 5, 6 and 9 in Section 4.3.1. Hence the solution is independent of the state $\boldsymbol{N}_r'$. The simplest choice for $\boldsymbol{N}_r'$ is $\boldsymbol{N}_r' = \begin{pmatrix} \phi_r \hat{n}_A \\ \phi_r \hat{n}_B \end{pmatrix}$ (the intersection of all of the separating curves).

In summary, we have proved the admissible set for $\boldsymbol{N}_l'$ is $\{\boldsymbol{N}_l\}$ and the admissible set for $\boldsymbol{N}_r'$ in the set $\mathcal{D}$. In addition, for any values of $\boldsymbol{N}_r'$ in $\mathcal{D}$ we obtain the same solution, because $\boldsymbol{N}_r'$ does not appear in the solution.

4.3.3 *Front-tracking*

Sections 4.3.1 and 4.3.2 described the solution for a single discontinuity whereas the initial condition for Equation (4.7) has several discontinuities. Hence, initially, we need to solve several Riemann Problems. The solution waves from these Riemann Problems might collide at later times in different locations. Every time two or more waves collide, a new Riemann Problem appears and needs to be solved. The process of following each front to calculate the time and location of collisions is called front-tracking [59, 83].

Figures 4.5 and 4.6 illustrate the front-tracking idea in the characteristic plot. Characteristics are curves in x-t plane along which the solution remains constant. Figure 4.5 shows the characteristics of a problem with a given initial condition. Each of the lines in Figure 4.5 represents a wave that travels with the constant speed equal to the inverse of the slope of that line. In the x-t characteristic plane, these collisions are represented by intersecting lines. Figure 4.6 illustrates an example of intersecting characteristic curves. In this example, an unsaturated solution is used to dissolve precipitates in a homogeneous system. The system initially contains a bank of precipitate B ($x \in [0.05, 0.4]$) followed by both precipitates ($x \in [0.45, 0.6]$) and precipitate A ($x \in [0.6, 0.75]$) with gradual transition between each bank.

In our implementation, we have used two doubly linked lists. The first list (X-list) contains all the discontinuities and is sorted by the location of each discontinuity. Initially at $t = 0$, we have only the X-list. Each discontinuity in the X-list is represented by the solution waves of its corresponding Riemann Problem. The collision time for every two neighbouring waves are computed and the collisions are stored in the second list (T-list). The T-list is sorted with respect to the collision times. All waves are propagated until the first collision (from T-list) occurs. The Riemann Problem for the corresponding collision is solved and the solution is replaced by the colliding waves in the X-list. The T-list is updated

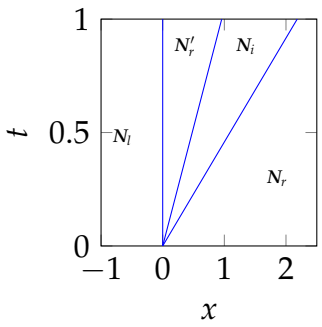

Figure 4.5: Characteristic plot for the solution of Equations (4.7) and (3.11) with $\boldsymbol{N}_l = (0.05, 0.05)^T$, $\phi_l = 0.1$ and $\boldsymbol{N}_r = (0.3, 0.4)^T$, $\phi_r = 0.2$.

based on the collision of the new waves with their neighbours. The algorithm stops when there are no collisions or when the next collision happens after the simulation time.

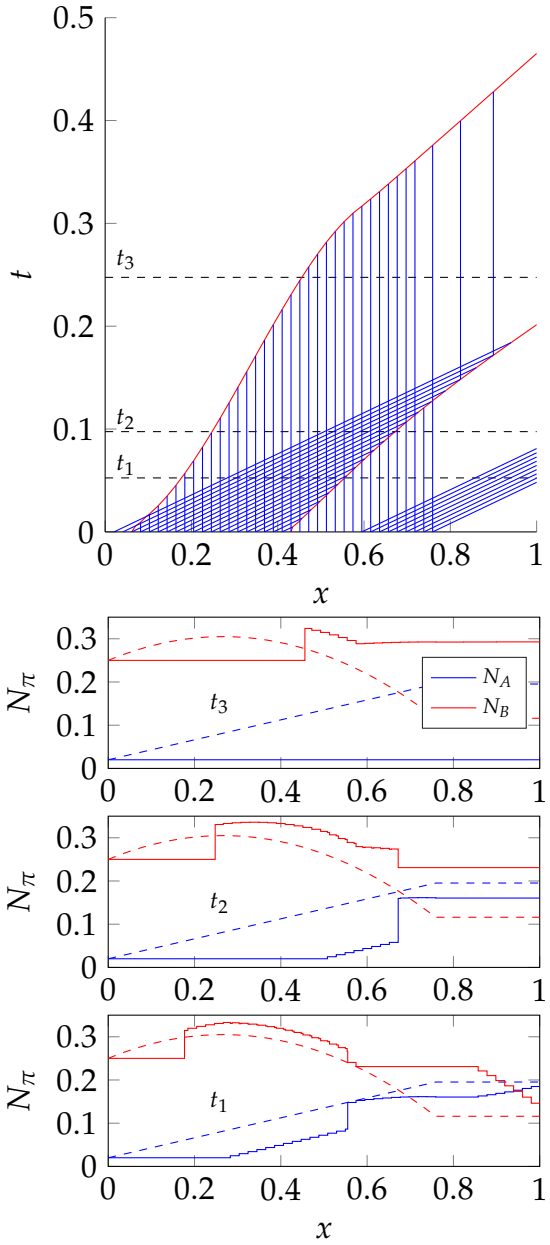

Figure 4.6: Interaction of solution waves for several initial discontinuities. The red lines on the top figure are characteristics for shocks and blue lines represents contact discontinuities. Three screen-shots of the solution at indicated times by dashed line in the top figure are depicted on the other figures. The initial condition is illustrated by coloured dashed curves. The jagged quality of the solid lines correpsonds to the number of step functions used in approximation of initial condition (dashed).

In this section, we present the results of two simulations of injection of unsaturated fluid to dissolve two salts with different solubility product in a 1/4-five-spot-pattern. More specifically, we take $k_A = 1\frac{\text{mol}^2}{\text{lit}^2}$ and $k_B = 2\frac{\text{mol}^2}{\text{lit}^2}$, c.f. Figure 4.1, with constant concentration of species for injection fluid $\boldsymbol{N}_l = \binom{0.05}{0.05}$. The boundary conditions for the pressure equation for both cases are similar (constant pressure at the producer with a source term of 1 pore volume of fluid per unit time injected at the injection well). The two simulations are different in that the first is in a homogeneous medium whereas the second is for a heterogeneous rock. For both cases, the domain dimensions are 366×671 and the simulation time is set to 6 pore volumes. For the homogeneous case, the grid dimensions are 120×220.

Figure 4.7 shows the propagation of injection fluid and the evolution of dissolution fronts in a homogeneous medium with constant porosity 0.2 and permeability 100 millidarcy using 120 streamlines. The initial condition of the medium is $\binom{0.4}{0.3}$. The one-dimensional version of this problem is explained in Case 14 of Section 4.3.1. As illustrated in Figure 4.3a and explained in Section 4.3.1, the intermediate state $\boldsymbol{N}_i$ has a higher concentration of N_A. The reason is that the faster shock $\mathcal{S}_2$ dissolves salt B and salt A starts to precipitate due to the co-ion effect. In the two-dimensional case of this problem, the streamlines mix at the well resulting in even more precipitate of A. These precipitate do not leave the system until an unsaturated mixture arrives and dissolves the precipitates. In fact, if the arriving streamlines are not saturated and they have different compositions, they may induce more precipitates.

The accumulation of precipitates at the well through the mixing of streamlines is best illustrated in the plane spanned by the secondary variables n_A and n_B. Figure 4.8 shows an example. The values of n_A and n_B are bounded by zeros (horizontal and vertical axes) and the projection of B^{AU} and A^{BU} from the hodograph plane into this plane. The concentration of the components for any fluid ($\boldsymbol{n}$) can be represented by a point in this domain including its boundaries. Now consider, for example, the streamlines 1 and 5 in Figure 4.7 after 1.5 pore volumes have been injected. Streamline 1 at the well is saturated with both components and the concentration of the components is $(\hat{n}_A, \hat{n}_B)^T$. Along streamline 5, the fluid is unsaturated with B but saturated with A. The two fluid concentrations are illustrated in the n_A-n_B plane. The domain is not convex and therefore any linear combination of $\boldsymbol{n}_1$ and $\boldsymbol{n}_5$ is outside the domain and implies an oversaturated fluid. As a result, more precipitates are produced and the precipitates accumulate and potentially clog the well. In a finite-volume based simulation, precipitates are distributed over the whole cells containing the well due to the

numerical dispersion. This yields an underestimate of the amount of precipitate at the well. Figure 4.9 shows the produced water and the amount of accumulated precipitate at the production well.

As an example with heterogeneous porosity, we take the 20th layer of the SPE10 model from [99] (c.f. Figure 4.10). As discussed in Section 4.3.2, the discontinuity in porosity causes the flux function to be discontinuous and thus the solution to the Riemann Problem may involve an additional constant state. For the initial condition, we set the fluid concentration of species (n_α) equal for all blocks to establish an initial chemical equilibrium. The amount of initial precipitate for each block is set to be proportional to the porosity of that block. Hence, a cell with more void space would accommodate more precipitates initially. Figure 4.11 illustrates the propagation of the fronts (n_π) in the whole domain at three times using 380 streamlines in 60×220 grid cells. Figure 4.12 shows produced water at the production well.

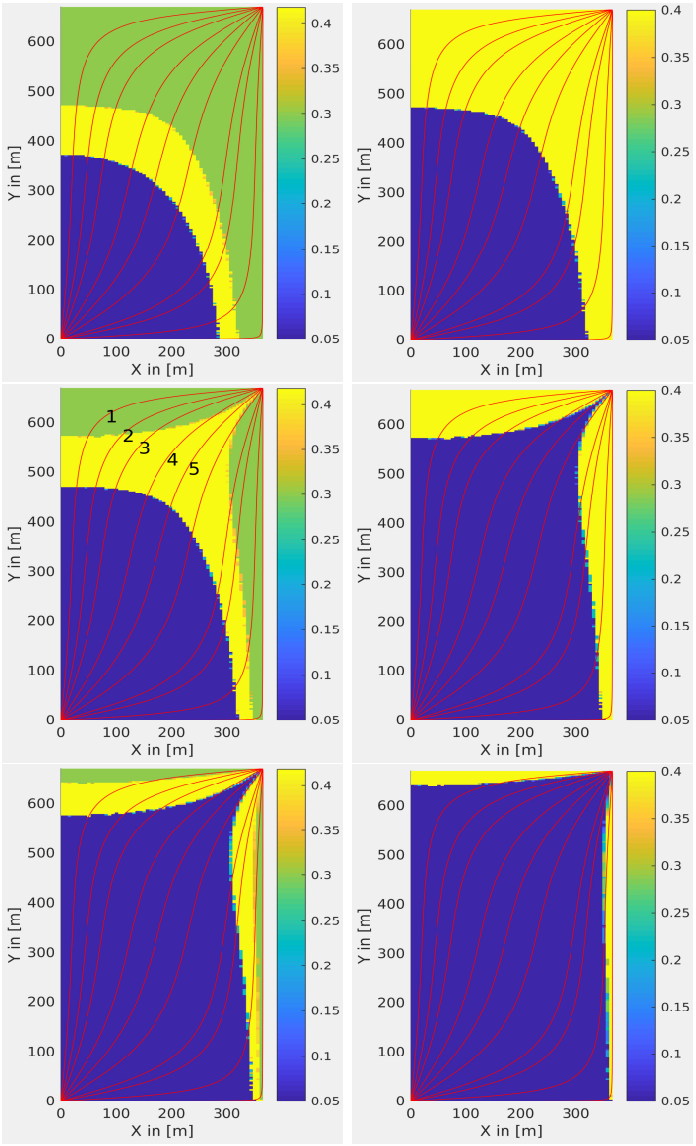

Figure 4.7: Evolution of fronts of N_A (left column) and N_B (right column) in a two-dimensional homogeneous medium for injection of an unsaturated water to dissolve two salts (problem of Figure 4.5 with $\phi_l = \phi_r = 0.2$) in three different instances of time (in pore volumes); 1.0 (top) , 1.5 (middle) and 2.3 (bottom). Some of the streamlines are depicted for visualisations. The colorbar depicts the concentration of components.

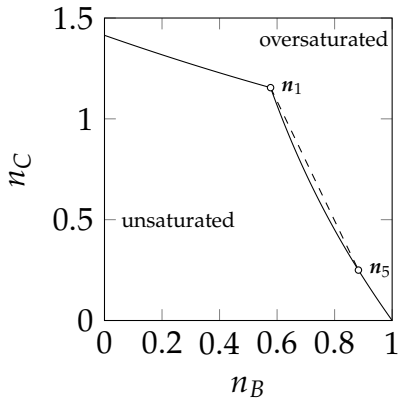

Figure 4.8: The n_A-n_B plane constructed by projecting the two boundaries A^{BU} and B^{AU} from the hodograph plane. Point $\boldsymbol{n}_1$ and $\boldsymbol{n}_5$ correspond to the streamlines 1 and 5 of Figure 4.7. somewhere on the dashed line that is supersaturated and results in producing precipitates. For a better illustration of non-convexity of unsaturated zone equilibrium constants are set to $k_A = 1$, $k_B = 10$.

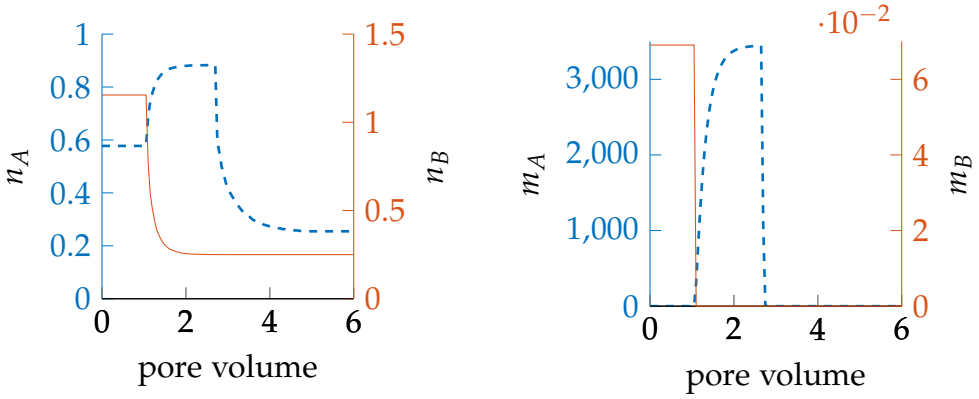

Figure 4.9: a) History of the concentration of the sampled water (dashed for n_A and solid for n_B) for homogeneous medium ($\phi = 0.2$). b) History of precipitate of A, m_A (dashed blue) and precipitate B, m_B (solid red) at well in mole/volume with $V_w = 0.1$. As soon as B is dissolved, due to the co-ion effect, precipitate A starts to accumulate and reaches a maximum dependent to V_w before it dissolves.

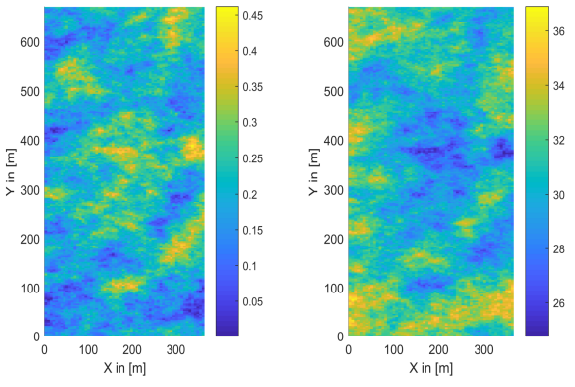

Figure 4.10: a) Porosity and b) permeability field ($-log(K)$)) of 20th layer of SPE10 model from MRST [100]

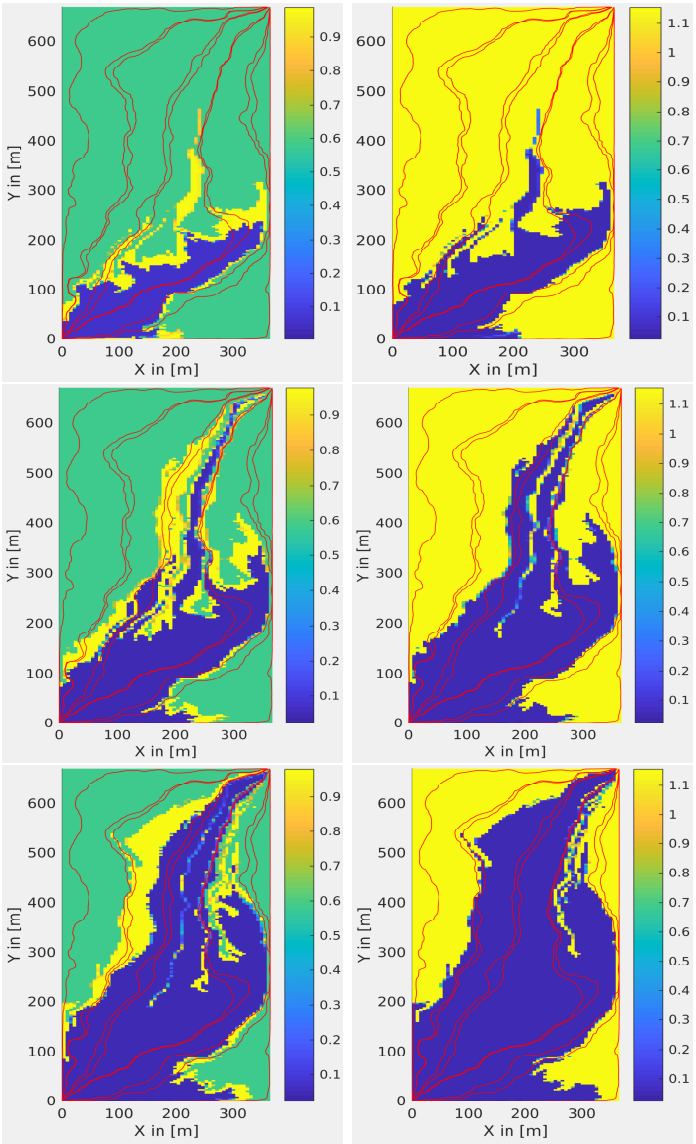

Figure 4.11: Evolution of fronts of n_A (left column) and n_B (right column) in a two-dimensional heterogeneous medium for injection of an unsaturated solution to dissolve two salts in three different instances of time (in pore volumes); 1.2 (top) , 2.4 (middle) and 4.8 (bottom). The colorbar shows the concentration of components.

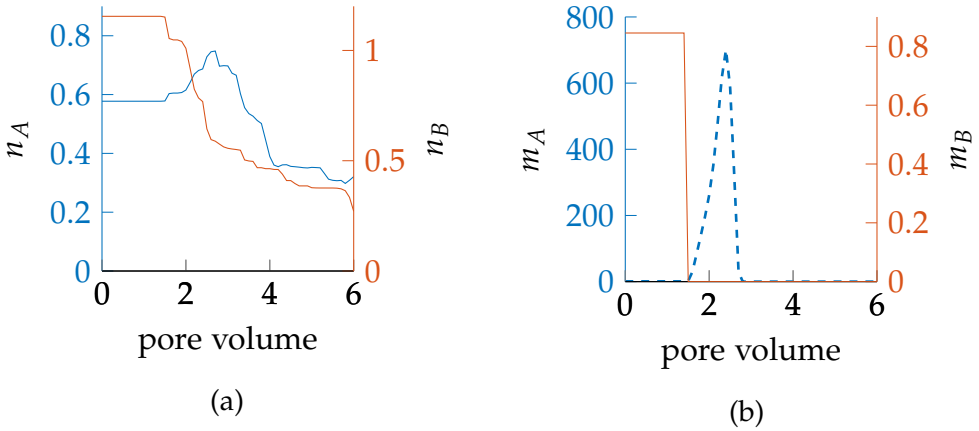

Figure 4.12: a) History of the concentration of the sampled water (mole/volume) for the heterogeneous case, b) history of precipitate of A, m_A (dashed blue) and B, m_B (solid red) at well in mole/volume with $V_w = 0.1$.

We have presented a streamline method for flow in porous media involving two chemical reactions. The two reactions share an ion and thus the common-ion effect determines the saturated concentration levels. The method is based on a front-tracking algorithm that uses the analytical solutions to Riemann Problems along each streamline. To apply the method for a heterogeneous medium, the analytical solution in one dimension is extended to take into account discontinuities of the flux function for the underlying hyperbolic PDE. The unique entropy satisfying solution for the hyperbolic system is sought through honouring conservation of mass across the interface and the monotonic increase of wave speeds.

To predict scaling at the well, a model for mixing streamlines at the well is provided. The well model post-processes the results from streamline simulator. Through this model, we have shown how streamlines with different concentrations arriving at different times result in high accumulation of precipitates at the well. The results can be used in prediction of breakthrough of concentrations when chemical reactions in the reservoir do not change porosity or permeability of the medium significantly.

While this method is free from the excessive dispersion typical in finite volumes and does not a Newton solver at each step, and hence quite efficient for large domains, it has the restrictions on the physics it can accommodate. In general, chemical reactions are assumed to be in equilibrium at all times, medium and the fluid is assumed to be incompressible and other physics such as capillary, gravity and changes in permeability are ignored for the sake simplicity. In general, when the number of physical processes increase streamline methods start to loose their advantage over standard finite volume methods.

5

PRECIPITATION AND DISSOLUTION IN FRACTURE NETWORKS

In this chapter, we aim to develop a simulation strategy for dissolution and precipitation in discrete fracture networks in two dimensions. We first consider a simple network of two fractures that form a self-mixing problem. We show that this system is prone to clogging in dissolving two salts via unsaturated injection fluid. In addition, we consider the transport of two different unsaturated fluid and indicate that these type of systems can also clog themselves. The systems are studied under several simplifying assumption and factors affecting clogging are analysed. The topology of the network is then expanded, the assumptions taken are relaxed and the algorithm is explained through an illustrative example.

5.1 MODEL

The chemical reactions are the ones used discussed previously, i. e., Equation (2.1) on page 7. For this chapter, we take the values relevant to the reactions of potassium chloride and sodium chloride, $k_A = 7.9\frac{\text{mol}^2}{\text{lit}^2}$, $k_B = 37.2\frac{\text{mol}^2}{\text{lit}^2}$. The shared ion is chloride (Cl^-). Other assumptions taken include incompressibility of the fluid and medium, constant temperature and negligible mechanical dispersion and molecular diffusion.

5.1.1 *Transport*

We consider the self-mixing problem containing two fractures 1 and 2 (also referred to as paths 1 and 2) that intersect at two locations. Both paths diverge from the inlet and converge to the outlet and have a fixed boundary condition (inlet composition $\boldsymbol{N}_I$) as depicted in Figure 5.1 with K, L and d as permeability, length and aperture for each fracture, respectively. The system initially has a uniform overall composition of $\boldsymbol{N}_r$ everywhere.

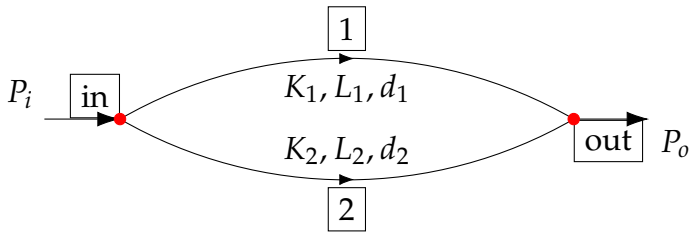

Figure 5.1: Sketch of a system with self-mixing paths. K, L and d are permeability, length and aperture, respectively.

Each path is considered as a one-dimensional domain. The mass balance along each path reads

$$\frac{\partial \boldsymbol{N}}{\partial t} + \frac{\partial \left(v\boldsymbol{n}\right)}{\partial x} = 0, \quad x \in [0, L], \quad t > 0, \tag{5.1}$$

with $L = L_1$ for path 1 and $L = L_2$ for path 2. In Equation (5.1), v is the velocity of fluid along the path. The porosity of the fractures are unity. Therefore, the overall concentration of a component i is given by

$$N_i = n_i + m_i. \tag{5.2}$$

For the current problem, we neglect the contribution of precipitates to the void volume along the fractures because the volume fraction of precipitate is usually less than 10^{-3} in those areas[1]. At the intersections, however, precipitates accumulate and their contribution to flow needs to be accounted for. Hence, precipitation or dissolution along the fracture does not have any effect on the velocity of the fluid. The solution to the Riemann Problem of Equation (5.1) is given in [1] and was summarised in Chapter 4.

For the first example, we consider the dissolution of two salts, which are initially present in the whole network, by an unsaturated fluid. In particular, we take $\boldsymbol{N}_l = \binom{1.5}{1.5}$ and $\boldsymbol{N}_r = \binom{1.3}{6.0}$. The Riemann solution consists of two shocks. The initial condition, Hugoniot loci and the intermediate state are depicted in Figure 5.2. The two shocks on path j are denoted by $\hat{\mathcal{S}}_1^{(j)}$ and $\hat{\mathcal{S}}_2^{(j)}$ for slow and fast shock in path j, respectively. Hence, the velocity of $\hat{\mathcal{S}}_1^{(j)}$ is smaller than that of $\hat{\mathcal{S}}_2^{(j)}$ for $j = 1, 2$. The absolute shock velocities are both smaller than the fluid velocity and can be normalised by it, to yield the relative relative shock velocities $\mathcal{S}_1$ and $\mathcal{S}_2$,

$$\begin{pmatrix} \hat{\mathcal{S}}_1^{(j)} \\ \hat{\mathcal{S}}_2^{(j)} \end{pmatrix} = v_j \begin{pmatrix} \mathcal{S}_1 \\ \mathcal{S}_2 \end{pmatrix}, \tag{5.3}$$

1 Consider, for example, the precipitation of the most common scale, barium sulphate. The highest concentration for barium ion reported is 4000 ppm. This results in 6.8 moles of $BaSO_4$ (given enough of sulphate is present). Hence, around 1 cm^3 in a litre of solution.

The relative shock velocities therefore lie in the interval $[0, 1]$.

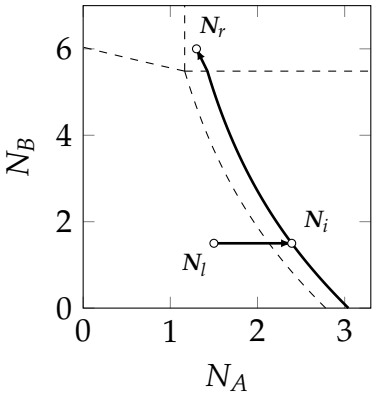

Figure 5.2: The solution in the hodograph plane for dissolution of two salts with unsaturated fluid. The two thick curves represent the Hugoniot loci from injected ($\boldsymbol{N}_l$) and ($\boldsymbol{N}_r$) initial fluid and their intersection is the intermediate state ($\boldsymbol{N}_i$) that appears between the two shock waves

5.1.2 *Flow*

Given a fixed pressure gradient $\Delta P = P_i - P_o$, we obtain the following relationships for the volumetric flow for each path

$$Q_1 = \Delta P \frac{d_1 K_1}{\mu L_1}, \qquad Q_2 = \Delta P \frac{d_2 K_2}{\mu L_2}, \tag{5.4}$$

where μ is the viscosity of the fluid and the fractions are the transmissibility associated with paths. Equation (5.4) can be expanded, using the cubic law for the permeability (see [101]) of the fractures, to obtain

$$Q_1 = \frac{\Delta P d_1^3}{12 \mu L_1}, \qquad Q_2 = \frac{\Delta P d_2^3}{12 \mu L_2}. \tag{5.5}$$

5.1.3 *Mixing*

There is only one location for mixing in this problem, i. e., the intersection of paths 1 and 2 at the outlet. Initially ($t = t_0$), the concentration at the intersection, which is denoted by $\boldsymbol{N}_\xi$, is $\boldsymbol{N}_r$,

$$\boldsymbol{N}_\xi \Big|_{t_0} = \boldsymbol{N}_r. \tag{5.6}$$

The two shocks from the two paths 1 and 2 arrive to the intersection point at four (possibly) different times $t_s^{(1)}$, $t_f^{(1)}$, $t_s^{(2)}$ and $t_f^{(2)}$. Here, we have used the subscripts s and f for arrival of 1-shock and 2-shock family (slow and fast) to avoid confusion with the path number in superscripts. The volume of the intersection of paths

is determined by apertures d_1 and d_2 and the angle between the normals θ, therefore

$$\tilde{V} := d_1 d_2 \csc(\theta) \tag{5.7}$$

Equation (5.7) may be multiplied by the porosity to obtain the void volume for the intersection. Note that at the intersection, we do not neglect the contribution of precipitates to the volume because precipitates accumulate at the intersection volumes. Initially at $t = t_0$, the intersection is partially filled with A and B precipitates with moles per volume of the medium $m_A^{\xi}\Big|_{t_0}$ and $m_B^{\xi}\Big|_{t_0}$. The volume of salts in the intersection prior to any mixing, $V_{A\text{rem}}$ and $V_{B\text{rem}}$, is thus

$$V_{A\text{rem}} := \frac{m_A^{\xi}\Big|_{t_0} \tilde{V}}{\omega_A}, \qquad V_{B\text{rem}} := \frac{m_B^{\xi}\Big|_{t_0} \tilde{V}}{\omega_B}, \tag{5.8}$$

where ω_A and ω_B are the molar densities.

For the outlet, it is assumed that the incoming streams completely mix, i. e., they reach equilibrium upon arrival and before leaving the sytem. The time interval after which mixing of incoming streams with any stationary precipitates is calculated, is referred to as the *mixing time* and is denoted by δt. A natural selection for the mixing time is one that allows the intersection volume to be filled with the incoming streams. The mixing time must be less than or equal to the time needed to fill the intersection at the outlet, t_i, because otherwise mixing is incomplete. Therefore, the maximum value for δt is defined by

$$t_i := \frac{V_{\text{eff}}}{(Q_1 + Q_2)}, \tag{5.9}$$

where V_{eff} is the effective volume of the intersection,

$$V_{\text{eff}} = \phi \tilde{V} - V_{A\text{rem}} - V_{B\text{rem}}. \tag{5.10}$$

The last equation is expanded using Equation (5.8) to obtain the following expression

$$V_{\text{eff}} = \tilde{V} \left(\phi - \frac{m_A^r}{\omega_A} - \frac{m_B^r}{\omega_B} \right), \tag{5.11}$$

from which we define the effective porosity, ϕ_F,

$$\phi_F := \frac{V_{\text{eff}}}{\tilde{V}} = \phi - \phi_A \left(N_A^r, N_B^r \right) - \phi_B \left(N_A^r, N_B^r \right) \tag{5.12}$$

where ϕ_A and ϕ_B are the volume fraction of salt A and B when they contribute to changes of volume. The three volume fractions ϕ_A, ϕ_B and ϕ_F are functions of primary variable $\boldsymbol{N}$. They were introduced in Chapter 3 and their explicit expression are given in Appendix A.1.

We shall now evaluate the concentration, amount of precipitates and the porosity of the intersection after the finite mixing time δt. The overall concentration (for A) after a mixing timestep from beginning of the process, t_0, is

$$N_A^{\xi}\Big|_{t_0+\delta t} = \frac{\mathcal{N}_{A,1} + \mathcal{N}_{A,2} + \tilde{\mathcal{N}}_A + m_A^{\xi}\tilde{V}}{\tilde{V}}, \tag{5.13}$$

where $m_A^{\xi}\tilde{V}$ represents the precipitates (of salt A) that are immobile in moles and are present when the incoming fluid enter the intersection point. The notations $\mathcal{N}_{A,1}$ and $\mathcal{N}_{A,2}$ in Equation (5.13) are the number of moles of A that flow from path 1 and 2, respectively. The number of incoming moles of A after δt on path 1 is

$$\mathcal{N}_{A,1} = Q_1 n_A^1 \delta t, \tag{5.14}$$

where n_A^1 is the concentration of A in path 1 that reaches the outlet. The term $\tilde{\mathcal{N}}_A$ in Equation (5.13) represents the moles of A in the fluid that remained in the intersection from time t_0 and will be mixed with the streams from path 1 and 2. Assuming $\delta t \leq t_i$, the portion of the intersection effective volume, which is occupied by incoming fluid, is $\frac{\delta t}{t_i}$. Therefore, $\tilde{\mathcal{N}}_A$ is calculated as

$$\tilde{\mathcal{N}}_A = \left(1 - \frac{\delta t}{t_i}\right) n_A\Big|_{t_0} \tilde{V}\phi_F\Big|_{t_0}, \tag{5.15}$$

where n_A and ϕ_F are evaluated at $\boldsymbol{N}_m\Big|_{t_0}$. Replacing the last two equations in Equation (5.13), we obtain the overall concentration for the intersection after δt,

$$N_A^m\Big|_{t_0+\delta t} = \left(\bar{n}_A \frac{\delta t}{t_i} + n_A\Big|_{t_0} \frac{t_i - \delta t}{t_i}\right)\phi_F + m_A\Big|_{t_0}, \tag{5.16a}$$

$$N_B^m\Big|_{t_0+\delta t} = \left(\bar{n}_B \frac{\delta t}{t_i} + n_B\Big|_{t_0} \frac{t_i - \delta t}{t_i}\right)\phi_F + m_B\Big|_{t_0}. \tag{5.16b}$$

where $n_A\Big|_{t_0}$ is the function n_A evaluated at $\boldsymbol{N}_m\Big|_{t_0}$ and

$$\bar{n}_\pi = \frac{Q_1 n_\pi^1 + Q_2 n_\pi^2}{Q_1 + Q_2}, \quad \pi = \{A, B\} \tag{5.17}$$

and refers to mobile ions of π entering the intersection. For a more accurate estimation of $\boldsymbol{N}_m\Big|_{t_0+\delta t}$, we use functions ϕ_A and ϕ_B to evaluate the amount of precipitate at the intersection and replace $N_\pi^m\Big|_{t_0+\delta t}$ in Equation (5.16) to obtain

$$N_\pi^m\Big|_{t_0+\delta t} = \left[\left(\bar{n}_\pi \frac{\delta t}{t_i} + n_\pi \frac{t_i - \delta t}{t_i}\right)\phi_F + \omega_\pi \phi_\pi\right]_{t_0}. \tag{5.18}$$

where n_A, n_B, ϕ_A, ϕ_B and ϕ_F are all evaluated at $\boldsymbol{N}_m\Big|_{t_0}$. We can express $\boldsymbol{N}_m\Big|_{t_0}$ as

$$N_\pi^m\Big|_{t_0} = \left[n_\pi \phi_F + \omega_\pi \phi_\pi\right]_{t_0}. \tag{5.19}$$

Subtracting the Equation (5.19) from Equation (5.18) yields, after simplification,

$$N_\pi^m\Big|_{t_0+\delta t} - N_\pi^m\Big|_{t_0} = \delta N_\pi^m = \frac{\delta t}{t_i}\left(\bar{n}_\pi - n_\pi\right)\phi_F, \tag{5.20}$$

which holds true at all times $t > t_0$. Therefore, we have dropped the index zero and shown the difference by δN_π^m. Dividing the above equation by the mixing time, letting $\delta t \to 0$ and using the definition of t_i from Equation (5.9), we obtain the system of ODEs for evolution of the overall concentration in the intersection

$$\frac{\mathrm{d}N_A}{\mathrm{d}t} = \frac{Q_1 + Q_2}{\tilde{V}}\left(\bar{n}_A - n_A(N_A, N_B)\right), \tag{5.21a}$$

$$\frac{\mathrm{d}N_B}{\mathrm{d}t} = \frac{Q_1 + Q_2}{\tilde{V}}\left(\bar{n}_B - n_B(N_A, N_B)\right). \tag{5.21b}$$

In Equation (5.18), the sum of the incoming mobile ions $(\bar{n}_A, \bar{n}_B)$ may exceed the saturation value. Therefore, the mixture of the incoming fluid is over-saturated and the surplus will precipitate. This precipitation will result in accumulation of salts at the intersection. Initially, the profile of $\boldsymbol{N}$ has identical values for path 1 at L_1 and for path 2 at L_2. This situation holds true until a fast shock arrives at the intersection. It can be assumed, without the loss of generality, that arrival of the faster shock in path 1, $t_f^{(1)}$, is earlier than that of path 2, $t_f^{(2)}$. For $t > t_f^{(1)}$ the incoming fluid from path 1 has concentration $\begin{pmatrix} n_A^i \\ n_B^i \end{pmatrix}$ while the concentration of mobile components that are carried to the intersection from path 2 are $\begin{pmatrix} n_A^r \\ n_B^r \end{pmatrix} = \begin{pmatrix} \hat{n}_A \\ \hat{n}_B \end{pmatrix}$. The concentration for these two streams are shown as two points in the hodograph plane in Figure 5.3a. The mixture lies somewhere on the line connecting these two points. This line always lies outside the unsaturated region because of the convexity of the curves in the hodograph plane. Hence, the mixture is over-saturated with respect to A and any additional ions must precipitate. The precipitation continues until a new shock arrives to the intersec-

tion, i. e., either the fast shock from path 2 or the slow shock from path 1. In the latter case, dissolution of salt A starts because saturated fluid $\begin{pmatrix} n_A^r \\ n_B^r \end{pmatrix}$ mixes with the unsaturated fluid $\begin{pmatrix} n_A^l \\ n_B^l \end{pmatrix}$ that lies in the unsaturated region, as depicted in Figure 5.3b. In the former case, two streams of same composition mix. Hence, no change in the amount of precipitates occur. The situation will remain unchanged until a slow shock reaches the intersection whereby dissolution of salt A happens.

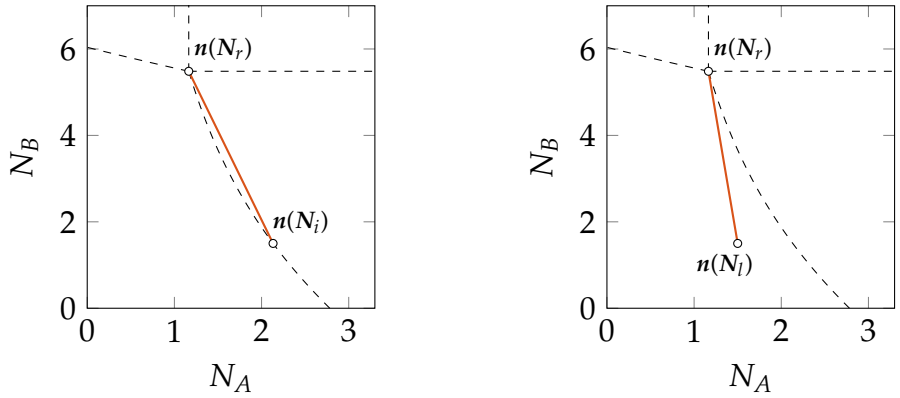

Figure 5.3: Concentration of components in the fluid for the two incoming streams at different time intervals a) when mixing results in accumulation of precipitates at the intersection and b) when mixing of incoming streams dissolves any present precipitate. The solid line represent the composition of all possible mixtures at the intersection.

5.1.4 *Precipitation*

Here, we seek to study the precipitation rate and calculate the amount of precipitate after it has been triggered, i. e., for $t > t_f^{(1)}$. We can do this by integrating Equation (5.21) and then evaluating the precipitates using the expression in Appendix A.1. However, it should be noted that inflow concentrations $\bar{n}_\pi$ are also functions of flow rates. On the other hand, the flow rates are functions of the permeability of the intersection which is again a function of $N_{\tilde{\xi}}$. Hence, Equation (5.21) is highly nonlinear and numerical methods must be employed to obtain the solution. However, we assume here that the flow is not altered by the precipitation at the intersection. Also, we assume the precipitation rate is constant after it has been triggered (i. e., at $t = t_0$) until it changes to zero or negative (dissolution stage). Another assumption is that t_i is so small that $\delta t = t_i$ is a good approximation in estimating the derivatives. These assumptions are valid at high flow rates (c.f. the defition of t_i in Equation (5.9)) and for highly

dense salts. Hence, the following approximations for rate of precipitation and dissolution are obtained

$$\frac{\mathrm{d}m_A}{\mathrm{d}t} \approx \left(\frac{Q_1+Q_2}{\tilde{V}\phi_F}\omega_A\right)\Big[\phi_A(\bar{n}_A\phi_F+\omega_A\phi_A,\bar{n}_B\phi_F+\omega_B\phi_B)-\phi_A\Big], \tag{5.22a}$$

$$\frac{\mathrm{d}m_B}{\mathrm{d}t} \approx \left(\frac{Q_1+Q_2}{\tilde{V}\phi_F}\omega_B\right)\Big[\phi_B(\bar{n}_A\phi_F+\omega_A\phi_A,\bar{n}_B\phi_F+\omega_B\phi_B)-\phi_B\Big], \tag{5.22b}$$

respectively. The constraints for the above equations are

$$\frac{\mathrm{d}m_A}{\mathrm{d}t} = 0, \quad \text{for } \phi_A = 1, \tag{5.23a}$$

$$\frac{\mathrm{d}m_B}{\mathrm{d}t} = 0, \quad \text{for } \phi_B = 0. \tag{5.23b}$$

i. e., complete dissolution of precipitate B or clogged intersection by salt A.

In derivation of Equation (5.22), we have assumed the incoming streams have constant concentration. Therefore, the bounds of integral are the time interval between arrival of different shocks. With the assumption of constant flow conditions, the time-of-flights are calculated using $t = \frac{L}{v}$. As before, we assume the fast shock along path 1 has the earliest arrival at the intersection. The expression for this time-of-flight, $t_f^{(1)}$, is

$$t_f^{(1)} = \frac{12\phi\mu L_1^2}{\mathcal{S}_2\Delta P d_1^2} \tag{5.24}$$

The next front arriving at the intersection is either the slow shock from path 1 (at $t = t_s^{(1)}$) or the fast one from path 2 (at $t = t_f^{(2)}$). In either case, we have accumulation of precipitate A whilst dissolution of salt B for $t \in [t_f^{(1)}, t^*]$ where

$$t^* = \min(t_s^{(1)}, t_f^{(2)}) \tag{5.25}$$

If $t^* = t_s^{(1)}$, dissolution of salt A initiates at $t = t^*$ and continues until all the salts are being dissolved. For $t = t_f^{(2)}$, no dissolution occurs in the interval $t \in [t^*, t^\dagger]$, where

$$t^\dagger = \min(t_s^{(2)}, t_s^{(1)}). \tag{5.26}$$

The dissolution of salt A initiates at $t = t^\dagger$.

From the above analysis, we conclude that the amount of precipitate is directly proportional to the difference $t_p := t^* - t_f^{(1)}$ and we refer to it as the *precipitation time*. If $t^* = t_f^{(2)}$, we obtain

$$t_p = \frac{12\phi\mu}{\mathcal{S}_2 \Delta P} \left(\frac{L_2^2}{d_2^2} - \frac{L_1^2}{d_1^2} \right). \tag{5.27a}$$

For the second case where $t^* = t_s^{(1)}$, the expression for the precipitation time reads

$$t_p = \frac{12\phi\mu L_1^2}{d_1^2 \Delta P} \left(\frac{1}{\mathcal{S}_1} - \frac{1}{\mathcal{S}_2} \right). \tag{5.27b}$$

Assuming a constant rate of precipitation, Equation (5.22) can now be integrated for the precipitation time period to obtain the maximum amount of precipitate that forms in the intersection, m_A^∞ and m_B^∞, as

$$m_A^\infty = t_p \left(\frac{\mathrm{d}m_A}{\mathrm{d}t} \right) + m_A^r, \qquad m_B^\infty = t_p \left(\frac{\mathrm{d}m_B}{\mathrm{d}t} \right) + m_B^r. \tag{5.28}$$

5.2 SENTIVITY ANALYSIS FOR PRECIPITATION AT THE INTERSECTION

This section provides a sensitivity analysis on precipitation rate and time in terms of geometrical parameters and the initial conditions. The velocities depend on the geometrical parameters of the fracture network. These parameters, as well as the initial condition, affect both the precipitation time and the precipitation/dissolution rates. The values for the base case are $d_1 = 1.1$mm, $d_2 = 1$mm, $L_1 = 50$m, $L_2 = 51$m, $\boldsymbol{N}_l = \binom{1,8}{2}$ and $\boldsymbol{N}_r = \binom{1,3}{6}$, unless stated otherwise. The pressure difference is set to 1 atmosphere and the flow is calculated from the given aperture and length of each path.

5.2.1 *Geometry*

In this section, we focus on the effect of variation of length and aperture of fractures on the maximum amount of precipitates. There are a total of four parameters, d_1, d_2, L_1 and L_2 to be considered. However, we only focus on the effect of variation of length and aperture for path 1 due to the symmetry of the topology.

The effect of length and aperture are reflected on both precipitation time and rate of precipitation. Consider the case where t_p is calculated from Equation (5.27a), (e. g., when $d_1 = d_2$ and $L_1 < L_2$). Here, we increase d_1 to keep our assumption that path 1 is faster than path 2. Figure 5.4a shows the vari-

ation of precipitation time with respect to changes in the aperture in terms of normalised quantities. Equation (5.27a) shows that an increase in d_1 causes an increase in precipitation time. This growing trend of precipitation time continues until $t_s^{(1)} = t_f^{(2)}$. Further increase in d_1 results in a decrease in precipitation time because now $t^* = t_f^{(2)}$ and precipitation time is calculated from Equation (5.27b).

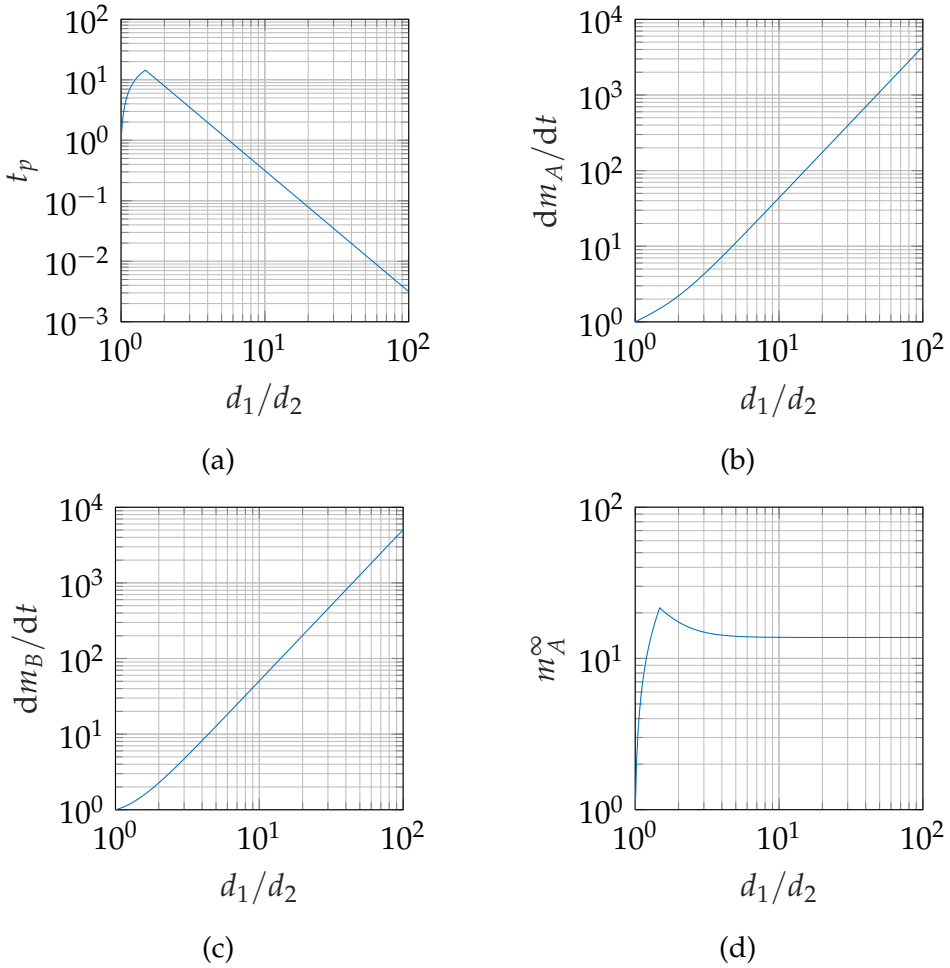

Figure 5.4: Variation of precipitation rates (a), dissolution rates (b), precipitation time (c) and final amount of precipitates (d) versus changes in ratio of the aperture of the fractures. The quantities on both axes are normalised by their initial value, i. e., values at $d_1 = d_2$. Note that the dissolution rates are negative.

Next, we consider the effect of aperture on the precipitation/dissolution rate. The plots for variations of normalised quantities are shown in Figures 5.4b and 5.4c. The inverse precipitation rate is roughly proportional to the square of aperture because the flow is scaled by d_1^3 and hence $\delta t \propto d_1^{-2}$. The changes of δt overcompensate any changes in dm and hence the precipitation rate increases by an increase in the aperture of fracture 1.

In Figure 5.5, the effect of changes of L_1 on the precipitation/dissolution parameters are illustrated. Here, the apertures and the length of the second path (L_2) are fixed at $d_1 = 1.1$mm, $d_2 = 1.0$mm and $L_2 = 51$m. The length of the first path (L_1) is decreased up to two orders of magnitude. The changes in the precipita-

tion time, illustrated in Figure 5.5a, can be justified using a similar argument as before except that the effects are reversed. The changes in the precipitation/dissolution rates are shown in Figures 5.5b and 5.5c. The effect of changes of L_1 is also opposite to that of the aperture with respect to precipitation rate. However, the proportionality rate is less than 1. Therefore, the changes in the final amount of precipitate, as shown in Figure 5.5d, decreases with a decrease in the ration of $\frac{L_1}{L_2}$.

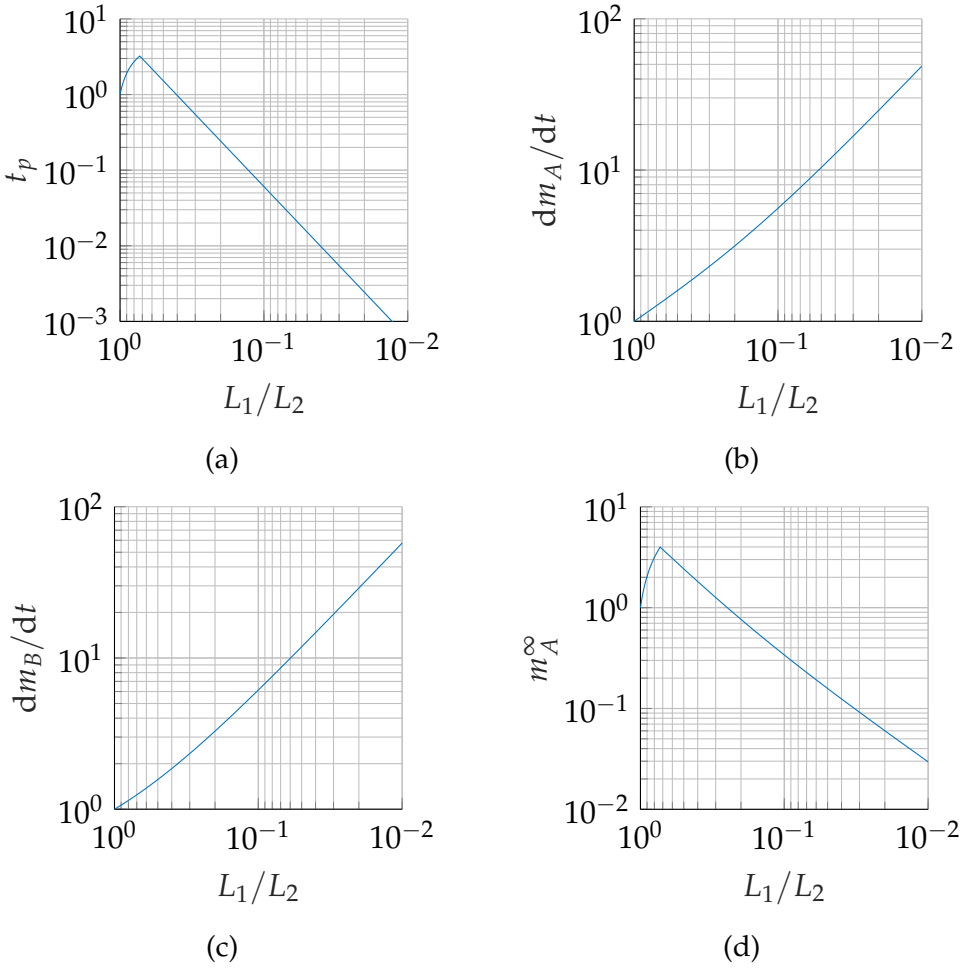

Figure 5.5: Variation of precipitation rates (a), dissolution rates (b), precipitation time (c) and final amount of precipitates (d) versus changes in ratio of the length of fractures. The quantities on both axes are normalised by their initial value, i. e., values at $L_1 = L_2$. Note that the dissolution rates are negative.

5.2.2 *Injection concentration and initial condition*

The effect of injection fluid on the final amount of precipitate is more complex than that of the geometry. An injection fluid, that has its overall concentration on the bifurcation line, induces zero amount of precipitates [1, 102] (or see Section 3.3.7 on page 33). The bifurcation line is the straight line that passes through $\boldsymbol{N}_r$ and the intersection of the boundary curves in the hodograph plane,

$\boldsymbol{N}_t = \begin{pmatrix} \hat{n}_A \\ \hat{n}_B \end{pmatrix}$. When $\boldsymbol{N}_r$ belongs to bifurcation line, the two shocks $\mathcal{S}_1$ and $\mathcal{S}_2$ gain the same velocity and merge, hence the intermediate state $\boldsymbol{N}_i$ disappears. It is thus expected that an increase in the distance of the injection fluid overall concentration,$\boldsymbol{N}_l$, from the bifurcation line increases the final amount of precipitate. This, however, does not imply a monotonic increase with respect to the distance from the bifurcation line. Away from this line and only on one side of it, the unsaturated region for the injection concentration can be divided into two regions based on the calculation of t_p, i. e., whether the precipitation time is calculated using Equation (5.27a) or Equation (5.27b). Figure 5.6 illustrates the contour lines for the final amount of precipitate based on the variation of $\boldsymbol{N}_l$ for both sides of the bifurcation line and the separating curves for each pair of regions. In both figures, the precipitation time for points in the regions, which are closer to the bifurcation line, is proportional to the difference of both shocks (c.f. Equation (5.27b)). In the other regions, which are away from the bifurcation line, only the fast shocks affect the precipitation time (c.f. Equation (5.27a)). Hence, contour lines are parallel to the main axis (or the Hugoniot loci) in these regions. The non-monotonicity in this region in Figure 5.6b is due to changes in precipitation rate for injection fluids that are nearly saturated which makes the mixture concentration over-saturated for both salts.

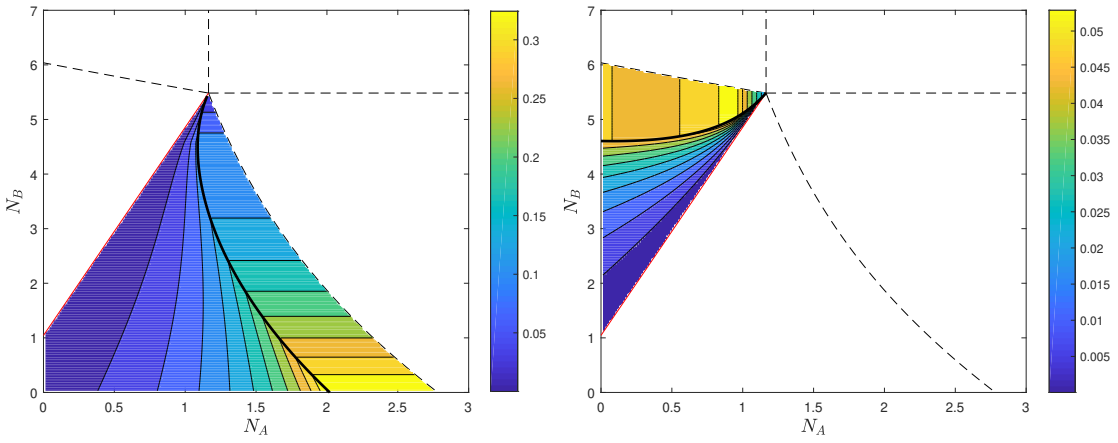

(a) (b)

Figure 5.6: Contour lines for the volume fraction of the final amount of precipitate for different upstream compositions in unsaturated region. The downstream composition is fixed to $\boldsymbol{N}_r = (1.3,\ 6)^T$. Contour lines for upstream points in either side of the bifurcation line (in red) are shown in two figures. (a) Volume ratio of the final amount of precipitate A. The highest amount of induced precipitate A is when the upstream does not contain B ions and but it is nearly saturated with respect to A. b) Volume fraction of the final amount of precipitate B. The final amount of precipitate riches its maximum when the upstream is relatively rich both ions. Colors show the volume fraction of precipitate A in (a) and B in (b).

The effect of variation of the initial condition, $\boldsymbol{N}_r$, on the final amount of precipitate is similar to that of injection concentration $\boldsymbol{N}_l$. Figure 5.7 illustrates these

effects for fixed injection concentration $\boldsymbol{N}_l = \binom{0.5}{5}$ and different values of initial condition, $\boldsymbol{N}_r$, in region $ASBS$. The final amount of precipitate is minimum if the bifurcation line from the initial condition passes over the concentration of the injection point on the hodograph plane. In other words, the line passing from the $\boldsymbol{N}_l$ and the triple point $\boldsymbol{N}_t$ is the bifurcation line. It should be noted again that in Figure 5.7, the lower triangle in the colored region represents the volume fraction of the final (maximum) amount of precipitate A before dissolution initiates at the intersectin. In this scenario, there is no precipitate B present. Likewise, in the complementary region of the colored area, contour lines show how much of the intersection is filled with salt B before its dissolution is triggered by the arrival of a new front. As illustrated in the figure, for certain values of the initial condition, the intersection is filled with precipitate B, i. e., the volume ratio reaches unity.

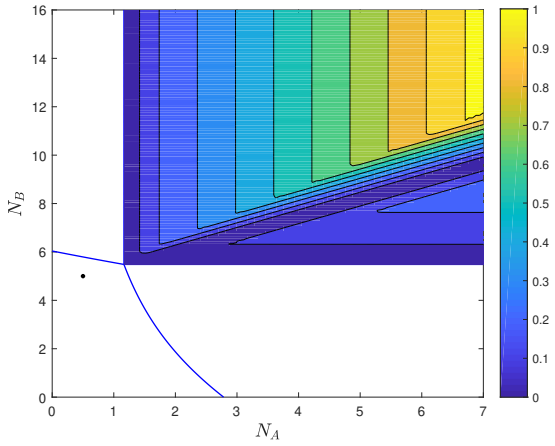

Figure 5.7: Contour lines for the volume fraction of the final amount of precipitate for different downstream compositions with different of amount of initial composition. The upstream composition is changed to $\boldsymbol{N}_l = (0.5, 5)^T$. Colors show the volume fraction of precipitates.

5.2.3 *Topology*

If the injection concentration on paths are different or the number of the paths change from 2 to a higher number, the precipitation time may be extended to several intervals. Consider for example that the paths 1 and 2 are fed from different inputs with overall concentration $\boldsymbol{N}_{l1}$ and $\boldsymbol{N}_{l2}$, respectively as illustrated in Figure 5.8. The injection concentrations, $\boldsymbol{N}_{l1}$ and $\boldsymbol{N}_{l2}$, are such that each one causes a distinct intermediate state, $\boldsymbol{N}_{i1}$ and $\boldsymbol{N}_{i2}$, in both regions as shown in Figure 5.9a. Again, assume that path 1 is faster and the first breakthrough at the intersection is the intermediate concentration corresponding to path 1, $\boldsymbol{N}_{i1}$. As before, the mixing concentration after the first breakthrough at $t_f^{(1)}$ is oversaturated (c.f. Figure 5.3a). Hence, the precipitation starts at $t = t_f^{(1)}$. Also assume

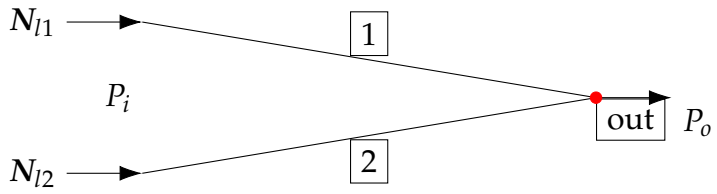

Figure 5.8: Sketch of a system with two fractures with different injection concentration (N_{l1} and N_{l2}). The pressure gradient is fixed to $\Delta P = P_o - P_i$.

the second breakthrough is at $t_f^{(2)}$, i. e., when the intermediate state from path 2 reaches the intersection. The important difference here from the previous case is that the precipitation may continue after $t = t_f^{(2)}$, because the new mixutre for $t \geq t_f^{(2)}$ may still be oversaturated. Figure 5.9b illustrates the concentration of the arriving flow streams after $t_f^{(2)}$ and the possible mixed concentration. As shown on the figure, part of the connecting lines is outside of the unsaturated zone. Therefore, the precipitation time may be extended for $t \geq t_f^{(2)}$ depending on the flow through each path. If the flow from path is considerably more than the one in path 2, the mixture of two paths is oversaturated. The precipitation finally stops when a slow shock reaches the intersection.

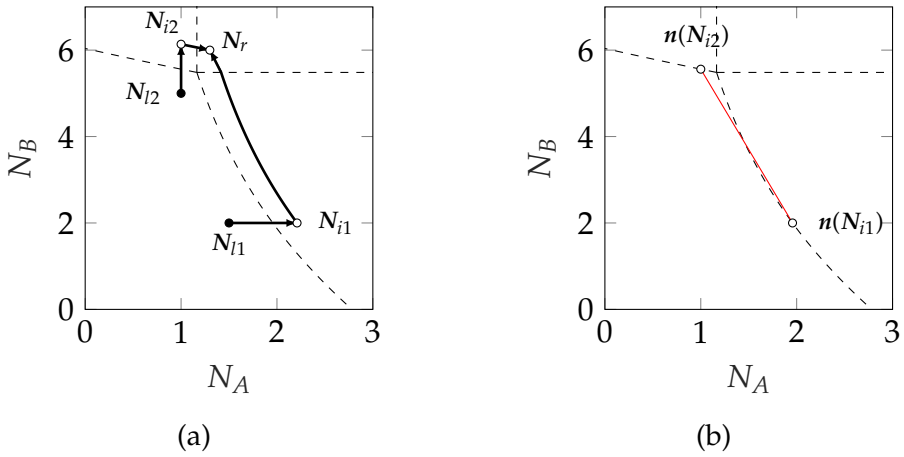

Figure 5.9: The solution on the hodograph plane when the two paths are fed with different (unsaturated) injection concentrations (a) and the possible mixing concentration for $t > t_f^{(2)}$. The assumption for the sequence of arrival of fronts are $t_f^{(1)} < t_f^{(2)}$.

The next example considered here is again for topology depicted in Figure 5.8 but now the injection fluid in both fractures are nearly saturated with respect A, i. e., their overall concentration is close to the boundary curve such that their mixture is saturated. Figure 5.10a depicts an example for such a case. Figure 5.10b shows that the mixture of the injection streams can be oversaturated for a range of Q_1 and Q_2. For such an injection concentration and flow rates, any combination of the upstream, downstream and intermediate state is oversaturated be-

cause the mixture of the unsaturated injection fluid streams is already saturated. Hence, precipitation keeps building up until the intersection is clogged.

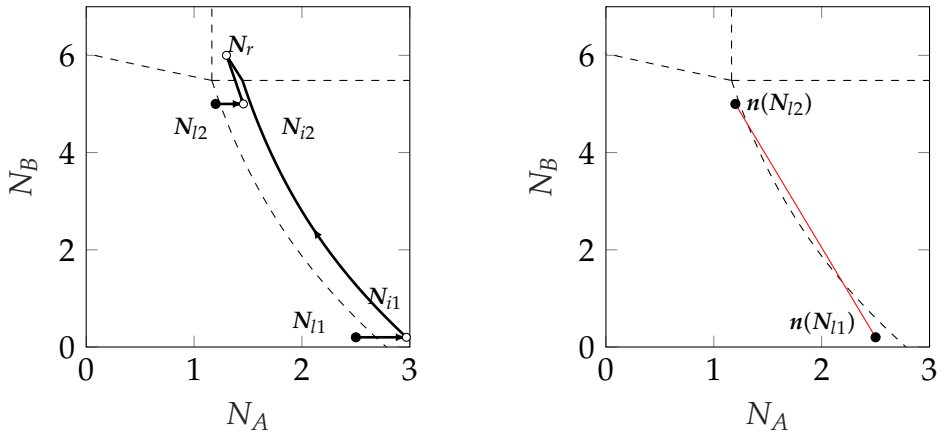

Figure 5.10: The solution on the hodograph plane when the two paths are fed with different nearly saturated injection concentrations (a) and the possible mixing concentration for injection fluids. Chances are higher that induced precipitation occurs with any combination of injection, initial or intermediate states

5.2.4 *Summary*

In the self-mixing setup (c.f. Figure 5.1), the sequence of events at an intersection is the accumulation of precipitates, dissolution of one salt followed by the dissolution of the other salt, provided that the precipitation stage does not clog the intersection. Each stage initiates with the arrival of a new front and terminates with the next front. The build-up of the precipitates is highly dependent on the ratio of the apertures and length of fractures as well as initial and injection concentrations, mostly in nonlinear form. The self-mixing can also form in larger networks as we will see in the next section. For the other minimal network that is not self-mixing, i. e., Figure 5.8, the situation is more complicated. Several precipitation stages may be present before dissolution initiates. Each stage may have a distinct rate of precipitation if linearisation is valid. However, the transition between stages occurs only when new fronts arrive at the mixer. We will discuss larger networks in the next section and discuss the cases where linearisation is not valid, i. e., when the changes of the volume at an intersection are drastic.

5.3 LARGE NETWORKS WITH MULTIPLE INTERSECTIONS

In the previous section, we showed that physical events are initiated by the arrival of fronts. A physical event may cause or change precipitation and/or dissolution rate at an intersection. The events occur due to the mixing of the incoming

streams and any stationary precipitate from the previous event. If the changes of precipitation or dissolution are not very high, one may assume rates and the flow in the whole network remain constant, as was the case in the previous section. In this section, we relax this assumption and extent the method for larger networks and several mixing points, i. e., intersections with two or more incoming streams. We will still use the four components explained in Section 5.1 between every two nodes but more is required to couple the flow and transport between several nodes. The algorithm is based on the solution to an assembly of Riemann Problems, i. e., a front-tracking algorithm, graph theory and the mixing model presented above. We will elaborate the algorithm for a network of six fractures that are either horizontal or vertical as depicted in Figure 5.11a and then provide another example with a larger network.

5.3.1 *Flow*

First, the fracture network needs to be mapped to an equivalent graph network, $\mathcal{G}$. In two-dimensional fracture network, fractures are represented as edges and the intersections are treated as nodes. Figures 5.11a and 5.11b depicts a network of 6 fractures and its equivalent graph representation, respectively. The distance between every two neighbouring nodes is 50 metres. The apertures for fractures 1 to 6 are 9, 1, 1, 10, 7 and 3 millimetres, respectively. The inlet and outlet pressure of the network is assumed to be constant, i. e., flow is allowed to change to reflect any changes of the permeability of the network.

We denote the aperture of a fracture by the letter d and indices for the bounding nodes. Here, we also assign the volume, a_j to each intersection j which is determined by the apertures of the intersecting fractures and the angle between their normals, θ, i. e., $a_j = d_{ij} d_{jk} \csc\theta$. Hence, each fracture ij has its length, L, trimmed by d_{jk} and d_{li} if the intersecting fractures on both ends are jk and li. The trimmed length is denoted by $\bar{L}$.

Through mass balance, we obtain

$$\sum_{j=1}^{N} Q_{ij} = 0, \tag{5.29}$$

for each node i, where Q_{ij} denotes the flux in each fracture between two nodes, i and j. Note that $Q_{ij} = 0$, if nodes i and j are not connected. We can also relate the flux in the fracture to the pressure at the nodes P_i and P_j using an equivalent Darcy's Law

$$v_{ij} = \frac{K_{ij}}{\mu L_{ij}} \left(P_i - P_j \right), \tag{5.30}$$

where

$$v_{ij} = Q_{ij}/d_{ij}. \tag{5.31}$$

In Equation (5.30), K_{ij} is the harmonic average of the permeabilities associated with part of the fracture that is bounded between two nodes, $\bar{K}_{ij}$, and the permeability of the two nodes, K_i and K_j, i. e.,

$$\frac{L_{ij}}{K_{ij}} = \frac{\bar{L}_{ij}}{\bar{K}_{ij}} + \frac{\ell_i}{K_i} + \frac{\ell_j}{K_j}, \tag{5.32}$$

where ℓ_i and ℓ_j are representative length for intersections and are evaluated by geometrically averaging the apertures of the intersecting fractures. All the individual permeabilities are evaluated using the cubic law [101] as discussed in Section 5.1.2. Equations (5.29) and (5.30) are combined to yield

$$\sum_{j}^{N} w_{ij} \left(P_i - P_j\right) = 0, \tag{5.33}$$

where $w_{ij} = \frac{K_{ij} d_{ij}}{\mu L_{ij}}$. If w_{ij} are assigned as weights of edges of the graph $\mathcal{G}$, then Equation (5.33) can be transformed to

$$\boldsymbol{LP} = \boldsymbol{0}, \tag{5.34}$$

where $\boldsymbol{L}$ is the Laplacian matrix of graph $\mathcal{G}$. The vector of pressure, $\boldsymbol{P}$, needs to modified a priori to include any prescribed boundary conditions. Once the above linear system is solved, Equations (5.30) and (5.31) can be used to obtain the velocity in each fracture.

5.3.2 *Transport*

In order to solve the transport model Equation (5.1), we first build the directed graph $\mathcal{D}$ with the same topology as graph $\mathcal{G}$ and the velocities, v_{ij}, as weights. The directed graph for Figure 5.11b is depicted in Figure 5.11c. The intersections in the network, where mixing occurs, can be found by traversing graph $\mathcal{D}$. It should be noted that mixing does not happen in all intersections. The intersections at which mixing occurs in the network in Figure 5.11c are nodes 4, 6, 7 and 9, A series of distinct paths are defined in the network on which transport equation is solved separately. Each path starts from an intersection with mixing (or the inlet of the fracture network) and ends with another intersection with mixing (or the outlet of the network). The paths for Figure 5.11c are listed in Table 5.1. Finding the paths scales badly with the number of nodes, however, this step is

only needed when the topology of the network changes, e. g., after a node clogs. The transport of ions along each path is computed using the front-tracking algorithm as discussed in Section 4.3.3 on page 62 and by converting the length of paths to time-of-flights.

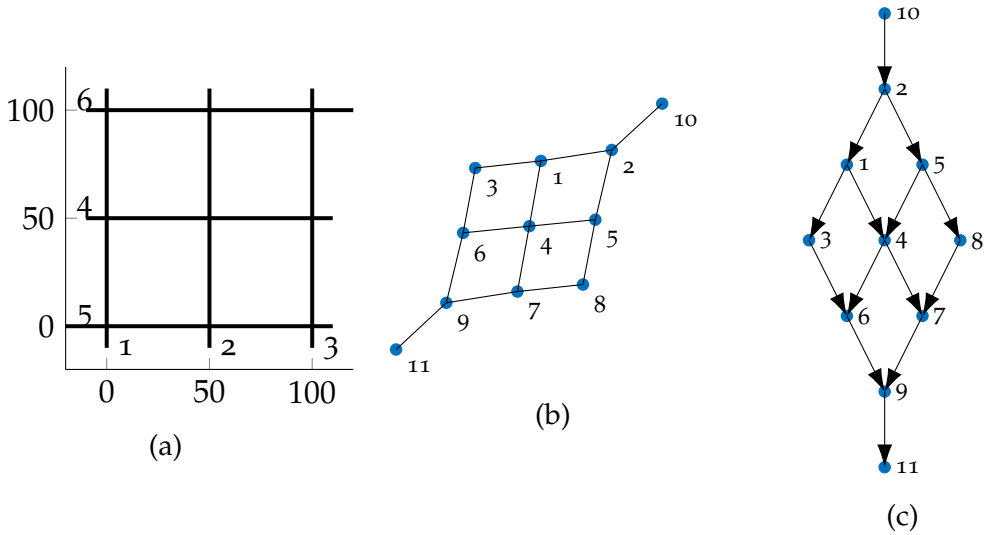

Figure 5.11: a) Fracture network of 6 fractures with equal length and random apertures $0.1mm \leq d \leq 1mm$, b) equivalent graph representation of the network c) directed graph representation that shows the direction of flows.

path number	nodes	last node (intersection with mixing)
1	10, 2, 1, 4	node 4
2	10, 2, 5, 4	
3	10, 2, 1, 3, 6	node 6
4	4, 6	
5	10, 2, 5, 8, 7	node 7
6	4, 7	
7	6, 9	node 9
8	7, 9	
9	9, 11	outlet

Table 5.1: List of all paths for problem discussed in Figure 5.11.

5.3.3 *Mixing and precipitation*

The mixing and calculation of the precipitates are carried out similar to what was discussed in Sections 5.1.3 and 5.1.4. Precipitation rates are assumed to be linear but the time step is adaptive to allow any changes to be reflected in the flow if necessary. Hence, the precipitation time is finite and bound to a threshold which will be discussed in Section 5.3.4. After each precipitation time, precipitation and dissolution rates are updated if required.

5.3.4 *Time stepping and coupling*

This section describes the strategy to choose an adaptive time step. Generally, there are three time-variables each indicating the initiation of a different process. The adaptive time is set to the minimum of these three variables.

Again, consider the concentration of components to be initially uniform everywhere in a network. Assume a new fluid with a different concentration is injected into the network. After solving the flow and finding paths we can initiate the transport of ions. The reactive transport of the injected fluid is not stopped until a wave reaches an intersection of fractures where incoming fluids mix. The arrival of a new wave at such an intersection triggers a precipitation/dissolution or it may just alter the outgoing concentration from that node. Therefore, the earliest time at which a new front reaches an intersection is of interest. This time is denoted by τ_s. At $t = \tau_s$, all precipitation rates are calculated (if any), new fronts are created, τ_s is set to infinity and the simulation continues. If dissolution is occurring, the time needed to completely dissolve the present precipitates, τ_d, is calculated using the constant dissolution rate for that intersection. For all the precipitation and dissolution that are happening on all nodes, the time at which they change the volume of that intersection by some threshold ϵ_1 is calculated. The minimum of these times is set to τ_c. The adaptive simulation time τ_a is set to

$$\tau_a = \min(\tau_s, \tau_d, \tau_c) \tag{5.35}$$

All the fronts on all the paths are advanced for τ_a and the volume of the intersections updated. If the change of the volume for an intersection is more than a threshold ϵ_2, flow is recalculated. Another threshold can be assigned for volumes below which an intersection shall be considered clogged. In this case, flow calculation should be accompanied by graph reconstruction and pathfinding. Figure 5.12 illustrates the movement of the fronts at three instances of time obtained using this method. For this problem we set the initial condition as $\boldsymbol{N}_r = \binom{1.3}{6}$ and the injection concentration as $\boldsymbol{N}_l = \binom{1.8}{2}$.

Figure 5.13 illsutrates the history of precipitation up untill 10^5 seconds at the four mixers. Due to the freshness of the upstream fluid and small amount of precipitates at the downstream the build-up of precipitates is quite slow, whereas the dissolution is very fast such that the complete dissolution of the accumlates of precipitates happend only within few time steps.

A larger network is depicted in Figure 5.14 with its equivalent undirected graph representation in Figure 5.14b. The flow is solved in this network and the flow is illustrated on the network as a directed graph in Figure 5.14c. It is assumed that the medium initially contains a uniform concentration of com-

ponents and amount of precipitates throughout the whole network as in the previous example, i. e., $\boldsymbol{N}_r = \binom{1.3}{6}$ and $\boldsymbol{N}_l = \binom{1.8}{2}$ with a constant pressure drop of one atmosphere. The overall concentration of N_A are depicted at three instances in Figure 5.15 and the history of the precipitates at the mixing nodes are in Figure 5.16

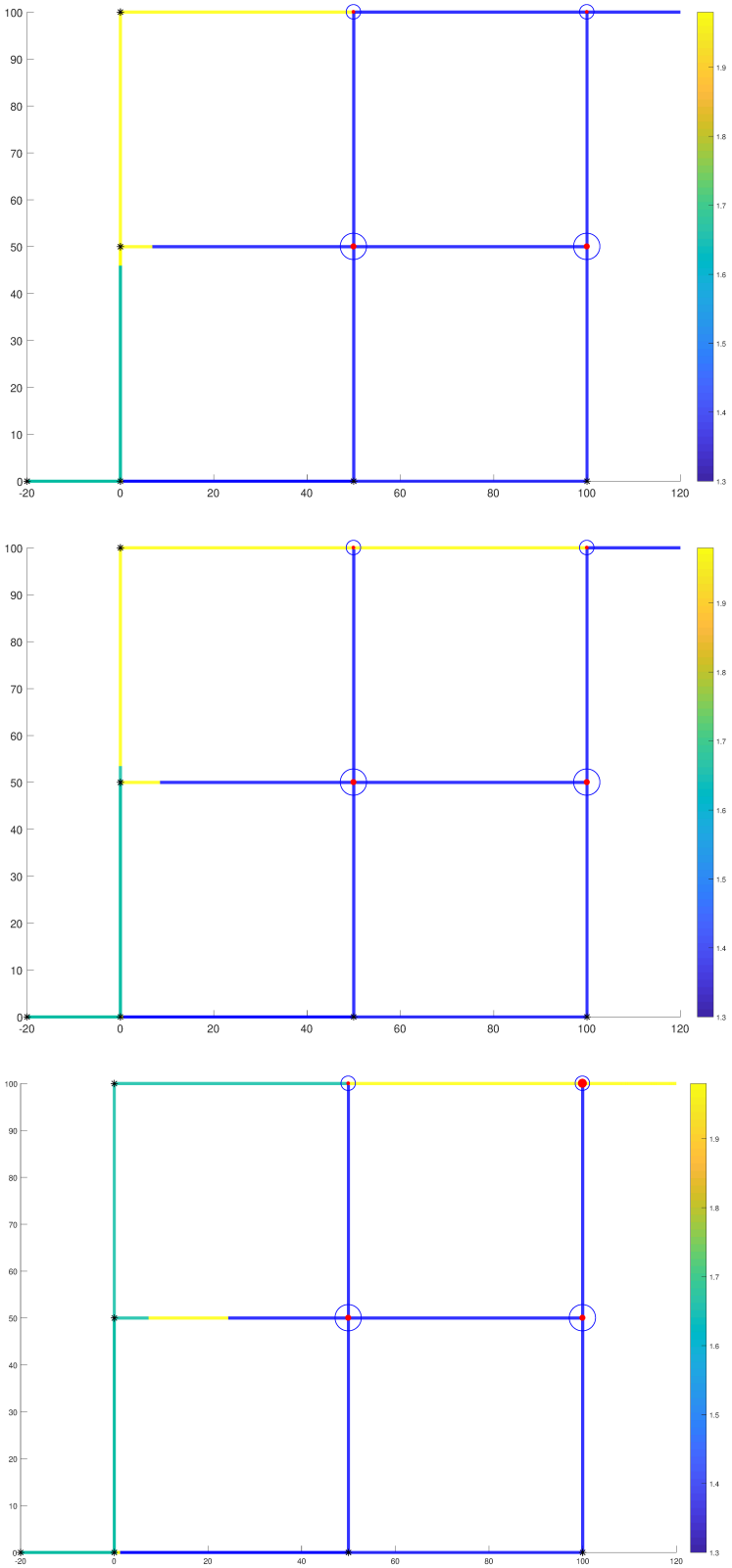

Figure 5.12: Front displacement for the network discussed in Figure 5.11 at three physical events triggered at t = 30018, 33882, 70832 from top to bottom. Intersections with mixing are represented by red dots and black circles. The black circle shows the size of the intersection relative to other intersections. The size of red dots represents how much it is filled. The color code for concentration is blue = low, yellow = high

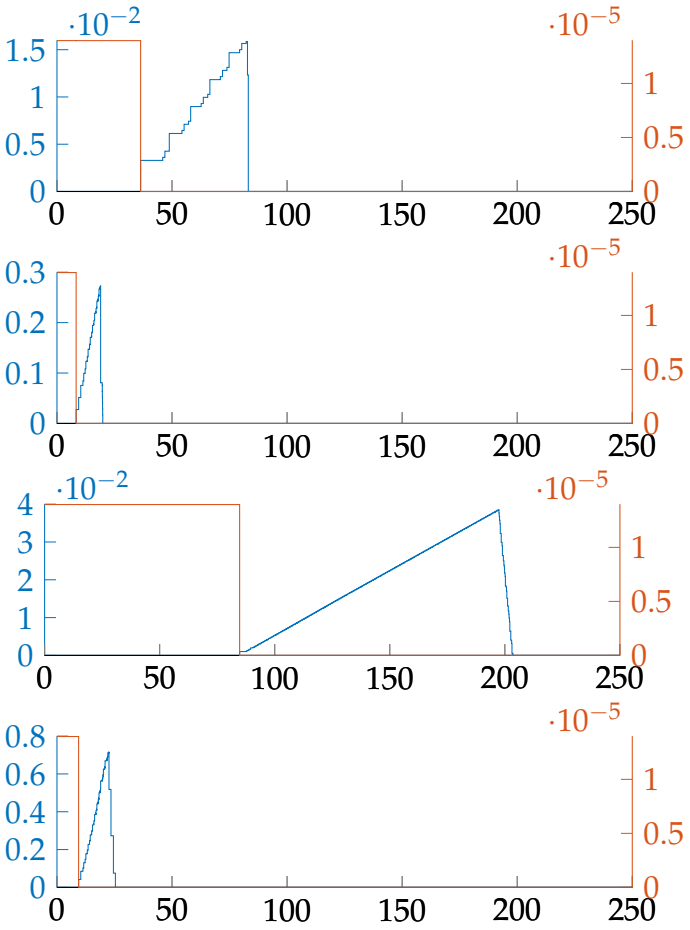

Figure 5.13: History of precipitates (upto 250 hours) for network illustrated in Figure 5.11. The figures are for nodes 4, 6, 7 and 9 from top to bottom respectively. The blue and red lines correspond to volume fraction of precipitate A and B, respectively. The changes of the concentration profile at all intersection after 250 hours are either zero or negligible and is not shown.

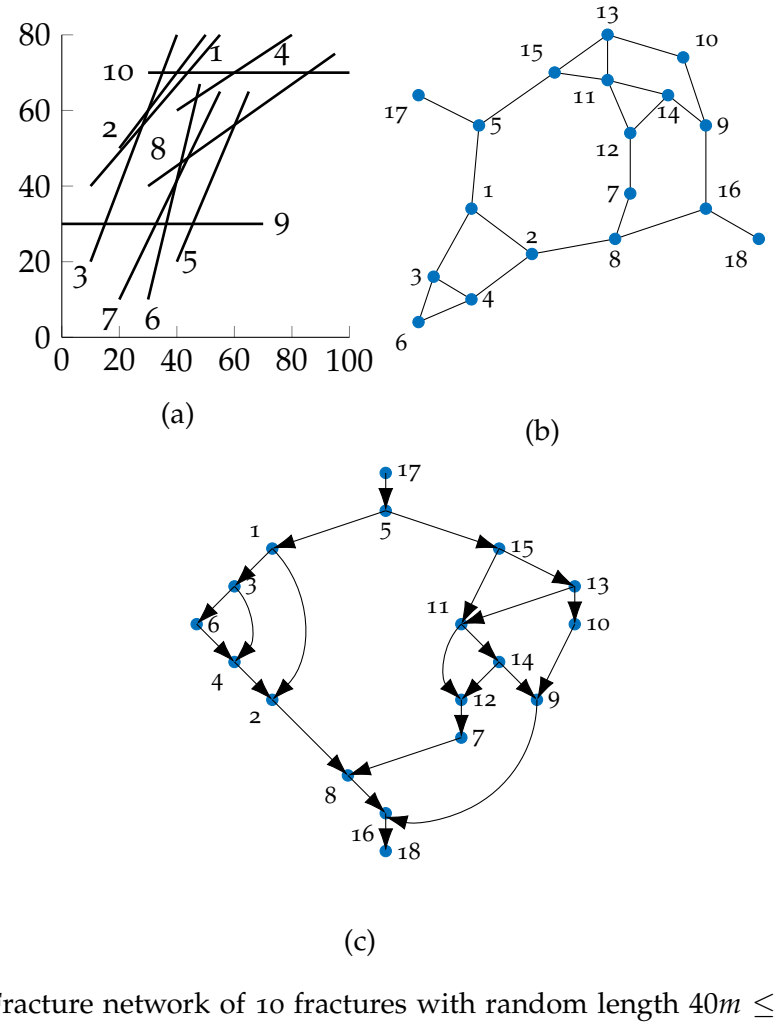

Figure 5.14: a) Fracture network of 10 fractures with random length $40m \leq l \leq 70$ and random apertures $0.1mm \leq d \leq 1mm$. The inlet is the left end of fracture 9 (point $[0, 30]$) and the outlet is right end of fracture 10 (point $[100, 70]$), b) equivalent graph representation of the network. Nodes 17 and 18 are the inlet and outlet, respectively. c) directed graph representation that shows the direction of flow.

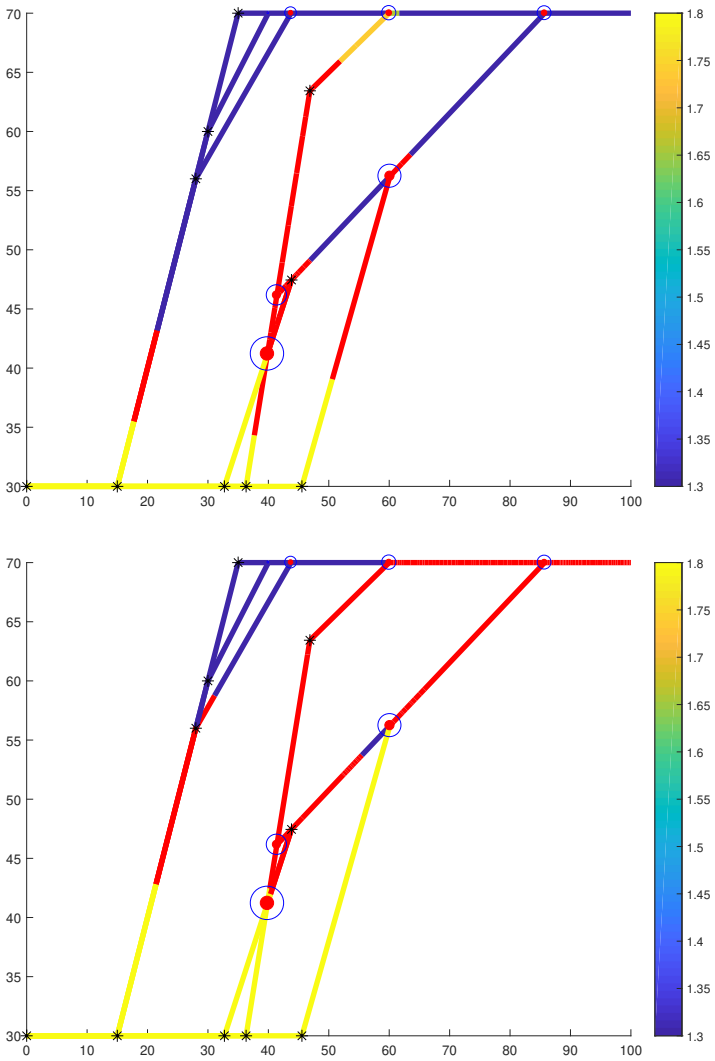

Figure 5.15: Front displacement for the network discussed in Figure 5.14 at two physical events triggered at t = 6570 (top) and 14550 (bottom). Intersections with mixing are represented by red dots and black circles. The black circle shows the size of the intersection relative to other intersections. The size of the red dots represents how much it is filled. The color code for concentration is blue = low, yellow = high, red = more than 1.8

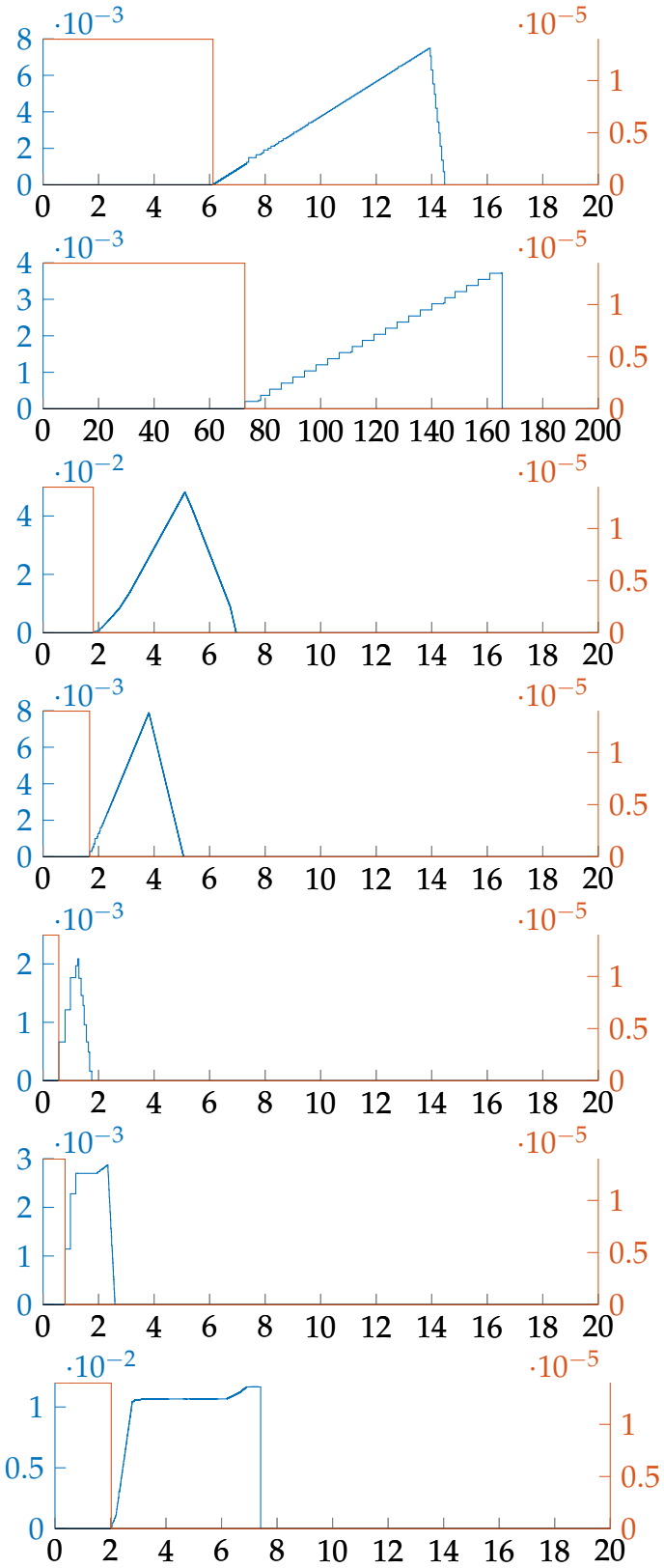

Figure 5.16: History of precipitates (upto 250 hours) for network illustrated in Figure 5.11. The figures are for nodes 2, 4, 8, 9, 11, 12 and 16 from top to bottom respectively. The blue and red lines correspond to volume fraction of precipitate A and B, respectively. The changes of the concentration profile at all intersection after 250 hours are either zero or negligible and is not shown.

In this chapter, we presented the analytical solution for precipitation and dissolution in two fractures that intersect at two points, at one of which mixing of incoming streams occur. This system was analysed and several sensitivity analysis was performed. The precipitation at the intersection is due to mixing of downstream composition with the intermediate composition that is formed due to the co-ion effect. We provided the framework of a general algorithm for larger networks of fractures and demonstrated it through a few examples. The details of the implementation of the algorithm are provided in the appendix.

For the small network, the amount of precipitate at the intersection is determined by a constant precipitation rate and a precipitation time. The effect of different parameters on the precipitation rate, precipitation time and the final amount of precipitation at the intersection was presented. In general, for a fixed initial and injection compositions,

- the precipitation (or dissolution) rate increases by an increase in the ratio of fracture apertures or by a decrease in the ratio of fracture lengths,
- the precipitation time may decrease or increase by changes in the aspect ratios,
- the final amount of precipitates can increase, decrease or remain constant when the ratio of fracture apertures or fractures length change.

For a system with fixed geometrical values, (i. e., aperture and length) and initial condition, the precipitation is minimum in the vicinity of the bifurcation line. However, changes are not uniform as the injection point on the hodograph plane moves away from the bifurcation line.

In addition, an algorithm is designed to couple flow and transport without exploiting any spatial mesh on the fractures. The approach is to use graph theory for flow calculation and front-tracking for transport. A time-stepping criterion is introduced to update flow regularly.

6

CONCLUSIONS AND RECOMMENDATIONS

This thesis provided a study on single-phase reactive flows with precipitation and dissolution of two salts that share an ion. We presented the analytical solution for the one-dimensional problems related to this type of flow. The discussed solutions considered both the cases when the precipitation affects the porosity of the medium and when it does not. The solution for both problems was presented and analysed comprehensively. As a result of accounting for the volume of the fluid, front speeds change and new intermediate states appear compared to the previous solution from [1]. The arrisal of new inetermediate states and changes in the speed of fronts creates a new phenomenon in 1D that cannot be obtained via model from [1]. The new phenomenon is referred to as self-clogging in this thesis. Self-clogging occurs when a salt is being dissolved. The other salt, due to the co-ion effect starts to precipitate. If the precipitating salt is less dense than the one that is dissolved, the model allows the volume to be changed accordingly. Hene, a reduction of volume occurs that in extreme cases clogs the system. For the self-clogging to appear in a system, two conditions need to be satisfied. The first condition is imposed by the system parameters, i. e., ratio of molar densities and ratio of equilibrium constants. Given that these ratios satisfy certain inequalities, self-clogging is impossible. The second condition is the initial and boundary condition of the problem. It is concluded that for the pair of salts Li-F and Li-Cl the first condition holds and this system is susceptible to self-clogging if also the boundary and initial conditions are within an appropriate range. Nevertheless, it should be noted that the results are subject to several assumptions.

The one-dimensional solution was also extended to account for the heterogeneities of the system. The corresponding Riemann problem admits spatial discontinuity in the flux function. It is shown that the solution to this specific problem can be obtained via the minimum jump entropy condition. A streamline simulator was developed for simulation of fronts in higher dimensions for the discussed problem. The simulator is based on the solution to the one-dimensional Riemann Problem. The flow and transport are decoupled in this problem. The implementation of such method imposes zero mixing at the well. Hence, expli-

cit mixing models are required to capture the mixing and reaction of incoming streams and, more important, accumulation of precipitates. Even though we have assumed that the reacting ions exist in both streams, mixing at the well does result in accumulation of precipitates. This is because the mixture of two streamlines, which carry saturated fluid, can be an oversaturated fluid. That is, the resulting mixture contains more ions than it can accommodate.

Finally, we studied the same problem in a discrete fracture network, i. e., a lattice of conductive paths with very small apertures. This scenario was a superposition of many problems each with a mixing well. Hence, several mixing locations exist in the problem and flow and transport could not be assumed to be decoupled in general. Several assumptions were made for simplification in order to obtain an intuition about the problem in simple settings. Ultimately, these findings were extended to couple the flow and transport in larger networks. The main finding of this was developing an algorithm to capture flow and reaction processes in this setting. The objective was not to use any spatial grid as the processes occur in different scales with multiple orders of magnitude difference. The main ingredients of the algorithm are graph theory for flow calculation, front-tracking for solving the transport problem and a semi-batch reactor model for capturing the mixing of streamlines at mixing nodes. A new strategy was proposed for updating the time-steps based initiation of physical events. Such events are defined as completion of dissolution at an intersection node, arrival of the new front to an intersection, and significant changes of pressure in the system.

While the algorithm presented for fracture networks treats the processes at different scales separately, a roadblock exists in extending the algorithm for larger networks. The challenge is the current algorithm used for finding all the paths uses $O(n!)$ operations. Two possible solutions that may decrease the order are 1: to develop and use more sophisticated algorithms in finding paths, and 2: to use a simple backbone for complex networks. While the second option has already been implemented in different applications, it is not trivial when this backbone needs to be updated considering the intersections are continuously changing in volume. Hence, it appears the first solution may be more practical.

The problems discussed in this thesis were first initiated to address the formation of two common salts, namely barite and anhydrite, in the production of oil in the North Sea. A potential direction where this research can be expanded and used for is, therefore, prediction of scales. However, it can also be used in the removal of heavy metal from the soil where chemical reactions are similar. Another possible application is in processes with ion-exchange as discussed in Section 2.5. In our approach, we have made several assumptions in developing the presented models and their solutions. The degree of the resulting mathem-

atical complexity in relaxing some of these premises are higher, e. g., chemical equilibrium. Although further development based on reaction kinetics requires a different strategy, the addition of non-reacting ion or an immiscible phase increases the degrees of freedom by one and is simpler to incorporate. Hence, other applications such as reactive transport of nuclear waste and CO_2 injection in fractured porous media may be a target for the methodology presented.

A

APPENDIX

A.1 SECONDARY VARIABLES FOR THE CASE OF VARIABLE POROSITY

In this section, we derive the explicit expressions for the secondary variables, $n_A\,(N_A, N_B)$, $n_B(N_A, N_B)$, $\phi_A(N_A, N_B)$ and $\phi_B(N_A, N_B)$, for each region. The expressions are given separately for each of the four regions in the hodograph plane.

In region $AUBU$, $\phi_A = \phi_B = 0$ hold true and Equations (2.6a) and (2.6b) are solved for n_A, n_B:

$$n_\pi(N_A, N_B) = \frac{N_\pi}{\phi_P}, \quad \pi = \{A, B\} \tag{A.1}$$

For Region $ASBU$ we have $\phi_B = 0$ and thus from Equation (2.6b) we obtain

$$\phi_A = \phi_P - \frac{N_B}{n_B(N_A, N_B)}, \tag{A.2a}$$

where n_B is derived from Equation (2.2) as

$$n_B(N_A, N_B) = \frac{(\tilde{n}_A)^2 - (n_A(N_A, N_B))^2}{n_A(N_A, N_B)}. \tag{A.2b}$$

For finding n_A, $\phi_B = 0$ and Equations (A.2a) and (A.2b) are inserted into in Equation (2.6a) and therefore

$$n_A = \frac{\omega_A N_B - \sqrt{Y}}{2(N_A + N_B - \omega_A \phi_P)}, \tag{A.2c}$$

where $Y = (\omega_A N_B)^2 - 4(N_A + N_B - \omega_A \phi_P)(\omega_A \phi_P - N_A)\,(\tilde{n}_A)^2$.

It can be shown that for this region that the following holds true

$$\frac{\partial n_B(N_A, N_B)}{\partial N_A} = \left(-1 - \frac{(\tilde{n}_A)^2}{(n_A(N_A, N_B))^2} \right) \frac{\partial n_A(N_A, N_B)}{\partial N_A}, \tag{A.2d}$$

$$\frac{\partial n_B(N_A, N_B)}{\partial N_B} = \left(-1 - \frac{(\tilde{n}_A)^2}{(n_A(N_A, N_B))^2} \right) \frac{\partial n_A(N_A, N_B)}{\partial N_B}. \tag{A.2e}$$

In region $ASBS$, the concentrations inside the fluid do not change. The concentrations are the value at $\boldsymbol{N}_t$, i. e.

$$n_A(N_A, N_B) = \hat{n}_A, \quad n_B(N_A, N_B) = \hat{n}_B. \tag{A.3a}$$

Therefore, all the derivatives in the Jacobian matrix are zero. The expressions for ϕ_A and ϕ_B thus reads

$$\phi_A = \frac{\hat{n}_A \left(\omega_B \phi_P - N_B\right) - N_A \left(\omega_B - \hat{n}_B\right)}{\hat{n}_A \omega_A + \hat{n}_B \omega_B - \omega_A \omega_B}, \tag{A.3b}$$

$$\phi_B = \frac{\hat{n}_B \left(\omega_A \phi_P - N_A\right) - N_B \left(\omega_A - \hat{n}_A\right)}{\hat{n}_A \omega_A + \hat{n}_B \omega_B - \omega_A \omega_B}. \tag{A.3c}$$

A.2 EIGENPROBLEM

We seek the solution of the eigenvalue problem $\mathcal{J}\boldsymbol{r}_p = \lambda_p \boldsymbol{r}_p$ where λ_p and $\boldsymbol{r}_p$ denote the p-th eigenvalue and eigenvector, respectively, for the Jacobian matrix of the flux functions as defined in Appendix A.1.

In region $AUBU$, we obtain a diagonal matrix for $\mathcal{J}$ with both diagonal entries as $1/\phi_P$. Therefore, $\lambda_1 = \lambda_2 = 1/\phi_P$ and the directions of the eigenvectors are arbitrary.

In region $ASBS$ the problem is trivial since $\mathcal{J} \equiv 0$.

For region $ASBU$, it can be shown

$$\frac{\partial n_A(N_A, N_B)}{\partial N_B} = \frac{\omega_A \phi_P - N_A}{N_B} \frac{\partial n_A(N_A, N_B)}{\partial N_A}. \tag{A.4}$$

After some algebraic calculation, we obtain

$$\frac{\partial n_A}{\partial N_A}\frac{\partial n_B}{\partial N_B} - \frac{\partial n_A}{\partial N_B}\frac{\partial n_B}{\partial N_A} = 0,$$

i. e., the determinant of $\mathcal{J}$ is zero and thus $\lambda_1 = 0$. The other eigenvalue is the trace of $\mathcal{J}$. It is possible to show, using simple algebraic calculations that, $\lambda_2 = \left(\frac{\partial n_A}{\partial N_A}\right)_{N_B} + \left(\frac{\partial n_B}{\partial N_B}\right)_{N_A} = \frac{1}{\phi_P - \phi_A}$.

The first eigenvector is

$$\boldsymbol{r}_1 = \begin{pmatrix} \lambda_1 - \mathcal{J}_{22} \\ \mathcal{J}_{21} \end{pmatrix} = \begin{pmatrix} -\mathcal{J}_{22} \\ \mathcal{J}_{21} \end{pmatrix} = \begin{pmatrix} \frac{\partial n_B}{\partial N_B} \\ \frac{\partial n_B}{\partial N_A} \end{pmatrix} = \left(\frac{(\tilde{n}_A)^2}{(n_A)^2} + 1 \right) \frac{\partial n_A}{\partial N_A} \begin{pmatrix} \frac{\phi_P \omega_A - N_B^p}{-N_C^p} \\ 1 \end{pmatrix}.$$

This means $\boldsymbol{r}_1$ is parallel to the line $\mathcal{I}_1 = \left\{ (N_A, N_B) | N_B = \frac{-N_B^p}{\phi_P \omega_A - N_A^p} (N_A - \phi_P \omega_A) \right\}$ and therefore the family of lines emerging from $\begin{pmatrix} \phi_P \omega_A \\ 0 \end{pmatrix}$ are slow integral curves.

Using the partial derivatives of the flux functions for this region, we obtain

$$\boldsymbol{r}_2 = \begin{pmatrix} -1 \\ 1 + \left(\frac{\tilde{n}_A}{n_A} \right)^2 \end{pmatrix}.$$

Using the expression Equations (A.2a) to (A.2c) we can evaluate $\nabla_{(N_A, N_B)} \phi_A = \begin{pmatrix} \frac{\partial \phi_A}{\partial N_A} & \frac{\partial \phi_A}{\partial N_B} \end{pmatrix}^T$ and show $\nabla_{(N_A, N_B)} \phi_A \cdot \boldsymbol{r}_2 = 0$ for the curve $\phi_A(N_A, N_B) \equiv \varphi$. Therefore, iso-porosity curves are fast integral curves.

A.3 ADMISSIBLE AND INADMISSIBLE SHOCKS

Theorem 1 (Slow shocks)**.** *A wave with the left state in AUBU and the right state in ASBU is a slow shock, provided that left and right states and* $\begin{pmatrix} \phi_P \omega_A \\ 0 \end{pmatrix}$ *form a straight line.*

Proof. For $\boldsymbol{N}_l = \begin{pmatrix} N_A^l \\ N_B^l \end{pmatrix} \in AUBU$, we chose an arbitrary point $\boldsymbol{N}_r = \begin{pmatrix} N_A^r \\ N_B^r \end{pmatrix} \in ASBU$ on the line

$$l_A = \left\{ (N_A, N_B) | N_B = \frac{N_B^l}{N_A^l} - \omega_A \phi_A (N_A - N_A^l) + N_B^l \right\} \tag{A.5}$$

and show that this point belongs to $\mathcal{H}_1(\boldsymbol{N}_l)$.

The expressions for the coordinates of the left and right states together with the equation of the line can be simplified to obtain

$$\frac{n_A - n_A^l}{N_A^p - N_A^l} = \frac{n_B - n_B^l}{N_B^p - N_B^l}.$$

In words, the arbitrary point satisfies the Rankine-Hugoniot condition.

Since the slope of l_A in Equation (A.5), $-\omega_A \phi_A$, is negative, $N_B^r < N_B^l$ holds true. This allows us to show

$$\bar{v}(\boldsymbol{N}_p; \boldsymbol{N}_r) = \left(\frac{N_B^r}{\phi_P - \phi_A^r} - \frac{N_B^l}{\phi_P} \right) \Big/ \left(N_B^r - N_B^l \right) < \frac{1}{\phi_P} = \lambda_1(\boldsymbol{N}_r).$$

On the other hand, if we express ϕ_A in terms of N_A^r and N_B^r, we can show $\bar{v}(\boldsymbol{N}_l; \boldsymbol{N}_r) > 0 = \lambda_1(\boldsymbol{N}_l)$. □

From the above theorem, a shock with left state in $AUBU$ and right state in $ASBU$ is stable. In addition, a shock with the left state in $ASBS$ and the right state in $ASBU$ is unstable because, for $\boldsymbol{N}_l \in ASBS$, $\lambda_1(\boldsymbol{N}_l) = \lambda_2(\boldsymbol{N}_l) = 0$ and therefore any shock violates Lax entropy condition.

Theorem 2 (Detached $\mathcal{H}$)**.** *For a point in $ASBU$, the detached branch of the Hugoniot locus is not admissible.*

Proof. We prove, by contradiction, that a shock with the right state on the detached branch of $\mathcal{H}$ is unstable. For a given point

$$\boldsymbol{N}_l = \begin{pmatrix} N_A^l \\ N_B^l \end{pmatrix} = \begin{pmatrix} n_A^l(\phi_P - \phi_A^l) + \omega_A \phi_A^l \\ n_B^l(\phi_P - \phi_A^l) \end{pmatrix} \in ASBU,$$

let $\mathcal{R}$ be the set all points in the detached $\mathcal{H}$. It can be directly shown that $\exists \boldsymbol{N}_s \in \mathcal{R}$ such that $N_A^s = n_A^s = 0$. In addition,

$$\boldsymbol{N}_s = \begin{pmatrix} N_A^s \\ N_B^s \end{pmatrix} = \begin{pmatrix} 0 \\ \frac{N_A^l}{n_B^l}(n_B^s - n_B^l) + N_B^l \end{pmatrix},$$

where $n_B^s = \tilde{n}_B$ because the fluid is only saturated with B and does not contain any A. The proof has three parts:

I- First, we prove that

$$\arg\min_{\boldsymbol{N}_r \in \mathcal{R}} \lambda_2(\boldsymbol{N}_r) = \boldsymbol{N}_s.$$

From Appendix A.2, we know $\lambda_2(\boldsymbol{N}_r) = \frac{1}{\phi_P - \phi_B^r}$. Therefore, we only need to prove $\min_{\boldsymbol{N}_r} \phi_B^r = \phi_B^s$, i. e., the lower end of the detached $\mathcal{H}$ curve has the lowest precipitate volume. Since the other end of the curve has the lowest porosity and the curve is continuous, it remains to show that no other point has porosity equal to that of $\boldsymbol{N}_s$. We prove this by contradiction: Suppose $\exists \boldsymbol{N}_r \in \mathcal{H}(\boldsymbol{N}_l), \boldsymbol{N}_r \neq \boldsymbol{N}_s$ such that $\phi_B^r = \phi_B^r$. Since $\boldsymbol{N}_s \in \mathcal{H}(\boldsymbol{N}_l)$ we can derive a relation for ϕ_B^s. Replacing this for $\boldsymbol{N}_r$ we obtain two expressions for n_A^r and n_B^r

$$n_A^r = n_A^l \frac{\tilde{n}_B - n_B^r}{\tilde{n}_B - n_B^l},$$
$$n_B^r = \tilde{n}_B - \frac{n_A^r}{n_A^l}(\tilde{n}_B - n_A^l),$$

which do not satisfy the charge balance equation. Therefore, we have proved by contradiction that such a point does not exist.

II- Next, we show that

$$\arg\max_{\boldsymbol{N}_r \in \mathcal{R}} \bar{v}\left(\boldsymbol{N}_l; \boldsymbol{N}_r\right) = \boldsymbol{N}_s.$$

Since $\forall \boldsymbol{N}_r \in \mathcal{R}, \boldsymbol{N}_r \neq \boldsymbol{N}_s$ we have

$$\bar{v}\left(\boldsymbol{N}_l - \boldsymbol{N}_s\right) - \bar{v}\left(\boldsymbol{N}_l - \boldsymbol{N}_r\right) = \frac{n^l_A}{N^l_A} - \frac{n^l_A - n^r_A}{N^l_A - N^r_A} = \frac{-n^l_A N^r_A + n^r_A N^l_A}{N^l_A (N^l_A - N^r_A)} = \frac{-n^l_A (n^r_A (\phi_P - \phi^r_B)) + n^r_A (n^l_A (\phi_P - \phi^l_A) + \phi^l_A \omega_A)}{N^l_A (N^l_A - N^r_A)} = \frac{n^l_A n^r_A \phi^r_B + n^r_A (\phi^l_A (\omega_A - n^l_A))}{N^l_A (N^l_A - N^r_A)} > 0.$$

III- Last, we know that

$$\lambda_2(\boldsymbol{N}_l) > \bar{v}(\boldsymbol{N}_l; \boldsymbol{N}_r),$$
$$\lambda_2(\boldsymbol{N}_r) > \bar{v}(\boldsymbol{N}_l; \boldsymbol{N}_r),$$

i. e., all $\boldsymbol{N}_r \in \mathcal{R}$ violate the Lax entropy condition and therefore the shock is not admissible.

□

The following two lemmas are used to prove the uniqueness of the solution to case 10 (Theorem 3).

Lemma 1 (bifurcation line z)**.** *Suppose $\boldsymbol{N}_l \in AUBU$ and $\boldsymbol{N}_r \in ASBS$. Let z be the line passing through $\boldsymbol{N}_r$ and $\boldsymbol{N}_t = \begin{pmatrix} N^t_B \\ N^t_C \end{pmatrix} = \begin{pmatrix} \hat{n}_A \phi_P \\ \hat{n}_B \phi_P \end{pmatrix}$. Let also $\boldsymbol{N}_{iA} = \mathcal{H}(\boldsymbol{N}_l) \cap \mathcal{H}(\boldsymbol{N}_r) \cap ASBU$ and $\boldsymbol{N}_{iB} = \mathcal{H}(\boldsymbol{N}_l) \cap \mathcal{H}(\boldsymbol{N}_r) \cap AUBS$. If $\boldsymbol{N}_l \in l$ then $\bar{v}(\boldsymbol{N}_l; \boldsymbol{N}_{iA}) = \bar{v}(\boldsymbol{N}_{iA}; \boldsymbol{N}_r)$ and $\bar{v}(\boldsymbol{N}_l; \boldsymbol{N}_{iB}) = \bar{v}(\boldsymbol{N}_{iB}; \boldsymbol{N}_r)$.*

Proof. The proof is tedious with trivial algebraic calculations. We only sketch the outline of the proof for $\bar{v}\left(\boldsymbol{N}_l; \boldsymbol{N}_{iA}\right) = \bar{v}\left(\boldsymbol{N}_{iA}; \boldsymbol{N}_r\right)$. The other equality $\bar{v}\left(\boldsymbol{N}_l; \boldsymbol{N}_{iB}\right) = \bar{v}\left(\boldsymbol{N}_{iB}; \boldsymbol{N}_r\right)$ can be proved similarly. To do this, a system of 5 equations with 5 unknowns need to be solved. The unknowns are the coordinates of $\boldsymbol{N}_{iA}$ in the hodograph plane (2), its fluid concentrations (2) and the amount of percipitate A. The equations are

1, 2. Total concentration for $\boldsymbol{N}_{iA}$,

3. Charge balance for $\boldsymbol{N}_{iA}$,

4. $\boldsymbol{N}_{iA} \in \mathcal{H}(\boldsymbol{N}_l)$,

5. $\boldsymbol{N}_{iA} \in \mathcal{H}(\boldsymbol{N}_r)$.

□

Lemma 2 (Diversion from the bifurcation line z)**.** *Suppose $\boldsymbol{N}_r \in ASBS$ and $\boldsymbol{N}_l \in AUBU$ lies on the line z defined in Lemma 1. Let l_{ASBU} be part of $\mathcal{H}_1(\boldsymbol{N}_l)$ that lies in $ASBU$. Then, for any point $\boldsymbol{N}_\zeta$ with $N_A^\zeta > N_A^l$ that lies on line l_{ASBU} we obtain $\bar{v}(\boldsymbol{N}_\zeta; \boldsymbol{N}_{iA}) > \bar{v}(\boldsymbol{N}_{iA}; \boldsymbol{N}_r)$. The resulting inequality is inverse when $N_A^\zeta < N_A^l$.*

Proof. Consider the case where $N_A^\zeta > N_A^l$; $\boldsymbol{N}_{iA}$, or the intermediate point in the region $ASBU$, is identical for both points $\boldsymbol{N}_l$ and $\boldsymbol{N}_\zeta$.

From Lemma 1, we obtain that $\mathcal{W}_1$ and $\mathcal{W}_2$ in $\boldsymbol{N}_l \xrightarrow{\mathcal{W}_1} \boldsymbol{N}_{iA} \xrightarrow{\mathcal{W}_2} \boldsymbol{N}_r$ have equal velocities $\bar{v}(\boldsymbol{N}_l; \boldsymbol{N}_{iA}) = \bar{v}(\boldsymbol{N}_{iA}; \boldsymbol{N}_r) = \frac{n_A^l - n_A^{iA}}{N_A^l - N_A^{iA}}$. On the other hand, since the intermediate points for both cases coincide, $\mathcal{W}_2^*$ in $\boldsymbol{N}_l \xrightarrow{\mathcal{W}_1^*} \boldsymbol{N}_{iB} \xrightarrow{\mathcal{W}_2^*} \boldsymbol{N}_r$ and $\mathcal{W}_2$ are identical. It remains to show $\bar{v}(\boldsymbol{N}_\zeta; \boldsymbol{N}_{iB}) > \bar{v}(\boldsymbol{N}_l; \boldsymbol{N}_{iB})$. The later is possible to prove because $\phi_P < 1$ and therefore

$$n_A^\zeta - n_A^l > N_A^\zeta - N_A^l > 0,$$

Similarly, opposite results could be obtained by assuming $\boldsymbol{N}_\zeta$ on the left of $\boldsymbol{N}_l$ or

$$n_A^\zeta - n_A^l < N_A^\zeta - N_A^l < 0.$$

□

Theorem 3. *For a Riemann Problem with $\boldsymbol{N}_r \in ASBS$ and $\boldsymbol{N}_l \in AUBU$ below the bifurcation line z defined in Lemma 1 (case 10 in Section 3.3), the intermediate state lies in $ASBU$.*

Proof. Since, $\boldsymbol{N}_l \in AUBU$, $\exists \boldsymbol{N}_l^* \in AUBU$ that also lies on l_{ASBU} (defined in the proof of Lemma 2), i.e $\mathcal{H}_1(\boldsymbol{N}_l) = \mathcal{H}_1(\boldsymbol{N}_l^*)$. Therefore, we have

$$M(\boldsymbol{N}_l; \boldsymbol{N}_r) = M(\boldsymbol{N}_l^*; \boldsymbol{N}_r) = \boldsymbol{N}_{iA},$$

where by $M(\boldsymbol{N}_l; \boldsymbol{N}_r)$, denotes the intermediate state of the Riemann Problem with initial states $\boldsymbol{N}_l$ and $\boldsymbol{N}_r$. From Lemmas 1 and 2 we obtain

$$\bar{v}(\boldsymbol{N}_l^*; \boldsymbol{N}_{iA}) = \bar{v}(\boldsymbol{N}_{iA}; \boldsymbol{N}_r) > \bar{v}(\boldsymbol{N}_l; \boldsymbol{N}_{iA})$$

In addition, (again from Lemmas 1 and 2):

$$\begin{aligned} \forall \boldsymbol{N}_l,\ \exists \boldsymbol{N}_l^{**} \in l_{AUBS} \quad \text{s.t.} \quad & AUBS \supset M(\boldsymbol{N}_l; \boldsymbol{N}_r) = M(\boldsymbol{N}_l^{**}; \boldsymbol{N}_r) = \boldsymbol{N}_{iB}, \\ & \Rightarrow \bar{v}(\boldsymbol{N}_l^{**}; \boldsymbol{N}_{iB}) = \bar{v}(\boldsymbol{N}_{iB}; \boldsymbol{N}_r) < \bar{v}(\boldsymbol{N}_l; \boldsymbol{N}_{iB}) \end{aligned}$$

Therefore the stable solution is the one with the intermediate point in $ASBU$. □

Theorem 4. *For case 11, when the left state does not belong to region α (Figures 3.13a and 3.14a), the solution with intermediate state in AUBS is not admissible.*

Proof. The proof is tedious with trivial algebraic calculations, so a sketch of the proof is presented instead. First, we take the left state exactly on the extension of B^{AS} and we show that $\mathcal{S}_1$ and $\mathcal{S}_2$ the velocity of the shocks from $\boldsymbol{N}_l$ to $\boldsymbol{N}_{i1}$ and from $\boldsymbol{N}_{i1}$ to $\boldsymbol{N}_{i2}$ are equal. Moving $\boldsymbol{N}_l$ along the trajectory $\begin{pmatrix} 0 \\ \phi_P \omega_B \end{pmatrix}$ and $\boldsymbol{N}_l$, the solution to the Riemann Problem would yield an identical intermediate point. Therefore, the velocity of the second shock (from $\boldsymbol{N}_{i1}$ to $\boldsymbol{N}_{i2}$) remains constant whereas the first velocity, due to Lemma 2 increases. This violates our admissibility condition. To show that the velocities are the same when $\boldsymbol{N}_l$ is exactly on the extension of B^{AS}, one has to solve a system of 5 equations:
1. $\boldsymbol{N}_{i1} \in \mathcal{H}(\boldsymbol{N}_l)$,
2. $\boldsymbol{N}_{i2} \in \mathcal{H}(\boldsymbol{N}_{i1})$,
3. Charge balance for $\boldsymbol{N}_{i1}$ i.e.: $n_B^{i1}(n_A^{i1} + n_B^{i1}) = k_B$,
4. Charge balance for $\boldsymbol{N}_{i2}$ i.e.: $n_B^{i2}(n_A^{i2} + n_B^{i2}) = k_B$,
5. $\boldsymbol{N}_{i2} \in B^{AS}$.
We have not considered ϕ_A^{i2} in the set of known because $\boldsymbol{N}_{i2} \in \mathcal{I}_2(\boldsymbol{N}_r)$ implies $\phi_A^{i2} = \phi_A^r$. Solving this system gives us the elements we need to show $\bar{v}(\boldsymbol{N}_r; \boldsymbol{N}_{i1}) = \bar{v}(\boldsymbol{N}_{i1}; \boldsymbol{N}_{i2})$ □

A.4 SECONDARY VARIABLES FOR THE CASE OF CONSTANT POROSITY

In this section, we derive the expressions for the secondary variables in terms of the primary variables N_A and N_B for the case that precipitates do not take volume, i. e., relevant to Chapter 4.

For the secondary variables n_A and n_B, we note that they are continuous but not necessarily differentiable across the borders. In general $\boldsymbol{n}$ expressions differ depending on the location of $\boldsymbol{N}$.

A fluid in region $AUBU$ is unsaturated with respect to both ions A and B and hence

$$n_\pi = \frac{N_\alpha}{\phi},\ \pi = \{\mathrm{A}, \mathrm{B}\} \tag{A.6}$$

In region $ASBS$, we have saturation with respect to both ions and therefore

$$n_\pi = \hat{n}_\pi. \tag{A.7}$$

To find concentrations for region $ASBU$, we use Equation (2.6b) to obtain n_B and then replace it in Equation (2.1a) and solve for n_A,

$$n_B = \frac{N_B}{\phi}, \quad n_A = \frac{1}{2}\sqrt{\left(\frac{N_B}{\phi}\right)^2 + 4\left(\tilde{n}_A\right)^2} - \frac{N_B}{2\phi}. \tag{A.8}$$

Similar to region $ASBU$, the concentrations for region $AUBS$ can be obtained

$$n_A = \frac{N_A}{\phi}, \quad n_B = \frac{1}{2}\sqrt{\left(\frac{N_A}{\phi}\right)^2 + 4\left(\tilde{n}_B\right)^2} - \frac{N_A}{2\phi}. \tag{A.9}$$

REFERENCES

[1] F. G. Helfferich. *The theory of precipitation/dissolution waves*. AIChE Journal, **35**(1): 75–87 (1989). doi:10.1002/aic.690350108. (Cited on pages ii, 2, 3, 46, 50, 54, 73, 82, and 98.)

[2] A. Collins. *Geochemistry of oilfield waters*, volume 1. Elsevier, Amsterdam;Oxford;New York (1975). (Cited on page 1.)

[3] L. P. Dake. *Fundamentals of reservoir engineering*, volume 8. Elsevier (1983). (Cited on page 1.)

[4] L. W. Lake. *Enhanced oil recovery*. Old Tappan, NJ; Prentice Hall Inc. (1989). (Cited on page 1.)

[5] K. S. Sorbie and E. J. Mackay. *Mixing of injected, connate and aquifer brines in waterflooding and its relevance to oilfield scaling*. Journal of Petroleum Science and Engineering, **27**(1-2): 85–106 (2000). doi:10.1016/S0920-4105(00)00050-4. (Cited on page 1.)

[6] A. J. ABBAS. *Descaling of Petroleum Production Tubing utilising Aerated High Pressure Flat Fan Water Sprays*. Ph.D. thesis, Salford (2014). (Cited on page 1.)

[7] O. Vazquez, G. Ross, M. Jordan, D. A. A. Baskoro, E. Mackay, C. Johnson and A. Strachan. *Automatic Optimisation of Oilfield Scale Inhibitor Squeeze Treatments Delivered by DSV*. In *SPE International Conference on Oilfield Chemistry*. Society of Petroleum Engineers, Montgomery (2017). doi:10.2118/184535-MS. (Cited on page 1.)

[8] K. Jarrahian, L. S. Boak, A. J. Graham, M. A. Singleton and K. S. Sorbie. *Experimental Investigation of the Interaction between a Phosphate Ester Scale Inhibitor and Carbonate Rocks for Application in Squeeze Treatments*. Energy & Fuels, **33**(5): 4089–4103 (2019). doi:10.1021/acs.energyfuels.9b00382. (Cited on page 1.)

[9] A. Alvarez, W. Lambert, J. Bruining and D. Marchesin. *The Riemann Solution for Carbonated Waterflooding*. In *15th European Conference on the Mathematics of Oil Recovery*, 1–19 (2016). doi:10.3997/2214-4609.201601855. (Cited on page 1.)

[10] E. J. Mackay, K. S. Sorbie, V. M. Kavle, E. Sorhaug, K. B. Melvin, K. Sjursaeter and M. M. Jordan. *Impact of In Situ Sulphate Stripping on Scale Management in the Gyda Field*. In *SPE International Oilfield Scale Symposium*, 1–11. Society of Petroleum Engineers (2006). doi:10.2118/100516-MS. (Cited on page 1.)

[11] T. F. R. Hassane. *The application of streamline reservoir simulation calculations to the management of oilfield scale*. Ph.D. thesis, Herriot-Watt University (2013). (Cited on page 1.)

[12] A. McNaught and A. D. Wilkinson. *common-ion effect (on rates)*. In *IUPAC Compendium of Chemical Terminology*. IUPAC, Oxford, 2nd edition (1997). doi:10.1351/goldbook.C01191. (Cited on page 2.)

[13] C. A. J. Appelo and D. Postma. *Geochemistry, Groundwater and Pollution*. CRC press, London, 2 edition (2004). (Cited on page 2.)

[14] C. F. Novak, R. S. Schechter and L. W. Lake. *Rule-based mineral sequences in geochemical flow processes*. AIChE Journal, **34**(10): 1607–1614 (1988). doi:10.1002/aic.690341004. (Cited on page 2.)

[15] S. L. Bryant, R. S. Schechter and L. W. Lake. *Mineral sequences in precipitation/dissolution waves*. AIChE Journal, **33**(8): 1271–1287 (1987). doi:10.1002/aic.690330805. (Cited on pages 2 and 3.)

[16] M. P. Walsh, S. L. Bryant, R. S. Schechter and L. W. Lake. *Precipitation and Dissolution of Solids Attending Flow Through Porous Media*. American Institute of Chemical Engineers, **30**(2): 317–328 (1984). doi:10.1002/aic.690300222. (Cited on page 2.)

[17] P. G. Bedrikovetsky, E. J. Mackay, R. M. Silva, F. M. Patricio and F. F. Rosário. *Produced water re-injection with seawater treated by sulphate reduction plant: Injectivity decline, analytical model*. Journal of Petroleum Science and Engineering, **68**(1-2): 19–28 (2009). doi:10.1016/j.petrol.2009.05.015. (Cited on page 2.)

[18] P. Knabner, C. van Duijn and S. Hengst. *An analysis of crystal dissolution fronts in flows through porous media. Part 1: Compatible boundary conditions*. Advances in Water Resources, **18**(3): 171–185 (1995). doi:10.1016/0309-1708(95)00005-4. (Cited on pages 2 and 3.)

[19] A. Agosti, L. Formaggia and A. Scotti. *Analysis of a model for precipitation and dissolution coupled with a Darcy flux*. Journal of Mathematical Analysis and Applications, **431**(2): 752–781 (2015). doi:10.1016/j.jmaa.2015.06.003. (Cited on page 2.)

[20] F. A. Radu, A. Muntean, I. S. Pop, N. Suciu and O. Kolditz. *A mixed finite element discretization scheme for a concrete carbonation model with concentration-dependent porosity*. Journal of Computational and Applied Mathematics, **246**: 74–85 (2013). doi:10.1016/j.cam.2012.10.017. (Cited on pages 2 and 3.)

[21] O. M. Phillips. *Flow-controlled reactions in rock fabrics*. Journal of Fluid Mechanics, **212**: 263–278 (1990). doi:10.1017/S0022112090001951. (Cited on page 2.)

[22] C. Zhang, K. Dehoff, N. Hess, M. Oostrom, T. W. Wietsma, A. J. Valocchi, B. W. Fouke and C. J. Werth. *Pore-scale study of transverse mixing induced CaCO3 precipitation and permeability reduction in a model subsurface sedimentary system*. Environmental Science and Technology, **44**(20): 7833–7838 (2010). doi:10.1021/es1019788. (Cited on page 2.)

[23] J. R. Wood and T. A. Hewett. *Fluid convection and mass transfer in porous sandstones-a theoretical model*. Geochimica et Cosmochimica Acta, **46**(10): 1707–1713 (1982). doi:10.1016/0016-7037(82)90111-9. (Cited on page 2.)

[24] D. S. Korzhinskii. *The theory of systems with perfectly mobile components and processes of mineral formation*. American Journal of Science, **263**(3): 193–205 (1965). doi:10.2475/ajs.263.3.193. (Cited on page 2.)

[25] D. Korzhinskii. *The theory of metasomatic zoning*. Mineralium Deposita, **3**(3): 222–231 (1968). doi:10.1007/BF00207435.

[26] P. C. Lichtner. *The quasi-stationary state approximation to coupled mass transport and fluid-rock interaction in a porous medium*. Geochimica et Cosmochimica Acta, **52**(1): 143–165 (1988). doi:10.1016/0016-7037(88)90063-4. (Cited on page 2.)

[27] C. I. Steefel and a. C. Lasaga. *A Coupled Model for Transport of Multiple Chemical-Species and Kinetic Precipitation Dissolution Reactions with Application to Reactive Flow in Single-Phase Hydrothermal Systems* (1994). doi:10.2475/ajs.294.5.529. (Cited on page 3.)

[28] P. C. Lichtner, E. P. C. Lichtner, C. I. Steefel and E. H. Oelkers. *MSA Short Course: Reactive Transport in Porous Media*. In *Reviews in Minerology*, volume 34, 1–81. Mineralogical Society of America, Colorado (1996). (Cited on page 3.)

[29] H. Rhee, B. F. Bodin and N. R. Amundson. *A study of the shock layer in equilibrium exchange systems*. Chemical Engineering Science, **26**(10): 1571–1580 (1971). doi:10.1016/0009-2509(71)86047-5. (Cited on page 3.)

[30] H.-K. Rhee and N. R. Amundson. *A study of the shock layer in nonequilibrium exchange systems*. Chemical Engineering Science, **27**(2): 199–211 (1972). doi: 10.1016/0009-2509(72)85057-7.

[31] E. J. Hinch and B. S. Bhatt. *Stability of an acid front moving through porous rock*. Journal of Fluid Mechanics, **212**(-1): 279 (1990). doi:10.1017/S0022112090001963.

[32] L. W. Lake, S. L. Bryant and A. N. Araque-Martinez. *Geochemistry and fluid flow*. Elsevier Science, Oxford, 1 edition (2002). (Cited on page 3.)

[33] R. J. LeVeque. *Finite Volume Methods for Hyperbolic Problems*. Cambridge University Press, Cambridge (2002). doi:10.1017/CBO9780511791253. (Cited on pages 3, 7, 13, and 34.)

[34] F. G. Helfferich and G. Klein. *MULTICOMPONENT CHROMATOGRAPHY: THEORY OF INTERFERENCE*, volume 8 of *Chromatographic science*. M. Dekker (1970). doi:10.1093/chromsci/8.11.29A. (Cited on page 3.)

[35] E. Abreu, A. Bustos and W. J. Lambert. *Asymptotic Behavior of a Solution of Relaxation System for Flow in Porous Media*. In *Theory, Numerics and Applications of Hyperbolic Problems I*, 15–28. Springer, Aachen (2018). doi: 10.1007/978-3-319-91545-6_2. (Cited on page 3.)

[36] F. Helfferich. *Theory of Multicomponent, Multiphase Displacements in Porous Media*. Society of Petroleum Engineers Journal, **21**(1): 51–62 (1981). doi: 10.2118/8372-PA. (Cited on page 3.)

[37] F. G. HELFFERICH. *MULTICOMPONENT WAVE PROPAGATION: ATTAINMENT OF COHERENCE FROM ARBITRARY STARTING CONDITIONS†*. Chemical Engineering Communications, **44**(1-6): 275–285 (1986). doi:10.1080/00986448608911360. (Cited on page 3.)

[38] G. Pope, L. Lake and F. Helfferich. *Cation Exchange in Chemical Flooding: Part 1-Basic Theory Without Dispersion*. Society of Petroleum Engineers Journal, **18**(6): 418–434 (1978). doi:10.2118/6771-PA. (Cited on page 3.)

[39] L. Lake and F. Helfferich. *Cation Exchange in Chemical Flooding: Part 2–The Effect of Dispersion, Cation Exchange, and Polymer/Surfactant Adsorption on Chemical Flood Environment*. Society of Petroleum Engineers Journal, **18**(6): 435–444 (1978). doi:10.2118/6769-PA. (Cited on page 18.)

[40] F. G. Helfferich. *Conceptual view of column behavior in multicomponent adsorption or ion-exchange systems*. AIChE symposium series, **80**(233): 1–13 (1984). (Cited on page 3.)

[41] H.-K. Rhee, R. Aris and N. R. Amundson. *On the Theory of Multicomponent Chromatography*. Philosophical Transactions of the Royal Society A: Mathematical, Physical and Engineering Sciences, **267**(1182): 419–455 (1970). doi: 10.1098/rsta.1970.0050. (Cited on page 3.)

[42] N. R. Rhee, Hyun-Ku and Aris, Rutherford and Amundson. *First-Order Partial Differential Equations - Theory and Application of Single Equations*. Dover Publications (1986). (Cited on pages 3 and 7.)

[43] N. R. Rhee, Hyun-Ku and Aris, Rutherford and Amundson. *First-order Partial Differential Equations - Theory and Application of Hyperbolic Systems of Quasilinear Equations*. Dover Publications (1989). (Cited on pages 3, 7, and 11.)

[44] S. L. Bryant, R. S. Schechter and L. W. Lake. *Interactions of Precipitation Dissolution Waves and Ion-Exchange in Flow through Permeable Media*. American Institute of Chemical Engineers, **32**(5): 751–764 (1986). doi: 10.1002/aic.690320505. (Cited on page 3.)

[45] K. Kumar, I. S. Pop and F. A. Radu. *Convergence Analysis of Mixed Numerical Schemes for Reactive Flow in a Porous Medium*. SIAM Journal on Numerical Analysis, **51**(4): 2283–2308 (2013). doi:10.1137/120880938. (Cited on page 3.)

[46] K. Kumar, I. S. Pop and F. A. Radu. *Convergence analysis for a conformal discretization of a model for precipitation and dissolution in porous media*. Numerische Mathematik, **127**(4): 715–749 (2014). doi:10.1007/s00211-013-0601-1.

[47] C. Bringedal, I. Berre, I. S. Pop and F. A. Radu. *Upscaling of Non-isothermal Reactive Porous Media Flow with Changing Porosity*. Transport in Porous Media, **114**(2): 371–393 (2016). doi:10.1007/s11242-015-0530-9.

[48] C. Bringedal, I. Berre, I. S. Pop and F. A. Radu. *Upscaling of Nonisothermal Reactive Porous Media Flow under Dominant Péclet Number: The Effect of Changing Porosity*. SIAM Journal on Multiscale Modelling and Simulation, **14**(1): 502–533 (2016). doi:10.1137/15M1022781. (Cited on page 3.)

[49] R. Batycky, M. Blunt and M. Thiele. *A 3D Field-Scale Streamline-Based Reservoir Simulator*. SPE Reservoir Engineering, **12**(04): 246–254 (1997). doi: 10.2118/36726-PA. (Cited on page 4.)

[50] M. Crane, F. Bratvedt, K. Bratvedt, P. Childs and R. Olufsen. *A Fully Compositional Streamline Simulator*. In *SPE Annual Technical Conference and Exhibition*, 1—-10. Society of Petroleum Engineers (2000). doi:10.2118/63156-MS.

[51] M. R. Thiele, R. P. Batycky and M. J. Blunt. *A Streamline-Based 3D Field-Scale Compositional Reservoir Simulator*. In *SPE Annual Technical Conference and Exhibition*. Society of Petroleum Engineers (1997). doi:10.2118/38889-MS. (Cited on page 4.)

[52] M. G. Gerritsen, K. Jessen, B. T. Mallison and J. V. Lambers. *A Fully Adaptive Streamline Framework for the Challenging Simulation of Gas-Injection Processes*. In *SPE Annual Technical Conference and Exhibition*. Society of Petroleum Engineers (2005). doi:10.2118/97270-MS. (Cited on page 4.)

[53] G. Tryggvason, B. Bunner, A. Esmaeeli, D. Juric, N. Al-Rawahi, W. Tauber, J. Han, S. Nas and Y.-J. Jan. *A Front-Tracking Method for the Computations of Multiphase Flow*. Journal of Computational Physics, **169**(2): 708–759 (2001). doi:10.1006/jcph.2001.6726. (Cited on page 4.)

[54] R. Juanes and K.-A. Lie. *A Front-Tracking Method for Efficient Simulation of Miscible Gas Injection Processes*. In *SPE Reservoir Simulation Symposium*, 1–18. Society of Petroleum Engineers (2005). doi:10.2118/93298-MS. (Cited on page 4.)

[55] R. Juanes and K.-A. Lie. *Numerical modeling of multiphase first-contact miscible flows. Part 2. Front-tracking/streamline simulation*. Transport in Porous Media, **72**(1): 97–120 (2008). doi:10.1007/s11242-007-9139-y. (Cited on page 4.)

[56] H. M. Nilsen and K.-A. Lie. *Front Tracking Methods for Use in Streamline Simulation of Compressible Flow*. In *SPE Reservoir Simulation Symposium*, volume di. Society of Petroleum Engineers (2009). doi:10.2118/119099-MS. (Cited on page 4.)

[57] G. Di Donato and M. J. Blunt. *Streamline-based dual-porosity simulation of reactive transport and flow in fractured reservoirs*. Water Resources Research, **40**(4) (2004). doi:10.1029/2003WR002772. (Cited on page 4.)

[58] A. Datta-Gupta and M. J. King. *Streamline simulation: Theory and practice*, volume 11. Society of Petroleum Engineers, 1 edition (2007). (Cited on pages 4 and 50.)

[59] H. Holden, L. Holden and R. Høegh-Krohn. *A numerical method for first order nonlinear scalar conservation laws in one-dimension*. Computers & Mathematics with Applications, **15**(6-8): 595–602 (1988). doi:10.1016/0898-1221(88)90282-9. (Cited on pages 4 and 62.)

[60] C. M. Dafermos. *Polygonal approximations of solutions of the initial value problem for a conservation law*. Journal of Mathematical Analysis and Applications, **38**(1): 33–41 (1972). doi:10.1016/0022-247X(72)90114-X. (Cited on page 4.)

[61] H. Holden and N. H. Risebro. *Front Tracking for Hyperbolic Conservation Laws*, volume 152 of *Applied Mathematical Sciences*. Springer Berlin Heidelberg, Berlin, Heidelberg, 2nd edition (2015). doi:10.1007/978-3-662-47507-2. (Cited on pages 4 and 59.)

[62] T. Gimse and N. H. Risebro. *Solution of the Cauchy Problem for a Conservation Law with a Discontinuous Flux Function*. SIAM Journal on Mathematical Analysis, **23**(3): 635–648 (1992). doi:10.1137/0523032. (Cited on pages 4 and 59.)

[63] T. Gimse and N. H. Risebro. *A note on reservoir simulation for heterogeneous porous media*. Transport in Porous Media, **10**(3): 257–270 (1993). doi:10.1007/BF00616812. (Cited on page 59.)

[64] B. Andreianov and C. Cancès. *Vanishing capillarity solutions of Buckley-Leverett equation with gravity in two-rocks' medium*. Computational Geosciences, **17**(3): 551–572 (2013). doi:10.1007/s10596-012-9329-8.

[65] B. Andreianov and C. Cancès. *On interface transmission conditions for conservation laws with discontinuous flux of general shape*. Journal of Hyperbolic Differential Equations, **12**(02): 343–384 (2015). doi:10.1142/S0219891615500101. (Cited on page 4.)

[66] B. Andreianov and D. Mitrović. *Entropy conditions for scalar conservation laws with discontinuous flux revisited*. Annales de l'Institut Henri Poincare (C) Non Linear Analysis, **32**(6): 1307–1335 (2015). doi:10.1016/j.anihpc.2014.08.002. (Cited on page 4.)

[67] E. Godlewski, K.-C. Le Thanh and P.-A. Raviart. *The numerical interface coupling of nonlinear hyperbolic systems of conservation laws: II. The case of systems*. ESAIM: Mathematical Modelling and Numerical Analysis, **39**(4): 649–692 (2005). doi:10.1051/m2an:2005029. (Cited on pages 4 and 59.)

[68] B. Boutin, F. Coquel and P. G. LeFloch. *Coupling techniques for nonlinear hyperbolic equations. IV. Well-balanced schemes for scalar multi-dimensional and multi-component laws*. Mathematics of Computation, **84**(294): 1663–1702 (2015). doi:10.1090/S0025-5718-2015-02933-0. (Cited on page 4.)

[69] J.-O. Selroos and S. L. Painter. *Effect of transport-pathway simplifications on projected releases of radionuclides from a nuclear waste repository*

(Sweden). Hydrogeology Journal, **20**(8): 1467–1481 (2012). doi:10.1007/s10040-012-0888-5. (Cited on page 5.)

[70] R. N. Horne and F. Rodriguez. *Dispersion in tracer flow in fractured geothermal systems*. Geophysical Research Letters, **10**(4): 289–292 (1983). doi:10.1029/GL010i004p00289. (Cited on page 5.)

[71] B. Brian. *Characterizing flow and transport in fractured geological media: A review*. Advances in Water Resources, **25**(8-12): 861–884 (2002). doi:10.1016/S0309-1708(02)00042-8. (Cited on page 5.)

[72] S. Geiger-Boschung, S. K. Matthäi, J. Niessner and R. Helmig. *Black-Oil Simulations for Three-Component, Three-Phase Flow in Fractured Porous Media*. SPE Journal, **14**(02): 338–354 (2009). doi:10.2118/107485-PA.

[73] S. Karra, N. Makedonska, H. S. Viswanathan, S. L. Painter and J. D. Hyman. *Effect of advective flow in fractures and matrix diffusion on natural gas production*. Water Resources Research, **51**(10): 8646–8657 (2015). doi:10.1002/2014WR016829. (Cited on page 5.)

[74] R. March, H. Elder, F. Doster and S. Geiger. *Accurate Dual-Porosity Modeling of CO2 Storage in Fractured Reservoirs*. In *SPE Reservoir Simulation Conference*, 20–22. Society of Petroleum Engineers (2017). doi:10.2118/182646-MS. (Cited on page 5.)

[75] M. Karimi-Fard, L. Durlofsky and K. Aziz. *An Efficient Discrete-Fracture Model Applicable for General-Purpose Reservoir Simulators*. SPE Journal, **9**(02): 227–236 (2004). doi:10.2118/88812-PA. (Cited on page 5.)

[76] S. Karra, D. O'Malley, J. D. Hyman, H. S. Viswanathan and G. Srinivasan. *Modeling flow and transport in fracture networks using graphs*. Physical Review E, **97**(3): 033304 (2018). doi:10.1103/PhysRevE.97.033304. (Cited on page 5.)

[77] S. Srinivasan and A. Anupam. *Multiscale Modeling of Fracture Network in a Carbonate Reservoir*. In P. Abrahamsen, R. Hauge and O. Kolbjørnsen, eds., *Geostatistics*, volume 17 of *Quantitative Geology and Geostatistics*. Springer Netherlands, Oslo (2012). doi:10.1007/978-94-007-4153-9. (Cited on page 5.)

[78] B. Berkowitz and I. Balberg. *Percolation theory and its application to groundwater hydrology*. Water Resources Research, **29**(4): 775–794 (1993). doi:10.1029/92WR02707. (Cited on page 5.)

[79] M. Valera, Z. Guo, P. Kelly, S. Matz, V. A. Cantu, A. G. Percus, J. D. Hyman, G. Srinivasan and H. S. Viswanathan. *Machine learning for graph-based representations of three-dimensional discrete fracture networks*. Computational Geosciences, **22**(3): 695–710 (2018). doi:10.1007/s10596-018-9720-1. (Cited on page 5.)

[80] F. W. Schwartz and L. Smith. *A continuum approach for modeling mass transport in fractured media*. Water Resources Research, **24**(8): 1360–1372 (1988). doi:10.1029/WR024i008p01360. (Cited on page 5.)

[81] Y.-j. Park, K.-k. Lee and B. Berkowitz. *Effects of junction transfer characteristics on transport in fracture networks*. Water Resources Research, **37**(4): 909–923 (2001). doi:10.1029/2000WR900365. (Cited on page 5.)

[82] J. Smoller. *Shock Waves and Reaction-Diffusion Equations*, volume 258 of *Grundlehren der mathematischen Wissenschaften*. Springer New York, New York, NY (1994). doi:10.1007/978-1-4612-0873-0. (Cited on pages 7, 23, and 24.)

[83] C. M. Dafermos. *Hyperbolic Conservation Laws in Continuum Physics*, volume 1. Springer, 3 edition (2007). doi:10.1007/978-3-642-25847-3. (Cited on pages 7, 23, and 62.)

[84] M. G. Crandall. *Viscosity solutions: A primer*. In *Viscosity Solutions and Applications*, 1–43. Springer Berlin Heidelberg (1997). doi:10.1007/BFb0094294. (Cited on page 12.)

[85] P. D. Lax. *Hyperbolic Systems of Conservation Laws II.* Communications on Pure and Applied Mathematics, **10**(4): 537–566 (1957). (Cited on page 13.)

[86] G. Klein, D. Tondeur and T. Vermeulen. *Multicomponent Ion Exchange in Fixed Beds. General Properties of Equilibrium Systems*. Industrial & Engineering Chemistry Fundamentals, **6**(3): 339–351 (1967). doi:10.1021/i160023a004. (Cited on page 14.)

[87] A. Venkatraman, M. A. Hesse, L. W. Lake and R. T. Johns. *Analytical Solutions for Flow in Porous Media with Multicomponent Cation Exchange Reactions*. Water Resources Research, **50**: 5831–5847 (2014). doi:10.1002/2013WR015091. (Cited on page 15.)

[88] R. J. LeVeque. *Numerical Methods for Conservation Laws*. Birkhäuser Basel, Basel (1992). doi:10.1007/978-3-0348-8629-1. (Cited on page 15.)

[89] B. Temple. *Systems of Conservation Laws with Invariant Submanifolds*. Transactions of the American Mathematical Society, **280**(2): 781 (1983). doi:10.2307/1999646. (Cited on pages 16 and 26.)

[90] S. Dimitrios. *Modelling of Ion Exchange Reactions during Low Salinity Waterflooding*. M.sc, Heriot Watt University (2016). (Cited on page 17.)

[91] K.-A. Lie. *Front tracking for one-dimensional quasilinear hyperbolic equations with variable coefficients*. Numerical Algorithms, **24**(3): 275–298 (2000). doi: 10.1023/A:1019157629824. (Cited on page 23.)

[92] F. Asakura and M. Yamazaki. *Geometry of Hugoniot curves in 2x2 systems of hyperbolic conservation laws with quadratic flux functions*. IMA Journal of Applied Mathematics (Institute of Mathematics and Its Applications), **70**(6): 700–722 (2005). doi:10.1093/imamat/hxh072. (Cited on page 25.)

[93] G. R. Lawlor. *A L'hospital's rule for multivariable functions* (2012). (Cited on page 29.)

[94] D. W. Pollock. *Semianalytical Computation of Path Lines for Finite-Difference Models*. Ground Water, **26**(6): 743–750 (1988). doi:10.1111/j.1745-6584.1988.tb00425.x. (Cited on page 50.)

[95] A. Costa. *Permeability-porosity relationship: A reexamination of the Kozeny-Carman equation based on a fractal pore-space geometry assumption*. Geophysical Research Letters, **33**(2): L02318 (2006). doi:10.1029/2005GL025134. (Cited on page 51.)

[96] V. Kippe, H. Haegland and K.-A. Lie. *A Method To Improve the Mass Balance in Streamline Methods*. In *Proceedings of SPE Reservoir Simulation Symposium*, 1–12. Society of Petroleum Engineers (2007). doi:10.2523/106250-MS. (Cited on page 52.)

[97] B. T. Mallison, M. G. Gerritsen and S. F. Matringe. *Improved Mappings for Streamline-Based Simulation*. SPE Journal, **11**(03): 294–302 (2006). doi: 10.2118/89352-PA. (Cited on page 52.)

[98] B. Andreianov, K. H. Karlsen and N. H. Risebro. *A Theory of L 1-Dissipative Solvers for Scalar Conservation Laws with Discontinuous Flux*. Archive for Rational Mechanics and Analysis, **201**(1): 27–86 (2011). doi: 10.1007/s00205-010-0389-4. (Cited on page 59.)

[99] K.-A. Lie. *An Introduction to Reservoir Simulation Using MATLAB*. SINTEF, Oslo (2016). (Cited on page 66.)

[100] M. Christie and M. Blunt. *Tenth SPE Comparative Solution Project: A Comparison of Upscaling Techniques*. SPE Reservoir Evaluation & Engineering, **4**(04): 308–317 (2001). doi:10.2118/72469-PA. (Cited on page 68.)

[101] P. M. Adler, J.-F. Thovert and V. V. Mourzenko. *Fractured porous media*. Oxford University Press, Oxford (2013). (Cited on pages 74 and 88.)

[102] M. Ghaderi Zefreh, F. Doster and M. A. Hesse. *Theory of dissolution and precipitation waves—redux*. AIChE Journal, **65**(6): e16573 (2019). doi: 10.1002/aic.16573. (Cited on page 82.)